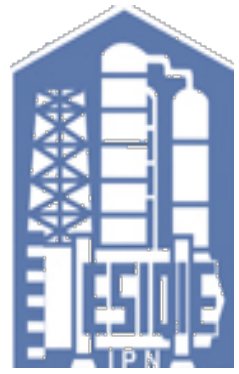




INSTITUTO POLITÉCNICO NACIONAL.  
ESCUELA SUPERIOR DE INGENIERÍA  
QUÍMICA E INDUSTRIAS EXTRACTIVAS



“Influence of Al on the superplastic behavior at low temperatures of fine grained Mg-Al-Zn alloys”

Tesis que para obtener el título de:  
Doctor en ciencias en metalurgia y materiales

Presenta:

M. en C. JOSÉ VICTORIA HERNÁNDEZ

Director de tesis

Dr. DAVID HERNÁNDEZ SILVA





**INSTITUTO POLITÉCNICO NACIONAL**  
**SECRETARÍA DE INVESTIGACIÓN Y POSGRADO**

*CARTA CESIÓN DE DERECHOS*

En la Ciudad de México el día 05 del mes de Diciembre del año 2011, el (la) que suscribe José Victoria Hernández alumno (a) del Programa de Doctorado en Ciencias en Metalurgia y Materiales con número de registro B081736, adscrito a la Escuela Superior de Ingeniería Química e Industrias Extractivas, manifiesta que es autor (a) intelectual del presente trabajo de Tesis bajo la dirección de Dr. David Hernández Silva y cede los derechos del trabajo intitulado *Influence of Al on the superplastic behavior at low temperatures of fine grained Mg-Al-Zn alloys*, al Instituto Politécnico Nacional para su difusión, con fines académicos y de investigación.

Los usuarios de la información no deben reproducir el contenido textual, gráficas o datos del trabajo sin el permiso expreso del autor y/o director del trabajo. Este puede ser obtenido escribiendo a la siguiente dirección j\_Victoria-Hernandez@hotmail.com. Sí el permiso se otorga, el usuario deberá dar el agradecimiento correspondiente y citar la fuente del mismo.

  
José Victoria Hernández

Nombre y firma

## Agradecimientos

Al Instituto Politécnico Nacional

Al Consejo Nacional de Ciencia y Tecnología (CONACyT) por el apoyo económico durante mis estudios de doctorado, así como también, por el apoyo que se me brindó para hacer mi estancia de investigación en el Helmholtz Zentrum Geesthacht en Alemania.

Al Dr. rer. nat. Dietmar Letzig por brindarme la oportunidad de trabajar en dicho instituto en el grupo de aleaciones deformables de Magnesio.

Al Dr. rer. nat. Jan Bohlen por todo su apoyo, amistad e invaluable consejos durante mi estancia, así como también, ser un gran compañero durante la redacción de los artículos de investigación derivados de esta tesis.

Al Dr. Sangbong Yi por todos sus consejos y por brindarme su amistad durante mi estancia.

Al grupo de técnicos en del grupo aleaciones deformables de magnesio por la preparación de muestras y mediciones en las que me ayudaron.

Mis mas sinceros agradecimientos a mis compañeros de trabajo y amigos Rodolfo, Mario, Rosario y Oliver, Ligia y Orley, Enrique y Hoa, Joachim, Morelia y Dirk, Carmelita, Karina, Lenka, Lennart y Gerrit por apoyarme y hacerme sentir en casa.

Al Dr. David Hernández Silva por todo su apoyo y consejos durante mis estudios de maestría y doctorado.

A Dios.

A ti María que te llevo dentro de mi corazón.

A esposa Jazmín por su amor e incondicional apoyo y a mi hija María José que me da la fuerza para continuar adelante.

A mis padres y hermanas por su apoyo y amor que siempre me han dado.

**Gracias.**

## Abstract:

In this work, the effect of Aluminum on the superplastic behavior at low temperatures of three wrought Mg-Al-Zn alloys has been investigated. The magnesium alloys were processed by hydrostatic extrusion (HE). This thermomechanical treatment allows higher extrusion rates and lower temperatures than conventional direct or indirect extrusion. By means of HE was possible to generate very fine grained microstructures with average grain sizes of 5  $\mu\text{m}$  for AZ31, 5  $\mu\text{m}$  for AZ61 and 8  $\mu\text{m}$  for AZ80. All extrusions were performed at only 150 °C and an extrusion rate of 8 m/min. In order to reveal the deformation mechanisms involved during plastic deformation, tension and compression tests were carried out at 175, 200 and 225 °C, and at three different strain rates of  $10^{-2}$ ,  $10^{-3}$  and  $10^{-4}$  s $^{-1}$ . All alloys showed superplastic behavior at low temperature, 200 °C for AZ31, 175 °C for AZ61 and 225 °C for AZ80. The superplastic behavior was enhanced by dynamic recrystallisation (DRX) which produced a finer grain microstructure during deformation. Dynamic recrystallisation produced small and equiaxed grains which facilitated the dominant mechanism of grain boundary sliding (GBS) responsible for the high elongations recorded. It was found that Al affects directly the recrystallisation mechanism which was one of the most important operative mechanisms during deformation. Moreover, with increasing the Al content, the precipitation of secondary phase  $\text{Mg}_{17}\text{Al}_{12}$  played an important role in the detriment of the superplastic behavior at the highest temperature or at the lowest strain rate used. In addition to these effects, the detection by means of electron backscatter diffraction (EBSD) of a special texture component  $\langle 11.1 \rangle$  during superplastic behavior was possible. It is note worthy that such component has only been seen up to now in magnesium alloys containing rare earth elements.

## RESUMEN:

En este trabajo, el efecto del Aluminio sobre el comportamiento superplástico a baja temperatura de aleaciones Magnesio-Aluminio-Zinc ha sido investigado. Las aleaciones de magnesio fueron procesadas por extrusión hidrostática (EH). Este tipo de tratamiento termomecánico permite el uso de velocidades de extrusión más altas y temperaturas de extrusión más bajas que extrusiones convencionales de extrusión directa e indirecta. Por medio de EH, fue posible procesar aleaciones con tamaños de grano alrededor de  $\sim 5 \mu\text{m}$  para la aleación AZ31,  $5 \mu\text{m}$  para la AZ61 y  $8 \mu\text{m}$  para la AZ80. Las extrusiones fueron realizadas a una temperatura de tan solo  $150 \text{ }^\circ\text{C}$  y con una velocidad de extrusión de  $8 \text{ m/min}$ .

Pruebas de tensión y compresión en las aleaciones extruidas fueron hechas a  $175$ ,  $200$  y  $225 \text{ }^\circ\text{C}$ ; a cada temperatura tres diferentes velocidades de deformación fueron empleadas:  $10^{-2} \text{ s}^{-1}$ ,  $10^{-3} \text{ s}^{-1}$  y  $10^{-4} \text{ s}^{-1}$ , todo esto con el objetivo de revelar los mecanismos de deformación involucrados durante la deformación plástica en dichas condiciones.

Todas las aleaciones mostraron comportamiento superplástico a baja temperatura:  $200 \text{ }^\circ\text{C}$  para la AZ31,  $175 \text{ }^\circ\text{C}$  para AZ61 y  $225 \text{ }^\circ\text{C}$  para la aleación AZ80.

El comportamiento superplástico fue mejorado por el efecto de la recristalización dinámica (DRX por sus siglas en inglés) la cual produjo una nueva microestructura durante la deformación con granos más finos y equiaxiales que los obtenidos durante la extrusión. La reducción del tamaño de grano durante la deformación mejoró el mecanismo dominante y responsable de los altos alargamientos medidos que fue el deslizamiento de límites de grano (GBS por sus siglas en inglés). Se ha encontrado que el Al afecta directamente el mecanismo de recristalización que fue uno de los más importantes durante la deformación de las aleaciones AZ's. También, al incrementar el contenido de Al, la precipitación de la fase secundaria  $\text{Mg}_{17}\text{Al}_{12}$  tuvo un papel importante en el detrimento del comportamiento superplástico en la temperatura más alta usada o en la velocidad de deformación más baja. Además de estos dos efectos, fue posible la detección por medio de difracción de electrones retrodispersados (EBDS) la formación de un componente especial de textura  $\langle 11.1 \rangle$  durante la deformación superplástica, haciendo ver que nuevos sistemas de deslizamiento son requeridos con el fin de compensar la gran deformación que sufre el material a bajas temperaturas. Es importante decir que dicho componente solo ha sido visto hasta ahora en sistemas de aleación de magnesio que contienen elementos de tierras raras.

1. Introduction	1
1.1 Specific objectives	3
2. Fundamentals	4
2.1 Magnesium	4
2.1.1 Magnesium alloys	5
2.1.2 Influence of alloying element additions on magnesium	5
2.2 Deformation behavior of magnesium and its alloys	7
2.3 Structural superplasticity	9
2.3.1 Atomic mechanism for superplasticity	11
2.3.2 Structural superplasticity in Mg alloys	12
2.4 Texture	13
2.4.1 Pole figure goniometer and texture analysis	14
2.4.2 EBSD technique	16
2.4.3 Texture analysis during superplastic deformation	18
2.5 Processing methods used for getting fine grained Mg alloys	20
2.5.1 Hot rolling	20
2.5.2 Direct and indirect extrusion	21
2.5.3 Hydrostatic extrusion	21
2.5.4 Deformation mechanisms active during thermomechanical treatment	24
3. Experimental procedure	27

3.1 Melting of the alloys	27
3.2 Thermomechanical treatment	27
3.3 Metallographic inspection	28
3.4 Texture measurements	29
3.5 Tension tests at elevated temperatures	30
3.6 Compression tests at elevated temperatures	31
3.7 EBSD Measurements in deformed samples	31
4. Results	32
4.1 Microstructure of the extruded alloys	32
4.2 Macro-texture	33
4.3 Mechanical test	35
4.3.1 Room temperature	35
4.3.2 Tension and compression tests at intermediate temperature	36
4.4 Yield asymmetry	41
4.5 Elongation to failure of tested alloys	43
4.5.1 Flow stress analysis of the tension tests	44
4.6 Deformed samples	45
4.7 Micrographs after fracture	48
4.8 EBSD analysis	52
4.8.1 Texture of deformed samples in tension	55
5. Discussion	57
5.1 Microstructure and texture of as-extruded alloys	57
5.2 Mechanical tests	58
5.2.1. Room temperature	58

5.2.2 Intermediate temperatures	60
5.3 Yield asymmetry at intermediate temperatures	64
5.4 Elongation to failure of tested samples	67
5.4.1 Strain rate sensitivity	71
5.4.2 Samples morphology after deformation	75
5.5 Microstructural and texture analysis after tensile deformation by means of EBSD	76
5.5.1 Zener-Hollomon parameter	76
5.5.2 Microstructural analysis	77
5.5.3 Texture development	79
6. Conclusions	93
References	96

## List of abbreviations and symbols

$\sigma$	True stress
$\varepsilon$	True strain
$\dot{\varepsilon}$	Strain rate
$\varepsilon_c$	Critical strain
$\varepsilon_p$	Strain peak
CRSS	Critical resolved shear stress
CYS	Compressive yield strength
e	Elongation (%)
EBSD	Electron backscatter diffraction
EBSP	Electron backscatter diffraction pattern
$D_o$	Initial grain size
DDRX	Discontinuous dynamic recrystallisation
DRX	Dynamic recrystallisation
RDRX	Rotational dynamic recrystallisation
GBS	Grain boundary sliding
IPF	Inverse pole figure
HCP	Hexagonal close package structure
HE	Hydrostatic extrusion
K	Material's constant
LTDRX	Low temperature dynamic recrystallisation
LTSP	Low temperature superplasticity

m	Strain rate sensitivity
OIM	Orientation maps
PM	Powder metallurgy
SPD	Severe plastic deformation techniques
T	Temperature
T <sub>m</sub>	Melting temperature
TYS	Tensile yield strength
UCS	Ultimate compressive strength
UTS	Ultimate tensile strength

## 1. Introduction

The low density of magnesium makes it attractive for lightweight parts used principally in the automotive and aeronautic industries. Over the last 20 years, great advances in magnesium research have been made [1]. Wrought magnesium alloys have so far found limited application, mainly as a result of their poor formability at low temperatures close to room temperature. This low formability is due to the hexagonal crystal structure and the limited number of deformation modes available near room temperature (slip and twinning) [2]. Much work has been carried out in order to improve the formability and mechanical properties of wrought magnesium alloys. Current research in this area is concerned with new alloying systems, the understanding of the deformation mechanisms involved during deformation of polycrystalline magnesium alloys and intense research of thermomechanical treatments that allow improving the microstructure and formability at low temperatures [3-8]. Nevertheless, for the industry even the lightest metal in form of wrought magnesium alloys are useless if they can not be deformed by conventional thermomechanical treatments like rolling and extrusions in industrial scale.

Since superplasticity refers to the ability of reaching very high elongations when the material is pulled in tension [9], the application of superplastic forming (SF) to wrought magnesium alloys could be interesting for the industry. Besides, a better understanding of the operative deformation mechanisms during superplastic deformation could give us a hint of where the material is able to undergo higher deformation, improving the plasticity especially at low temperatures near room temperature.

Recently, Swiosteck et al. [10] showed that hydrostatic extrusion (HE) is a feasible thermomechanical treatment for the production of fine grained

magnesium alloys. During HE, a hydrostatic medium presses onto the billet. The pressure is applied with a ram and passed on the medium leading to hydrostatic pressure from all sides onto the billet to make it flow through the die. This extrusion enables finer grains and higher extrusion rates at lower extrusion temperatures than the conventional direct or indirect extrusion processes [11]. The application of a low temperature process and low temperature superplasticity are especially attractive features in magnesium alloys because of their poor formability near room temperature.

Magnesium alloys containing aluminum and zinc are characterized by the low cost and ease of handling, together with good strength, ductility, and resistance to atmospheric corrosion. The wrought magnesium alloys AZ31, AZ61, and AZ80 have been successfully extruded by means of hydrostatic extrusion [10]. Besides, it has been proved that it is possible to use rather low extrusion temperatures as low as 100 °C in order to get a fine grained microstructure (<10 μm). This fine microstructure could be suitable for superplastic forming.

Consequently, the aim of this work is to use common wrought magnesium alloys from the series Aluminum- Zinc (AZ31, AZ61 and AZ80) processed by HE and test them in order to examine superplastic behavior, especially at low temperatures from 175 to 225 °C. The results can be used to reveal the deformation mechanisms during low temperature superplastic deformation and to understand the influence of aluminum content.

## 1.1 Specific objectives:

- Apply hydrostatic extrusion to the common wrought Mg-Al-Zn alloys in order to get a fine grained microstructure suitable for superplasticity.
- To understand the role of Al on the retention of a fine grained microstructure able to exhibit superplastic behavior at low temperatures ( $<0.5T_m$ ) and different strain rates. This will be carried out characterizing the precipitation of the secondary phase  $Mg_{17}Al_{12}$ . To do this, three different alloys will be used, AZ31, AZ61, and AZ80 with Al content of 3, 6 and 8 wt.% respectively.
- To analyze the asymmetry of tensile yield strength (TYS) and compressive yield strength (CYS) resulting after the thermomechanical treatment of AZ-Mg alloys. This analysis will be carried out at temperatures lower than 0.5 of the melting temperature ( $T_m$ ).
- To study the influence of temperature and strain rate on the activation of different deformation mechanisms during tension and compression tests.
- To analyze the texture changes during tensile deformation of AZ-Magnesium alloys at different temperatures and different strain rates.

## 2. Fundamentals

### 2.1 Magnesium

Magnesium is the lightest of all structural metals. As such, it forms the basis for commercial alloys that have found successful use in a wide variety of applications. It is a plentiful element, comprising 2.7% of the earth's crust. [12]. With a density of 1.74 [g/cm<sup>3</sup>] magnesium is particularly attractive for the industry for producing lightweight parts used principally in the automotive and aeronautic industries, if it is compared with the density of the most frequently used commercial structural metals e.g. steel (7.8 [g/cm<sup>3</sup>]) and aluminum (2.7 [g/cm<sup>3</sup>]) [1]. In table 1 the physical properties of magnesium are presented [12]:

Table 1: Physical properties of pure magnesium.	
Crystalline structure	Hexagonal close packet (HCP)
Lattice parameter a	0.32094 nm ( $\pm 0.01\%$ )
Lattice parameter c	5.2107 nm ( $\pm 0.01\%$ )
c/a ratio	1.6236
Melting point	648.8 °C
Latent heat of fusion	382 [KJ/kg]

Magnesium has been used for a wide variety of applications, including pyrotechnics, metallurgical, chemical and structural applications. In this chapter only a brief introduction about cast magnesium alloys will be presented. Because the main topic is superplasticity for structural applications, the scope of this thesis will be related to wrought magnesium alloys

### **2.1.1 Magnesium alloys.**

Due to magnesium's low strength, this metal can not be used for structural applications in its pure form. Therefore, it is necessary to add some alloying elements in order to increase the strength and ductility at room temperature [13]. The main mechanism for improving the mechanical properties is precipitation hardening and/or solid solution hardening [14]. While solid-solution hardening is determined by the differences in the atomic radii of the involved elements, the effectiveness of precipitation hardening mainly depends on the reduced solubility at low temperatures, the magnesium content of intermetallic phase, and its stability at application temperature. Magnesium forms intermetallic phases with most alloying elements, the stability of the phase increasing with the electronegativity of the other element.

### **2.1.2 Influence of alloying element additions on magnesium**

The AZ series are at present of the highest commercial importance. The alloys are relatively inexpensive to produce due to the low aluminum content and easy to fabricate. The presence of aluminum allows a significant solid solution strengthening. The alloys of the AZ series developed over a half a century ago have seen only some minor adjustments in the chemical composition [15].

Since 1920's, aluminum has been the most important alloying element for significantly increasing the tensile strength of magnesium alloys by forming the intermetallic phase  $Mg_{17}Al_{12}$ . The precipitation of this phase is observed at temperatures higher than 120 °C. Magnesium alloys that contain Al are

usually heat treated. In addition to the improvements in mechanical properties, a higher amount of Al increases significantly the castability. This is the main reason why most technical alloys, specially casting alloys, contain a high percentage of Al. However, the disadvantage is the higher tendency to micro-porosity as the aluminum content is increased.

Together with Al, Zinc (Zn) is another important alloying element for magnesium. This element induces the same behavior as Al in terms of strengthening and castability. By adding up to 3% Zn to magnesium, shrinkage can be compensated and tensile strength is raised. In addition to the improvements in mechanical properties, recent studies in binary Mg-Zn alloys by Meza et al. [13] showed that Zn is an important alloying element which contributes to grain refinement during casting. His studies demonstrated that the grain refinement mechanism is controlled by the Zn solute content and is associated with undercooling of the melt. The grain refinement in the casting process also will influence strongly the deformation behavior during thermomechanical processes like rolling and extrusion.

Manganese (Mn) has an important effect in raising the strength of magnesium alloys and improving their corrosion resistance [14]. As an iron remover, Mn has played an important role in the development of the AM (Aluminum-Manganese) alloys [16]. On the other hand, it has long been realized that the grain size of Mg-Al alloys is associated with the presence of impurity elements as Fe, Mn and C [17]. Therefore, Mn also has been used for its grain refinement effect.

Rare earth elements (RE like Gd, Ce, Nd, La and including Y) form eutectic systems of limited solubility with magnesium [14]. Therefore, precipitation hardening is possible. The precipitates are very stable and raise the creep resistance and the strength of the Mg-RE alloys at high temperatures.

It is also well established that the addition of rare earth elements leads to the formation of texture after thermomechanical treatments (e.g. extrusion and rolling) distinctly different from conventional Mg-Al-Zn [18, 19].

## 2.2 Deformation behavior of magnesium and its alloys

The deformation of magnesium is strongly influenced by the inherent anisotropy that results from the low symmetry of the HCP structure. This low symmetry limits the availability of different slip systems, which can be activated simultaneously.

A critical factor for the deformation of magnesium is the temperature. At room temperature magnesium and its alloys deform only by two deformation mechanisms, slip and twinning [19].

Slip occurs when the shear stress on the slip planes in the slip direction reaches a threshold value called the critical resolved shear stress (CRSS). This slip mechanism is controlled by dislocation glide.

At room temperature, primary slip occurs on the (0001) basal plane and in the  $\langle 11\bar{2}0 \rangle$  most closely packed direction of the plane. Secondary slip occurs in the  $\langle 11\bar{2}0 \rangle$  direction on the  $\{10\bar{1}0\}$  prismatic planes [12]. At elevated temperatures, slip also occurs in the  $\langle 11\bar{2}0 \rangle$  direction on the  $\{10\bar{1}1\}$  pyramidal planes. The increase in plasticity that occurs between 200 and 225 °C, depending on the alloy composition has been described by Siebel [20]. For pure magnesium the ductility is increased above 225 °C. Measurements by Roberts [21], Raynor [22], and Chapman [23], showed gliding of the basal plane up to 225 °C, and also, the pyramidal planes which lead to an erratic increase in the plastic formability, are only activated above 225 °C [14]

The crystallographic indices of the principal slip planes of the HCP structure of magnesium and some of its available slip systems are shown in Fig.1.

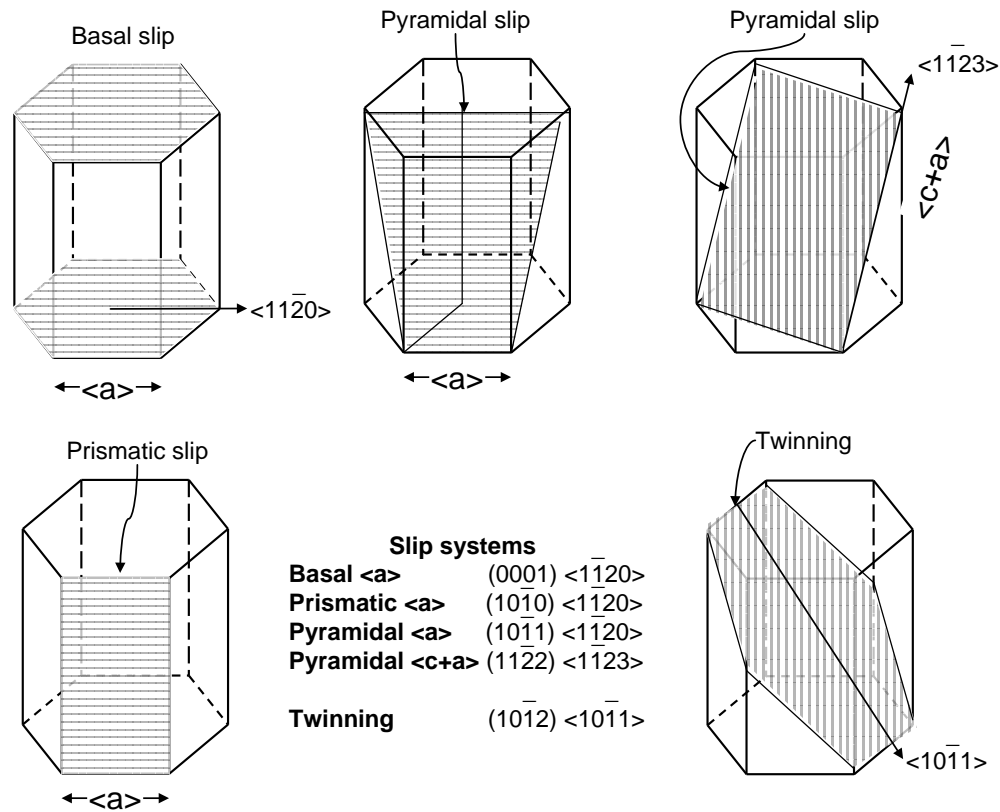


Fig. 1. Slip systems in hexagonal close packed structure. [24, 25]

An additional deformation mechanism which can compensate for the lack of slip systems is twinning.

At room temperature there are two commonly observed twinning planes,  $\{10\bar{1}2\}$  and  $\{10\bar{1}1\}$ . These modes accommodate extension and contraction along the c-axis, respectively [26]. Secondary twinning occurs across the  $\{30\bar{3}4\}$  planes. Meanwhile, at elevated temperatures also occurs across the  $\{10\bar{1}3\}$  planes.

Due to the low possibility to activate additional slip systems, deformation at room temperature in polycrystalline magnesium is limited only to basal slip and twinning, which results in low formability. If twinning dominates during deformation, it leads to brittle failure [27, 28]

## 2.3 Structural Superplasticity

Structural superplasticity refers to the ability of some metals to exhibit exceptional high elongations when pulled in tension while maintaining a characteristic stable microstructure [29]. Furthermore, during tensile deformation the material shows low or even vanishing strength and an unusual capacity for stable neck free plastic extension [30].

Superplasticity is a high-homologous-temperature phenomenon that leads to some metals to reach extended or anomalous ductility under restricted circumstances:

- Superplasticity is generally restricted to low strain rates from  $10^{-5}$  to  $10^{-3} \text{ s}^{-1}$  [31].
- The temperature should be around 0.5 of  $T_m$  or higher (where  $T_m$  is the absolute melting temperature) [32]

In addition to these, the main requirements for the materials to show superplasticity can be listed as follows [31]:

- 1) Fine and stable microstructure, usually superplasticity is found in metals which have average grain sizes lower than  $10 \mu\text{m}$ .
- 2) The presence of a second phase is necessary to inhibit grain growth.
- 3) The strength of the second phase must generally be of the same order as that of the matrix.
- 4) The second phase, if harder, should be finely distributed within the matrix.
- 5) The grain boundaries between the matrix grains should be of the high angle kind.

- 6) The grain boundaries should be mobile so as to reduce stress concentration at triple points.
- 7) The grains should be equiaxed in order to enable a grain boundary to experience a shear stress, allowing grain boundary sliding to occur.
- 8) The grain boundaries must resist tensile separation

During deformation, the steady state during uniaxial tensile deformation of superplastic materials can be described by the power law:

$$\sigma = K \cdot \dot{\varepsilon}^m \quad (1)$$

where  $\sigma$  is the flow stress,  $\dot{\varepsilon}$  is the strain rate,  $k$  is a constant and  $m$  is the strain rate sensitivity that should be higher than 0.3 [33].

$m$  is defined as:

$$m = \frac{\delta \ln \sigma}{\delta \ln \dot{\varepsilon}} \quad (2)$$

Three regions can be recognized which may conveniently be labeled I, II and III. The three regions are displayed in Fig. 2. Region II is the one of interest where superplasticity is displayed (see Fig. 2a). The peak values of  $m$  in this region (located in the inflection point of the curve) coincide with the maximum elongation (see Fig. 2b). In the superplastic region,  $m$  has values from 0.3 to 0.9 [31].

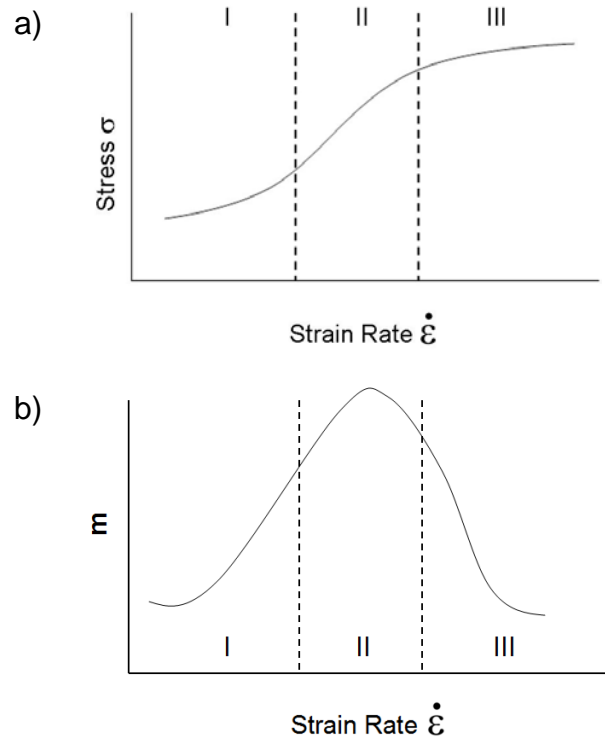


Fig. 2: Flow stress against strain rate.

With  $m > 0.3$ , Grain Boundary Sliding (GBS) is the mechanism that controls deformation and is related with superplastic behavior of materials. Conversely, if  $m$  values are lower than 0.3 the ductility is usually low and dislocation creep processes are activated [32, 34].

### 2.3.1 Atomic mechanism for Superplasticity:

GBS accommodated by dislocation motion: Ball and Hutchinson [35] put forward the idea that several groups of grains slide at once. When there is an unfavorably oriented grain, a stress concentration results which can be

relieved by dislocation motion. The dislocations, which are necessarily in a pile-up, prevent further sliding until the lead dislocation climbs.

GBS and diffusion creep: Ashby and Verral [36] proposed a grain switching event as central to their model. A group of 4 grains react to a tensile stress, sliding past each other and changing their shape to maintain continuity. These switching events occur randomly throughout the specimen with various clusters in different stages of the process.

GBS and core-mantle theory: Gifkins [37] proposed for each grain a non-deforming core surrounded by a mantle in which flow occurs. While the core contains statistically stored dislocations, the mantle, which is a few percent of the grain diameter, contains geometrically necessary dislocations. The grain boundary dislocations piled-up against a triple edge are responsible by their movement for grain boundary sliding.

Micromultiplicity: Sirinivasa [31] proposed that as the grain boundary network has alternate sets of shear paths, the deformation continues even if the grain boundary sliding is obstructed locally. In other words, the local stress conditions would enhance alternative the importance of the obstacles.

### **2.3.2 Structural superplasticity in Mg alloys**

Superplastic behavior in magnesium alloys has been observed by different authors. Some of those results are presented in Table 2.

In the upper part of the table, conventional thermomechanical treatments (rolling and extrusion) were used. It is interesting to note that the deformation temperatures used during superplastic deformation were

higher than  $0.5T_m$  and that the average grain size was between 6 to 25  $\mu\text{m}$ . The  $m$  values reported in those works were about 0.5. It is known that a high value on  $m$  retards flow localization, and therefore, the ductility is generally high [32]. However, by means of Severe Plastic Deformation techniques (SPD), fine or ultra fine microstructures (grain size  $<1 \mu\text{m}$ ) can be attained. This reduction of grain size enables  $m$  values to be higher than 0.3 even at temperatures lower than  $0.5T_m$ . This corresponds to a phenomenon called low temperature superplasticity (LTSP). Some of these works are presented in the lower part of Table 2.

Table 2: Superplasticity in Mg-based alloys processed by different methods.

Alloy	Grain size ( $\mu\text{m}$ )	T ( $^{\circ}\text{C}$ )	T/ $T_m$	$\dot{\epsilon}$ ( $\text{s}^{-1}$ )	$\epsilon$ to failure (%)	$m$	Processing method	Reference
<i>Conventional superplasticity (<math>&gt;0.5T_m</math>)</i>								
AZ31	8.1	400	0.70	$10^{-4}$	475	~0.5	Rolling	[32]
AZ31	6.6	400	0.70	$2 \times 10^{-4}$	800	0.56	Strip Castin+Rolling	[38]
AZ31	Mixed 8-25	450	0.79	$10^{-5}$	596	0.5	Extrusion	[39]
AZ61	8.7	400	0.76	$2 \times 10^{-4}$	400	0.5	Hot Rolling	[40]
AZ61	~20	375	0.71	$10^{-5}$	~450	0.5	Rolling	[41]
<i>Low temperature superplasticity (<math>\leq 0.5T_m</math>)</i>								
AZ31	0.7	150	0.26	$10^{-4}$	460	-	Extrusion+ECAP	[39]
AZ61	0.3-0.5	250	0.47	$3 \times 10^{-4}$	850	0.37	Differential Rolling (DSR-SPD technique)	[34]
AZ61	~0.6	200	0.38	$3.3 \times 10^{-4}$	1320	0.3	Extrusion +ECAP	[42]
AZ91	0.5	200	0.42	$5 \times 10^{-5}$	~600	0.5	ECAE	[43]
ZK60	1.4	250	0.48	$10^{-3}$	~1000	0.5	High Ratio DSR-SPD	[44]
ZK61	3.7	250	0.48	$1.4 \times 10^{-4}$	1330	~0.45	Isothermal Rolling	[45]
ZK61	~0.7	200	0.38	$10^{-3}$	659	0.5	Powder Metallurgy (PM)	[34]

## 2.4 Texture

Texture is one of the fundamental parameters characterizing polycrystalline materials in addition to crystal structure and lattice defects. This applies to technological materials, i.e. metals, ceramics and polycrystalline polymers. On the one hand, texture is the link between anisotropic properties of single crystals and those of the polycrystalline material and on the other hand, texture changes in the material are indicative of solid state processes of all kinds. Hence, texture studies provide an excellent and convenient means to study these processes themselves or to obtain information about the history of a material. [46].

### 2.4.1 Pole figure goniometer and texture analysis [24, 47]

A pole-figure goniometer using reflection geometry and monochromatic X-rays Cu K $\alpha$  radiation can be used for quantitative determination of textures. In this device, the source and counter are arranged in a fixed geometry, depending only on the Bragg angle of the investigated crystallographic plane. The Bragg angle refers to a reflection condition if Bragg's law is obeyed:

$$n\lambda = 2d \sin\theta \quad (3)$$

where  $\lambda$  is wavelength;  $d$  is the spacing of the reflecting planes;  $\theta$  is the angle of incidence and reflection and  $n$  is the order of diffraction. The sample is mounted on a holder which can be rotated around two mutually perpendicular axes to orient the specimen in any position with respect to the incident X-ray beam. The goniometer moves the detector with respect to the X-ray beam by two rotations;  $\Phi$  and  $\chi$  (see Fig. 3). The  $\chi$  circle is generally symmetrical between the incoming and diffracted beam (positioned at an angle  $\theta$ ). The  $2\theta$  and  $\omega$  axis coincide. The nomenclature

$\Phi$ ,  $\chi$  and  $\theta$  is standard in single-crystal diffractometry and marked on most instruments. Stepper motors, controlled by a personal computer, enable one to obtain any arbitrary angular position on the three axes  $2\theta$ ,  $\chi$  and  $\Phi$  (within a certain range to avoid mechanical collisions). The axis  $\omega$  sets only the detector to the proper Bragg angle,  $2\theta$ , of the diffraction peak of interest.

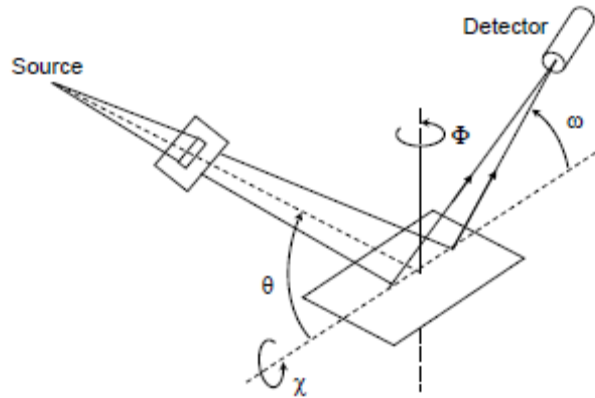


Fig. 3: Ray path and sample rotation in an X-ray texture goniometer and definition of the instrument angles [100].

The movement of the specimen unveils the spatial orientation of the respective poles  $\{hkl\}$ . In a stereographic projection, the measured intensity distribution generates the  $\{hkl\}$  pole figure. A pole figure shows the distribution of a selected crystallographic direction relative to certain directions in the specimen. In the case of magnesium, typical pole figures of interest are  $\{0002\}$ ,  $\{10\bar{1}0\}$ ,  $\{11\bar{2}0\}$ ,  $\{10\bar{1}1\}$ ,  $\{10\bar{1}2\}$ , and  $\{10\bar{1}3\}$ .

Another representation is the inverse pole figure, which is more adequate for showing condensed information on pole figures. This presentation shows the distribution of orientations in a selected direction of the specimen. The projection plane of an inverse pole figure is therefore a standard projection of the crystal, of which only the unit stereographic triangle needs to be shown. Fig. 4 shows the stereographic projection of a standard

representation of an inverse pole figure in the HCP lattice structure. Considering the symmetry of the extruded profiles, inverse pole figures contain most of the relevant information related to the extrusion direction, thus, this presentation will be used in the results.

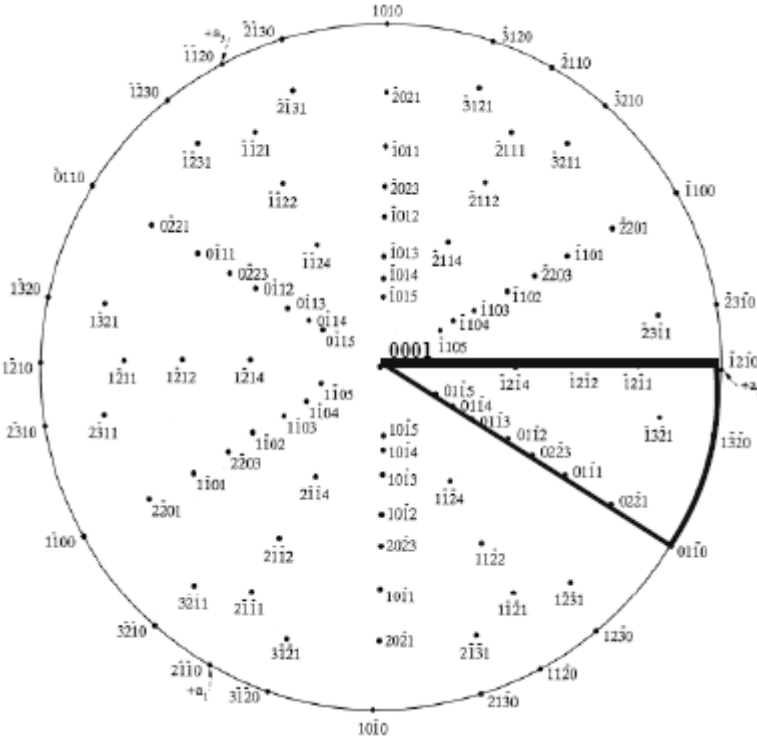


Fig. 4: Standard (0001) stereographic projection of an HCP crystal structure showing a diagrammatic illustration of the inverse pole figure (blue triangle) used in this study for the representation of textures in extruded profiles [24].

**2.4.2 EBSD technique**

As well as the analysis of texture by means of X-ray diffraction, electron backscatter diffraction (EBSD) has become an important tool for texture analysis.

EBSD is a microstructural-crystallographic technique used to examine the crystallographic orientation of many materials, which can be used to elucidate texture or preferred orientation of any crystalline or polycrystalline

material. EBSD can be used to index and identify the seven crystal systems, and as such it is applied to crystal orientation mapping, defect studies, phase identification, grain boundary and morphology studies, regional heterogeneity investigations, material discrimination, microstrain mapping, and using complementary techniques, physico-chemical identification [48]. Experimentally EBSD is conducted using a Scanning Electron Microscope (SEM) equipped with a phosphor screen, compact lens and low light CCD camera. A flat/polished crystalline specimen is placed into the normal position in the specimen chamber, but is highly tilted ( $\sim 70^\circ$  from horizontal) towards the diffraction camera (to increase the contrast in the resultant electron backscatter diffraction pattern). The phosphor screen is located within the specimen chamber of the SEM at an angle greater than or equal to  $90^\circ$  to the pole piece and is coupled to a compact lens which focuses the image from the phosphor screen onto the CCD camera (see Fig. 5). Electrons can backscatter within the material as these backscattering electrons exit the crystal they may exit at the Bragg condition related to the spacing of the periodic atomic lattice planes of the crystalline structure. These diffracted electrons can escape the material and some will collide and excite the phosphor causing it to fluoresce.

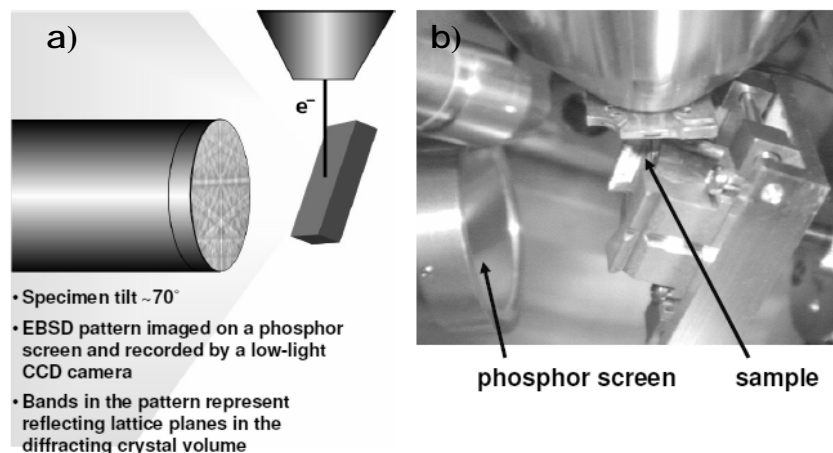


Fig. 5: a) Principles of EBSD technique and b) Setup inside the SEM

An electron backscatter diffraction pattern (EBSP) is formed when many different planes diffract different electrons to form Kikuchi bands which correspond to each of the lattice diffracting planes. If the system geometry is well described, it is possible to relate the bands present in the EBSP to the underlying crystal phase and orientation of the material within the electron interaction volume. Each band can be indexed individually by the Miller indices of the diffracting plane which formed it. In most materials, only three bands/planes which intercept are required to describe a unique solution to the crystal orientation (based upon their interplanar angles) and most commercial systems use look up tables with international crystal data bases to perform indexing.

While this description related to the kinematic solution (using the Bragg condition) is very powerful and useful for orientation and texture analysis, it only describes the geometry of the crystalline lattice and ignores many physical processes involved within the diffracting material [49].

### **2.4.3 Texture analysis during superplastic deformation**

The texture of superplastically deformed materials have been studied over years although the findings are by no means unambiguous. Reasons for this can be attributed, in major part, to differences in the initial microstructure; and in particular to differences in grain shape. However, texture analysis is very relevant to superplastic deformation due to for example:

- 1) Monitoring texture changes during superplastic deformation can help to clarify the relative importance of operating deformation mechanisms.
- 2) Correlating changes in texture and microstructure can elucidate the origins of anisotropic superplastic deformation.
- 3) Calculating properties such as Young's modulus (E) from texture data.
- 4) Producing specific textures in order to favor superplastic deformation [50].

Regarding texture analysis during superplastic deformation of magnesium alloys, Del Valle et al. [51] used EBSD technique for texture analysis as the main characterization technique during tensile deformation of an AZ31 alloy with grain size ranging from 17 to 40  $\mu\text{m}$ , at intermediate temperatures (300-375  $^{\circ}\text{C}$ ). Their results were oriented to the understanding of the deformation mechanisms responsible for the enhanced ductility of such alloy.

Watanabe et al. [52] examined the dislocation creep behavior of AZ31 magnesium alloy with different texture and grain sizes. The results of that work showed that softening by GBS due to finer grain size overwhelms the softening due to texture.

Yi et al. [53] studied the mechanical behavior and microstructure changes of the magnesium alloy AZ31 when deformed in tension at various temperatures, from RT to 250  $^{\circ}\text{C}$ . Their results showed a direct evidence for the high activity of the  $\langle c+a \rangle$  slip systems for temperatures  $\geq 200$  C. The texture intensity recorded in that work showed similar values at all temperatures, even in the sample deformed at 250 C which presented a grain structure mostly created by dynamic recrystallisation (DRX).

Gehrmann et al. [54] used texture measurements to investigate the deformation behavior of magnesium polycrystals. A special emphasis was

laid upon the influence of different starting textures on the deformation characteristics and the development of texture and microstructure.

## **2.5 Processing methods used for getting fine grained Mg alloys**

Wrought magnesium alloys can be processed by conventional thermomechanical treatments like rolling and extrusions.

### **2.5.1 Hot rolling**

Hot rolling is usually carried out in the temperature range between 300°C and 480°C depending on the alloy and the pre-treatment of the feedstock material. Mg-Al-wrought alloys like AZ31 or AZ61 need, for example, an intensive homogenization treatment of up to 24 h at 400°C to dissolve low melting intermetallic phases [15].

Initially the hot deformation process leads to an efficient break down of the comparatively coarse cast or solution treated structure into a fine-grained material, with a medium grain-size of 20 µm and below [55]. A thickness reduction of 10–30% per pass can be carried out without cracking, but the low volumetric heat content of magnesium combined with the comparatively limited process window of hot rolling normally requires several intermediate reheats.

The mechanical properties of sheet processed by rolling are mainly determined by the final grain-size. Beneficial thermomechanical reactions can be activated by controlled interference of work hardening, recovery and recrystallisation effects, which are sensitive to alloy composition, process temperature, deformation parameters, reheating cycles, the final cooling to room temperature and an additional heat treatment [15].

### **2.5.2 Direct and Indirect extrusion [13]**

For the direct process (see Fig. 6a), the metal billet is placed in a container and driven through the die by the ram. A dummy block is placed at the end of the ram in contact with the billet. In the indirect extrusion process (see Fig. 6b), a hollow ram carries the die, while the other end of the container is closed with a plate. The ram containing the die is kept stationary, and the container with the billet is mobile. Because there is no relative motion between the wall of the container and the billet in the indirect extrusion, the frictional forces are lower and the power required for extrusion is less than for direct extrusion. Friction occurs solely between the container and the die.

The advantages of indirect extrusion with respect to the direct method are the lower load required and the development of a more uniform flow pattern because of the absence of relative motion between the billet and the container. Moreover, heat is not produced by friction between the billet and the container. Consequently, there is a considerable reduction in the temperature.

### **2.5.3 Hydrostatic extrusion**

For the hydrostatic process, the billet in the container is surrounded by a fluid, a so called hydrostatic medium. On the stem side the container is sealed with the ram and on the die side with the billet so that the ram can compress the hydrostatic medium without coming into contact with the billet, Fig. 6c The most important feature is that the hydrostatic pressure is

applied to the medium leading to a homogeneous distribution of pressure over the whole surface of the billet. Thus, higher pressures than those available in the other methods can be applied. Moreover, the influence of friction is eliminated because the ram and the container do not touch the billet directly and the die is the only possible place where friction may appear. The lack of friction between billet and container also serves to reduce the extrusion force required. This allows the use of higher extrusion ratios and therefore faster production speeds. Since the heat developed by deformation is not excessive, the limitation of the process is dictated by the ability of the alloy to withstand plastic deformation at low temperatures. Lower process temperatures allow finer grain sizes to be obtained.

Swiosteck et al. [10] showed that hydrostatic extrusion (HE) is feasible thermomechanical treatment for the production of fine grained magnesium alloys. Their results showed that an extremely fine-grained microstructure, excellent ductility as well as enhanced yield strength of the wrought alloys AZ31, AZ61, ZM21, ZK30, ZE10 process at only 100 °C and for AZ80 at 110 °C could be received by this extrusion method. Moreover, the extrusion rates used for processing such alloys were about 8 m/min which is substantially higher than conventional direct or indirect extrusions where the maximum extrusion rates are about 2 m/min.

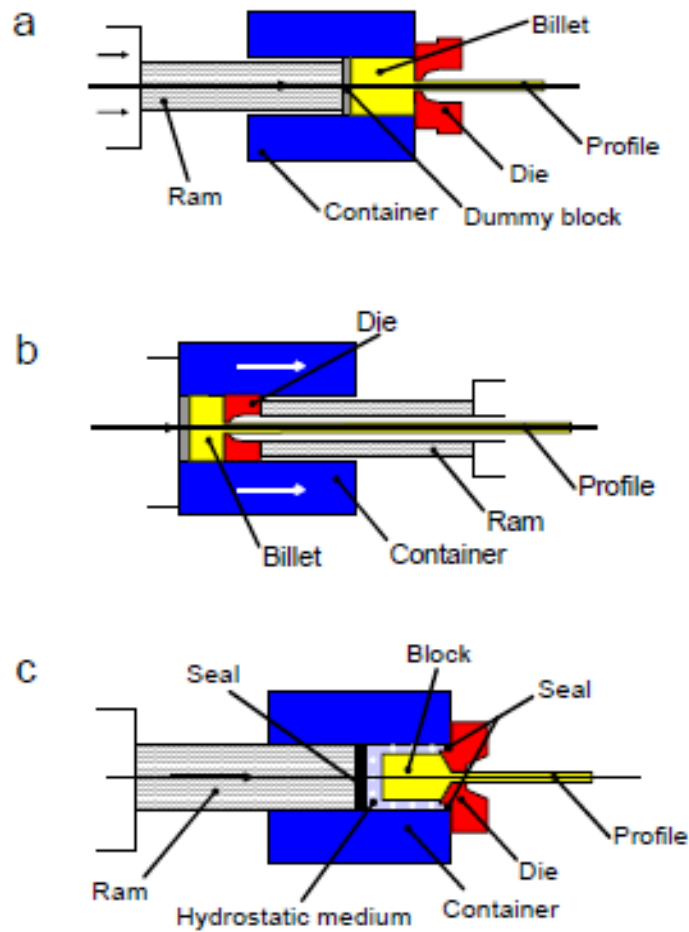


Fig. 6: Scheme of conventional extrusions: a) Direct, b) indirect and c) hydrostatic extrusion.

There is a phenomenon after extrusion of magnesium alloys. Due to the asymmetry of the magnesium's HPC structure and the texturing process after a thermomechanical treatment, the profiles of magnesium alloys show a yield asymmetry  $\Delta\sigma = TYS - CYS$ , when a tensile or compressive load is applied to the textured material. Therefore, a requirement for the commercial application of wrought magnesium alloys is a reduction in the

yield asymmetry, i.e. isotropic mechanical behavior. This difference in the mechanical properties is displayed in Fig. 7.

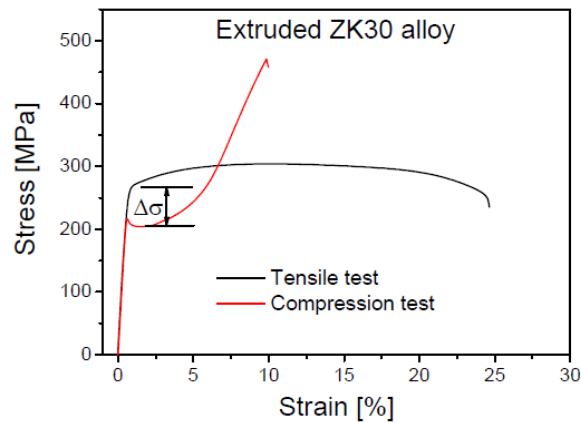


Fig. 7: Engineering stress-strain flow curves of an extruded ZK30 sample loaded parallel to the extrusion direction [13].

This phenomenon has been observed in hydrostatically extruded Mg-Al-Zn alloys [10]. Bohlen et al.[56] studied the microstructure and crystallographic texture from the non-deformed cast part using the remaining billet after hydrostatic extrusion towards the extruded profile. It was demonstrated that an increasing grain size leads to more favored twinning whereas a sole decrease of the  $\langle 10.0 \rangle$  pole density leads to less favored twinning and a lower asymmetry between tensile and compressive yield strength.

#### 2.5.4 Deformation mechanisms active during thermomechanical treatments

During hot rolling or extrusion, the strain rate time profile is usually defined by the process. Hot-working operations such as extrusion are conducted in a high strain rate range of  $10^{-3}$  to  $10^3$  s $^{-1}$  and develop relatively high stresses. Under hot-working conditions all forms of softening processes occur; namely static recovery and recrystallisation, and dynamic recovery and

recrystallisation. In Fig. 8 some possible combinations of dynamic and static softening processes during hot working are shown.

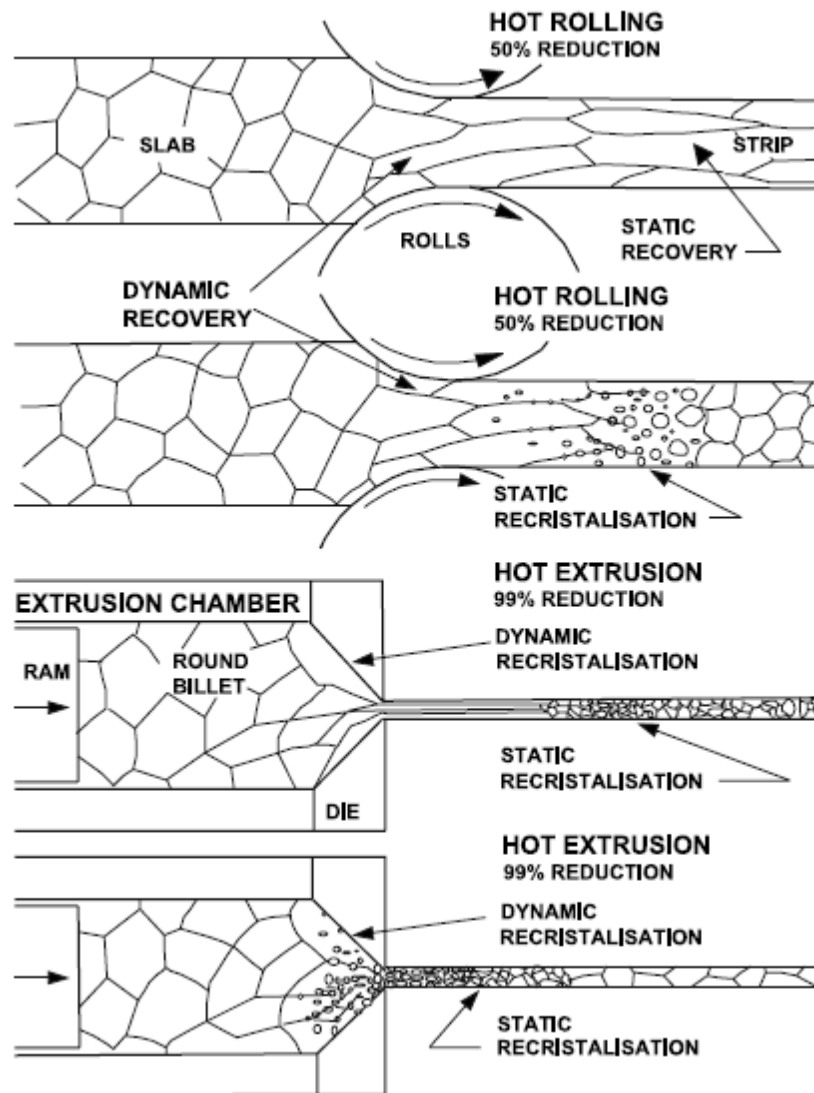


Fig. 8: Schematic representation of possible softening process during hot-working [57]

In magnesium the level of dynamic recovery is sufficiently low to allow dynamic recrystallisation above 240°C. Fine grains are formed at the initial grain boundaries. The product is strengthened due to the substructures from dynamic recrystallisation or refined grains. Magnesium alloys such as AZ31B and ZK60A work harden in the 180–240°C range by deformation

mechanisms induced by twinning [58]. At 300°C, the occurrence of dynamic recovery limits the work hardening. Above 360°C dynamic recrystallisation is observed and ductility is significantly improved. The alloy ZK60A exhibits lower ductility than the alloy AZ31A but becomes stronger at 420°C.

Nevertheless, dynamic recrystallisation is not only restricted to occur during thermomechanical treatments like rolling or extrusion or at temperatures above 240 °C.

For example, Al-Samman et al. [59] performed compression tests at 200, 300 and 400 °C and showed that DRX plays an important role in the deformation of the AZ31 alloy, especially at 200 °C, because at temperatures lower than 225 °C high critical stresses are necessary for the activation of non-basal slip systems.

Yi et al. [53] performed tensile tests on extruded AZ31 alloys with average grain sizes of 4 µm at temperatures between 150 and 250 °C. The results showed changes in mechanical behavior and elongations to failure of about 150 % when the temperature was increased to 250 °C. These results were explained by the high activity of  $\langle c+a \rangle$  slip systems and the occurrence of extensive DRX during the test. In both studies, the flow softening observed in the strain-stress curves during compression or tension was explained by the effect of DRX.

### 3. Experimental procedure

#### 3.1 Melting of the alloys

AZ31, AZ61 and AZ80 magnesium alloys were selected. Billets of all the alloys were produced by gravity casting. They were melted in a steel crucible using a resistance furnace. Alloying element additions were added to the molten magnesium in the crucible at temperatures between 740 and 760 °C, depending on the alloy. Casting was performed under a protective atmosphere mixture of argon and SF<sub>6</sub>. The melt was held for 3600 s under stirring to make sure that the alloying elements were homogeneously dissolved. The alloys were cast into cylindrical steel containers of 0.1 m in diameter and 0.41 m in height. The weight of the cast billets was about 8 kg. The chemical compositions of the cast alloys shown in Table 3. These compositions were determined by spectroscopic analysis using OES Spectrolab™ M equipment.

Table 3: Chemical composition of the selected alloys

Alloy	Al (wt%)	Zn (wt%)	Mn (wt%)	Fe (wt%)	Si (wt%)	Cu (wt%)	Ni (wt%)
AZ31	2.880	0.970	0.259	0.002	0.016	0.001	0.001
AZ61	6.390	0.931	0.204	0.001	0.019	0.001	0.001
AZ80	7.650	0.484	0.279	0.002	0.028	0.001	0.001

#### 3.2 Thermomechanical treatment

The thermomechanical treatment selected to process the alloys was hydrostatic extrusion (HE). To process the alloys, direct chill-cast billets with 0.8 m diameter were homogenized for 12 hr at 350 °C then cooled down in air to room temperature.

Hydrostatic Extrusions on the alloys were carried out in an ASEA-12MN Hydrostatic press (see Fig. 9) at 150 °C with an extrusion ratio of 1:28 and MoS<sub>2</sub> as lubricant in the die exit. The applied load was 700 Mpa. The used extrusion rate was 0.13 ms<sup>-1</sup> to produce bars of 0.015 m in diameter. The extruded bars were water quenched after the extrusion process. Details of the hydrostatic extrusion process can be found elsewhere [10].



Fig. 9: Used ASEA-12MN-hydrostatic-press, Freiberg (Germany).

### 3.3 Metallographic inspection

Specimens from extruded bars for optical microscopy were sectioned parallel to the extrusion direction. Then the samples were cold mounted in resin (DEMOTEC 30). Once mounted, the samples were mechanically grinded with SiC paper grit 800, 1000, 1500 and 2000. For final polishing oxide polishing suspension (OPS) of 0.05 µm was applied on a porous cloth of neoprene (MD-Chem Struers). Instead of cleaning with water in the last step ethanol was used in order to avoid oxidation on the surface.

The polished samples were chemically etched with a solution of picric acid (150 ml of ethanol, 40 ml distilled water, 6.5 ml acetic acid, 3-4 g picric acid) [60]. The grain size was measured with the linear intercept method.

### **3.4 Texture measurements**

Samples for texture analysis were prepared as described for metallographic inspection. However, they were electro chemically polished in a LectroPol-5 (Struers™) electro-polishing device in order to ensure no twins from manual polishing were left. The AC2 commercial solution (Struers™) was used as electrolyte. Optimum conditions for polishing were achieved with an electrolyte temperature of -20 °C and a constant voltage of 16 V for 80 s.

Quantitative texture measurements in as-extruded samples were carried out with a Panalytical™ x-ray diffractometer in reflection geometry using Cu-K $\alpha$  radiation. Six pole figures, (00.2), (10.0), (10.1), (10.2), (10.3) and (11.0), were measured up to a tilt angle of 70° and used to calculate the complete orientation distribution function. Recalculated inverse pole figures in extrusion direction are shown to characterize the texture of the bars. Due to the symmetry of the round bar extrusion, the inverse pole figures (IPF) in extrusion direction contain all relevant information to describe the texture [56].

### 3.5 Tension test at elevated temperatures

Tensile samples with a gauge length of 20 mm and 6 mm in diameter (according with the standard DIN 50125) were machined from the extruded bars with their longitudinal axis parallel to the extrusion direction. Tensile tests were conducted at 175, 200 and 225 °C (see Table 4 for homologous temperature used for each alloy) in air using a universal testing machine (Zwick™ Z050) equipped with an electrical furnace. At each temperature three different strain rates were used  $10^{-2}$ ,  $10^{-3}$  and  $10^{-4}$  s<sup>-1</sup>. An extensometer was attached to the samples to assure an accurate measurement of strain. This extensometer also controlled the strain rate during the whole test. Before starting the test, the samples were held at the selected temperature for 10 min in order to have a homogeneous and stable temperature. When failure occurred, the specimens were immediately quenched in water in order to retain the microstructure and texture at the moment of fracture.

Table 4: Homologous temperature for each alloy used in this work.

	AZ31	AZ61	AZ80
T (°C)	%(Tsol= 565)	%(Tsol= 562)	%(Tsol= 490)
175	0.31	0.33	0.36
200	0.35	0.38	0.41
225	0.40	0.43	0.45

\*Where "Tsol" refers to solidus temperature taken from the ASM handbook [12].

### **3.6 Compression test at elevated temperatures**

In order to compare the characteristic yield asymmetry of magnesium alloys of the series AZ, compression tests were performed with the same parameters as in tension for comparing the behavior of the alloys in both conditions. The compression samples were machined with their longitudinal axis parallel to the extrusion direction having dimensions of 17 mm in height and 11 in diameter. The tests were carried out in the same machine in which the tensile tests were performed. The clamps used for this kind of test were polished to mirror-like surface in order to reduce the friction between the sample and clamp surfaces. In addition to this, boron nitride (BN) was applied on the surfaces as lubricant to prevent the “barreling” of the samples.

### **3.7 EBSD measurements in deformed samples**

With the objective to analyze the final texture after fracture of the samples pulled in tension, EBSD technique was used. The microstructure and texture after deformation were characterized using Electron Backscatter Diffraction (EBSD) in a field emission gun scanning microscope (Zeiss™, Ultra 55, working at 15 kV, equipped with an EDAX/TSL EBSD system with a Hikari detector). The samples were prepared from the fractured specimens. These were mechanically polished with alumina powder of 1 μm and then electro-chemically polished using a Struers™ AC2 solution at 16 V and for 80s. The measurements were taken near the fracture tip with a step size of 0.2 μm.

## 4. Results

### 4.1 Microstructure of the extruded alloys

The microstructures of the extruded alloys are presented in Fig. 10. The extrusion direction lies horizontal. For AZ31 (see Fig. 10a)), a rather inhomogeneous microstructure is revealed, it is composed by large elongated grains resulting from the original cast microstructure. The elongated grains are surrounded by new fine and recrystallised grains. The average grain size is about 5  $\mu\text{m}$ . Fig. 10b presents the microstructure of AZ61. It appears to be more homogeneous and well recrystallised. However, some elongated structures are still visible in the extrusion direction. The average grain size is also 5  $\mu\text{m}$ . In the picture, dark bands are observed where a high concentration of a secondary phase  $\text{Mg}_{17}\text{Al}_{12}$  can be found. Fig. 10c depicts the microstructure of AZ80. The observed microstructure is much more homogeneous than the previous two alloys. For this alloy the etching was more complicated due to high aluminum content which resulted in a very high concentration of secondary phase  $\text{Mg}_{17}\text{Al}_{12}$  that makes easy the over etching. This secondary phase is mainly located on the grain boundaries. Nevertheless, particles are also observed within the grains. The average grain size is 8  $\mu\text{m}$ .

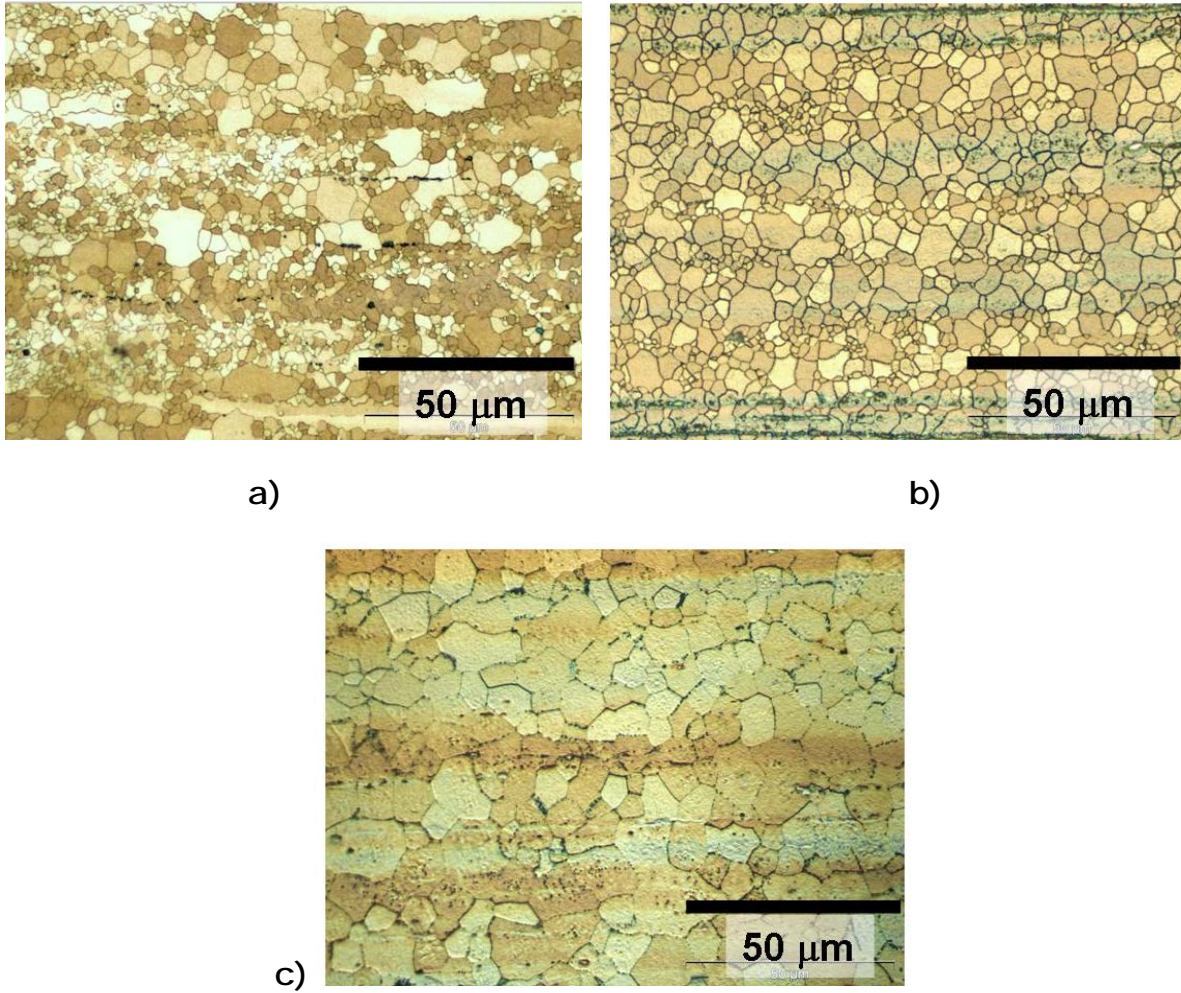


Fig. 10: Microstructure of hydrostatically extruded alloys: a) AZ31, b) AZ61 and c) AZ80.

## 4.2 Macro-Texture

For macro-texture characterization the inverse pole figures (IPF) were used. Due to the symmetry of the round bar extrusion, the IPF contains all relevant information to describe the texture, and, therefore, this representation will be used.

Fig 11a exhibits the corresponding inverse pole figure (IPF) of AZ31 after extrusion. The texture of this alloy is a typical  $\langle 10.0 \rangle$  fibre texture, and the majority of grains are therefore oriented with their basal planes parallel to the extrusion direction. Furthermore, higher intensities are found along the arc between the  $\langle 10.0 \rangle$  and  $\langle 11.0 \rangle$  poles.

The corresponding IPF of AZ61 is depicted in Fig. 11b. The texture of this alloy is basically comparable to the one of AZ31, however, the intensity of the  $\langle 10.0 \rangle$  pole is weaker and the intensity distribution towards the  $\langle 11.0 \rangle$  pole is more significant.

The tendency of changing the component from the  $\langle 10.0 \rangle$  to  $\langle 11.0 \rangle$  pole seen in AZ61 is followed by AZ80 in which the contribution of  $\langle 10.0 \rangle$  pole can be neglected. However, a new texture component  $\langle 10.1 \rangle$  appears between the  $\langle 00.1 \rangle$  pole and the  $\langle 10.0 \rangle$  pole. The maximum texture intensity is located in the  $\langle 11.0 \rangle$  pole (see Fig. 11c).

The maximum intensity of 5.5 multiple random distributions (m.r.d.) for AZ31, 3.3 for AZ61, and 3.5 for the AZ80 alloy.

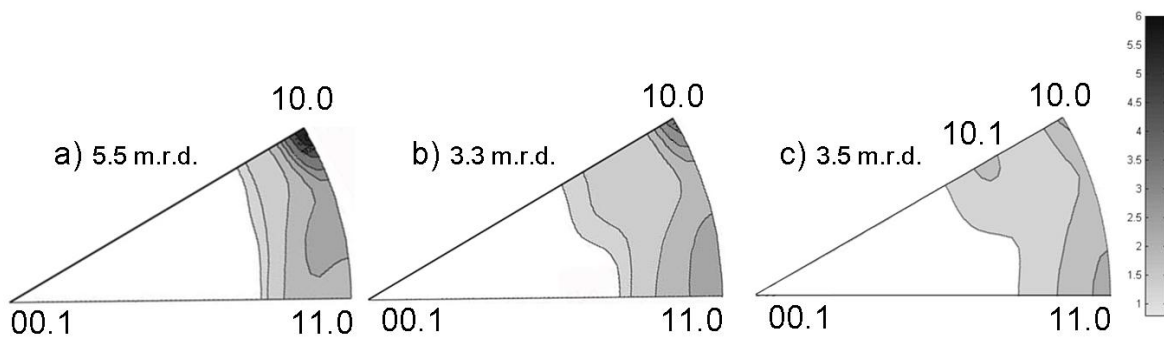


Fig. 11: Inverse pole figures in as extruded condition: a) AZ31, b) AZ61 and c) AZ80.

## 4.3 Mechanical test

### 4.3.1 Room temperature

The engineering stress-strain curves in tension and compression tested at room temperature for the three alloys are presented in Fig. 12.

For AZ31, there is a distinctive asymmetry in the yield strength in which the tensile yield strength (TYS) and compressive yield strength (CYS) are different (Fig. 12a). In contrast, the mechanical behavior of AZ61 and AZ80 showed that the difference between TYS and CYS was significantly reduced (see Fig. 12b and c). Interestingly, AZ31 and AZ61 show similar elongations to fracture in tension, whereas, the ductility of AZ80 was not as high as the previous alloys. On the other hand, all the alloys reached low strain when they were tested in compression. The alloy which showed the higher amount of reduction in height was AZ61. The detailed summary of mechanical properties is presented in table 5.

Table 5: Mechanical properties at room temperature of tested Mg-Al-Zn alloys.

Alloy	Average grain size [ $\mu\text{m}$ ]	TYS [MPa]	CYS [MPa]	UTS [MPa]	UCS [MPa]	e [%]
AZ31	5 $\pm$ 1 (inhomogeneous)	255 $\pm$ 5	225 $\pm$ 4	320 $\pm$ 3	423 $\pm$ 4	22 $\pm$ 1
AZ61	5 $\pm$ 1	223 $\pm$ 2	213 $\pm$ 5	330 $\pm$ 4	430 $\pm$ 4	22 $\pm$ 2
AZ80	8 $\pm$ 1	224 $\pm$ 2	215 $\pm$ 3	355 $\pm$ 5	450 $\pm$ 5	20 $\pm$ 1

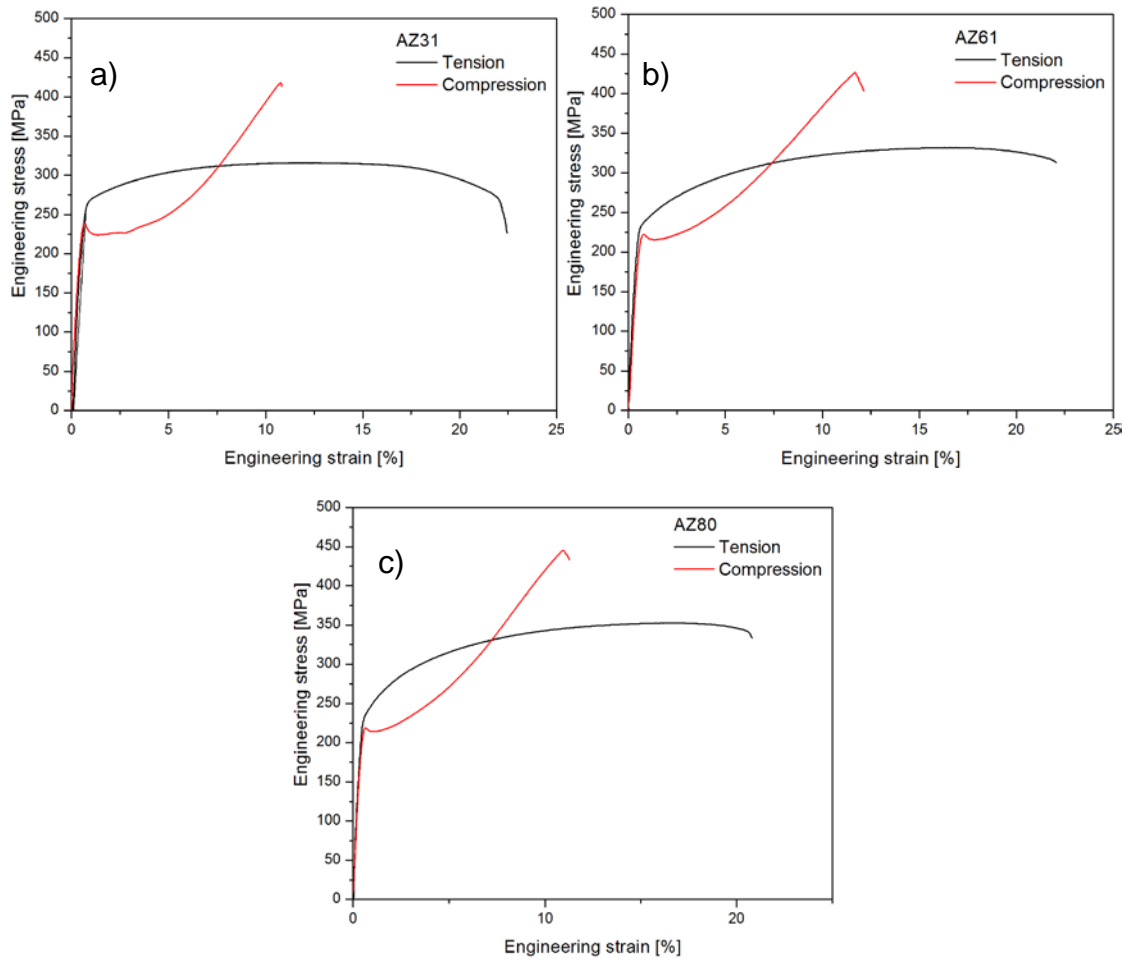


Fig. 12: Engineering Strain-Stress curves in tension and compression at room temperature: a) AZ31, b) AZ61 and c) AZ80.

#### 4.3.2 Tension and compression tests at intermediate temperature

The true stress- true strain curves of AZ31 tested in tension and compression at intermediate temperatures of 175, 200 and 225 °C and  $10^{-2}$ ,  $10^{-3}$  and  $10^{-4}$  s $^{-1}$  are depicted in Fig. 13. For 175 °C, it can be observed when tested in tension, a work softening and an increase in ductility as the strain rate is decreased. The work softening is more marked when plotted in compression.. As the temperature is increased to 200 and 225 °C, the ductility in tension is increased in every strain rate used. However, the work

softening in the lowest strain rate is not as pronounced as the intermediate strain rate of  $10^{-3} \text{ s}^{-1}$ , suggesting that precipitation hardening took place.

In the case of AZ61 alloy, the work softening in the tension tests is more evident compared to AZ31 alloy. There is an important work softening during the first 0.5 true strain in every temperature (see Fig. 14). This effect is clearly seen especially at  $10^{-3}$  and  $10^{-4} \text{ s}^{-1}$ . After this strain, there is a different slope in the curves. It is important to note the high ductility reached by this alloy even at the lowest temperature of  $175 \text{ }^{\circ}\text{C}$ . Interestingly, although AZ61 has higher aluminum content compared with AZ31, there is no sign of a strong precipitation hardening even when this alloy was tested at  $10^{-4} \text{ s}^{-1}$  and  $225 \text{ }^{\circ}\text{C}$ .

The true strain-stress curves for AZ80 are presented in Fig. 15. In contrast with the two previous alloys, the AZ80 alloy tested in tension at  $175 \text{ }^{\circ}\text{C}$  and  $10^{-2} \text{ s}^{-1}$  was able to reach strain about 0.55 and it failed with brittle like behavior. This brittle behavior was reduced by reducing the strain rate at the same temperature. On the other hand, is interesting to note that in compression the material was able to undergo a strain as high as 1.3 true strain without fracture even when tested at  $175 \text{ }^{\circ}\text{C}$  and  $10^{-2} \text{ s}^{-1}$ . When the temperature was increased to  $200 \text{ }^{\circ}\text{C}$ , the brittle behavior was suppressed and the fracture stress in all conditions was rather low. Also, at this temperature lower elongations to fracture were reached in the intermediate strain rate compared to  $10^{-2} \text{ s}^{-1}$ , although, the flow stresses were lower than in the higher strain rate. Conversely, when the temperature was increased to  $225 \text{ }^{\circ}\text{C}$  in the intermediate strain rate, the maximum elongation to fracture was reached. There was a strong work softening followed by a steady state until the end of the test.

In the compression test at  $200$  and  $225 \text{ }^{\circ}\text{C}$ , it can be observed a very similar behavior to the AZ61 in all the strain rates used.

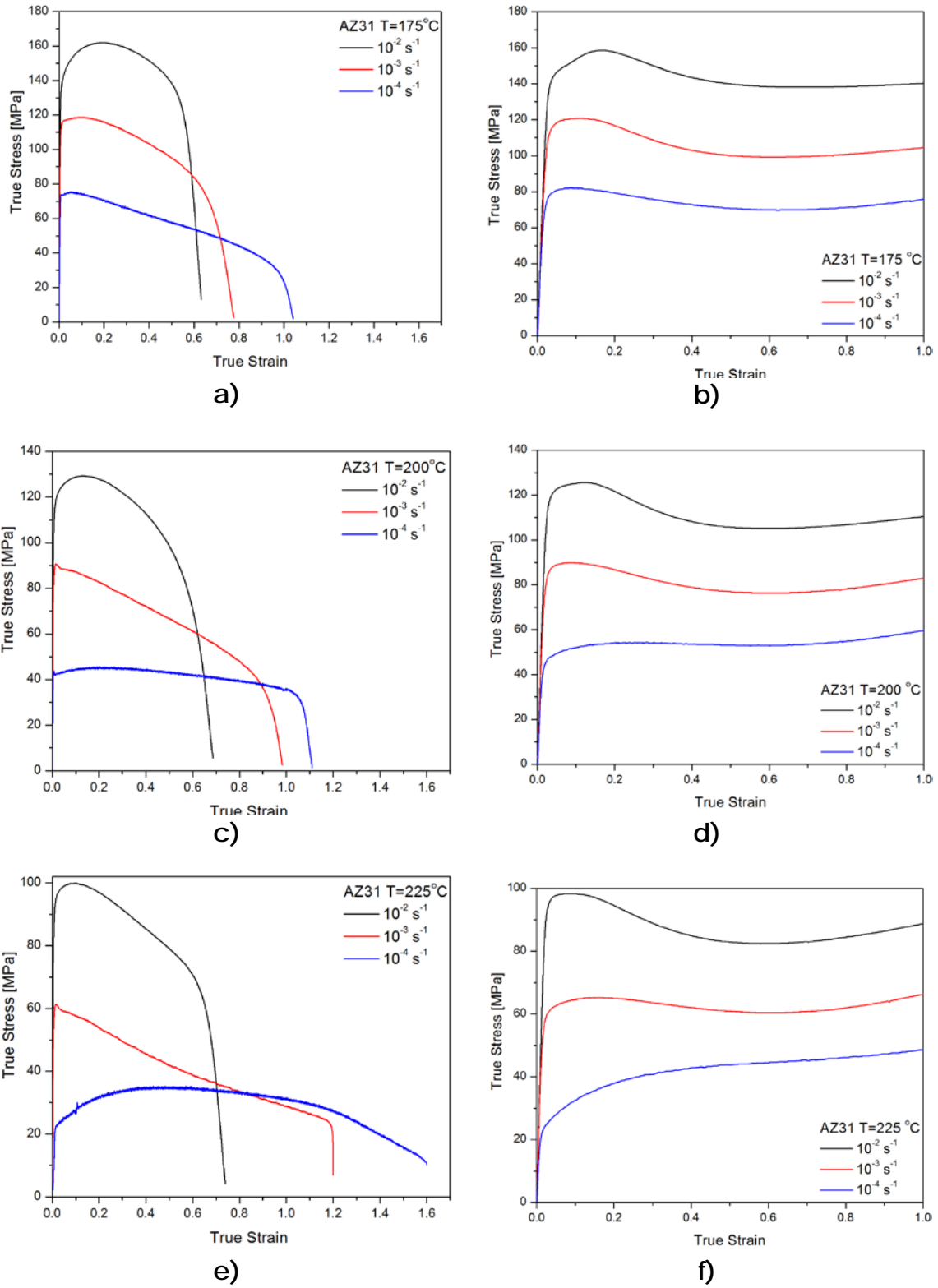


Fig. 13 : True Strain-Stress curves in tension (left) and compression (right) for AZ31 tested at 175 °C a) and b), for 200 °C c) and d), for 225 °C e) and f).

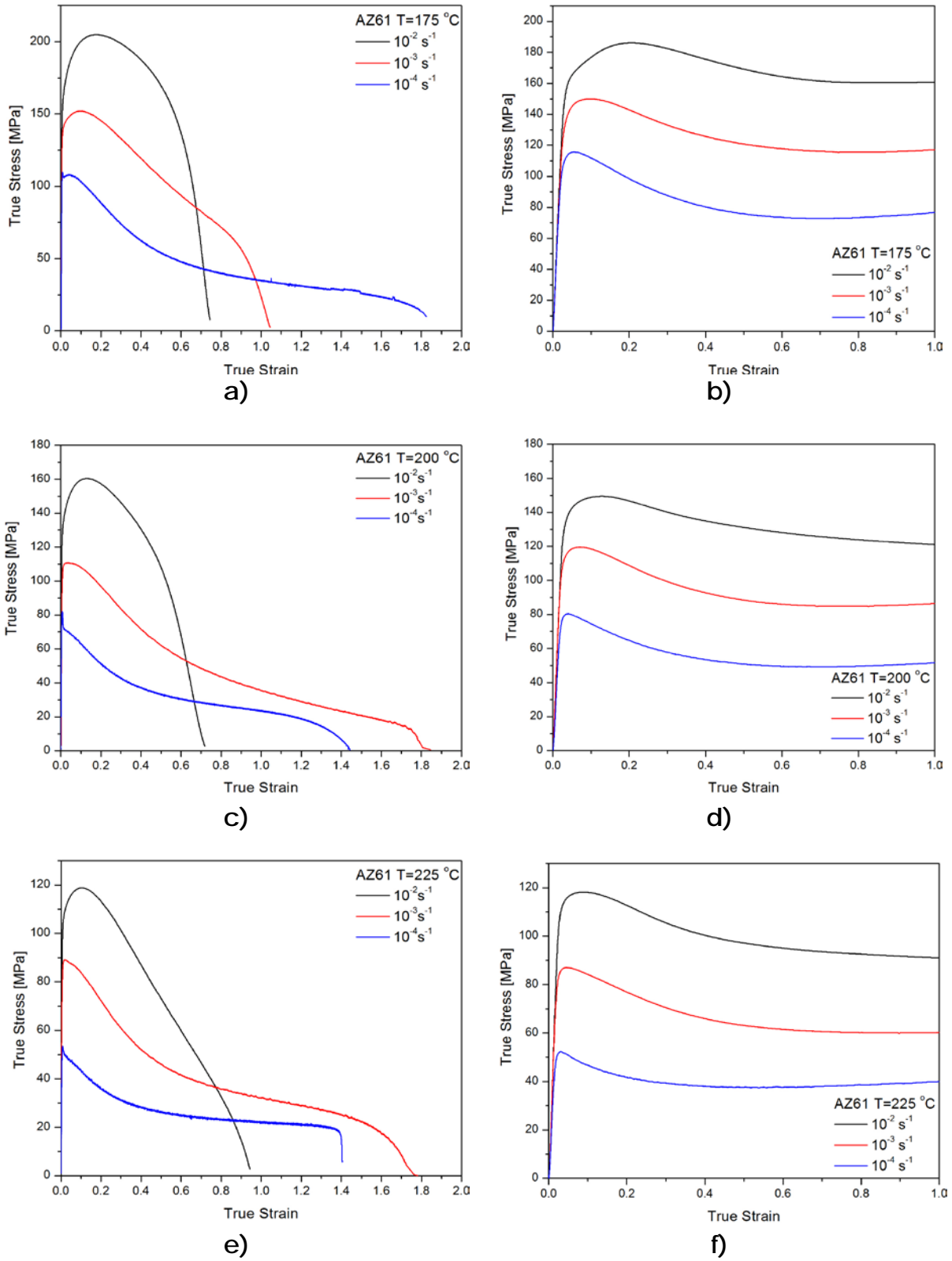


Fig. 14: True Strain-Stress curves in tension (left) and compression (right) for AZ61 tested at 175 °C a) and b), for 200 °C c) and d), for 225 °C e) and f).

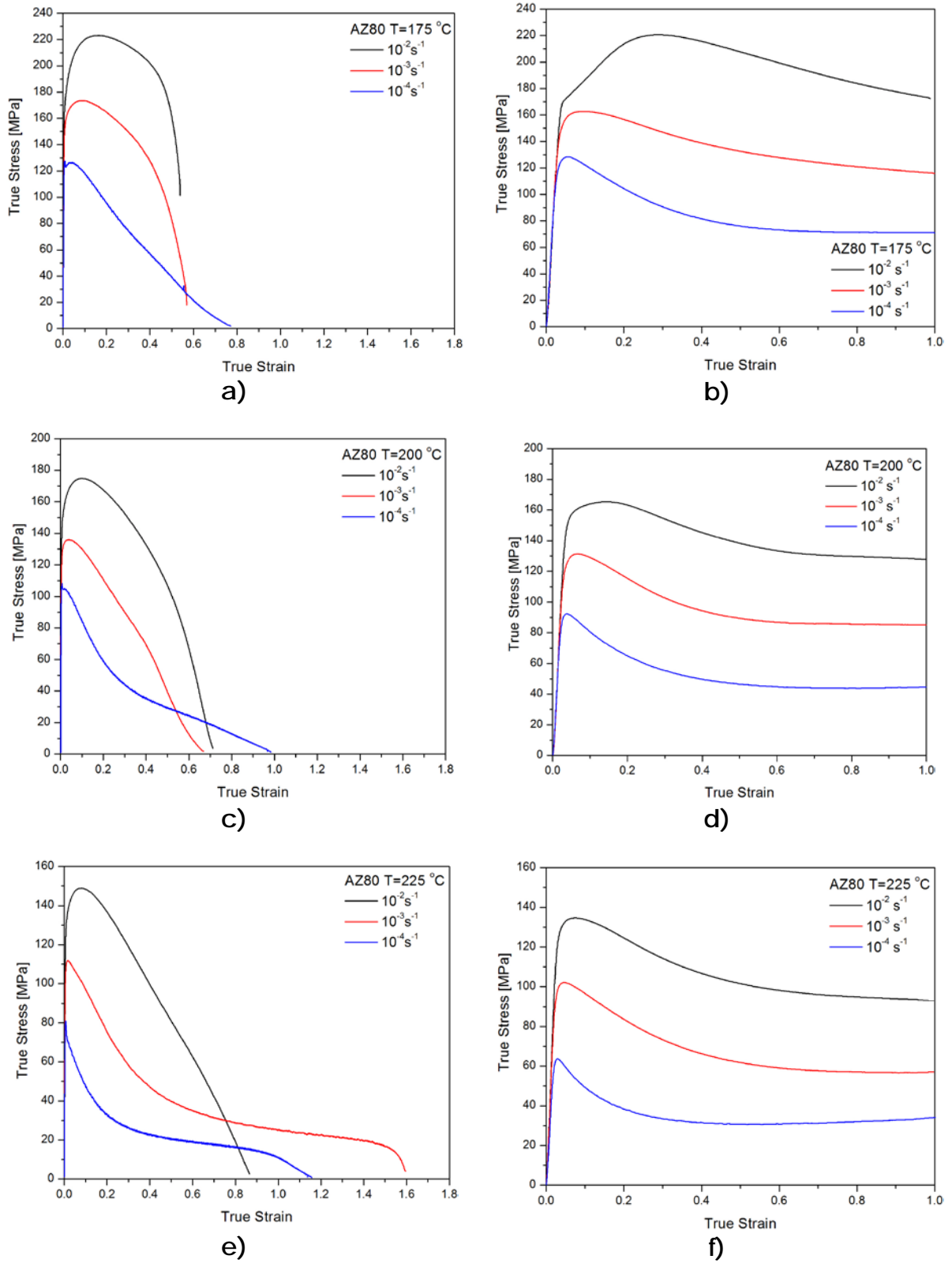


Fig. 15: True Strain-Stress curves in tension (left) and compression (right) for AZ80 tested at 175 °C a) and b), for 200 °C c) and d), for 225 °C e) and f).

#### 4.4 Yield Asymmetry

The results of the TYS and CYS for all alloys tested at intermediate temperatures are plotted in Fig. 16. Fig. 16a presents the results for the AZ31 alloy; this alloy showed comparable yield strength in tension and compression at all temperatures at the highest strain rate of  $10^{-2} \text{ s}^{-1}$ . However, as the strain rate was reduced at all temperatures, the tendency was that the TYS was higher than CYS. This behavior was reduced at  $225 \text{ }^{\circ}\text{C}$ .

For AZ61 alloy when tested at  $175 \text{ }^{\circ}\text{C}$  the results of TYS and CYS were very comparable. Interestingly as the temperature was increased, the CYS had higher value than TYS when this alloy was tested at  $10^{-2} \text{ s}^{-1}$ , but at  $10^{-4} \text{ s}^{-1}$  this tendency changed. The TYS followed the same behavior of AZ31 alloy (see Fig. 16b).

The results of AZ80 showed that the alloy had similar values of TYS and CYS at all the temperatures at  $10^{-2} \text{ s}^{-1}$ . However, there was a clear tendency in lower strain rates used at all the temperatures. The CYS was significantly lower than the TYS, and this behavior increased monotonically as the strain rate was reduced (see Fig. 16c).

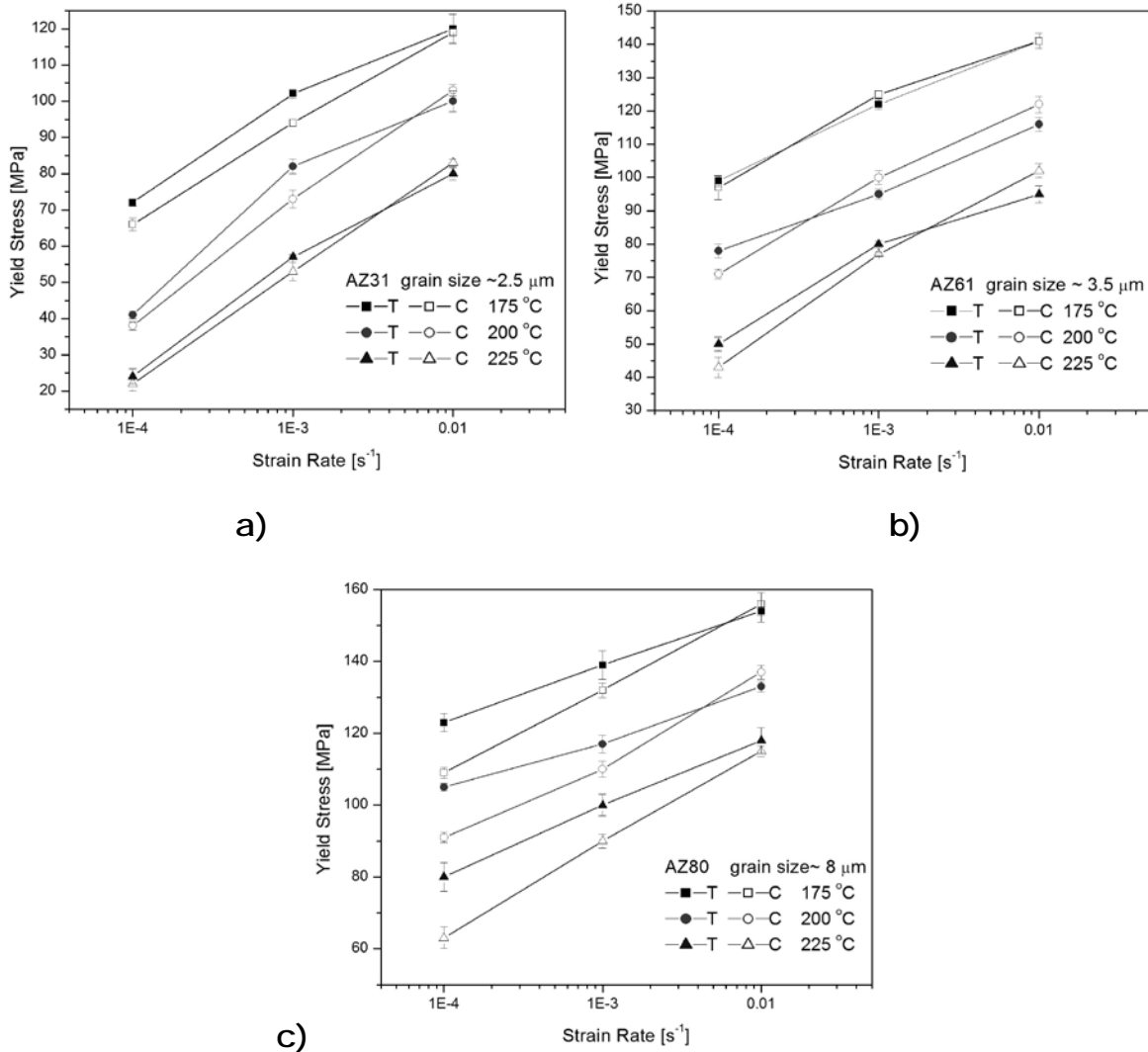
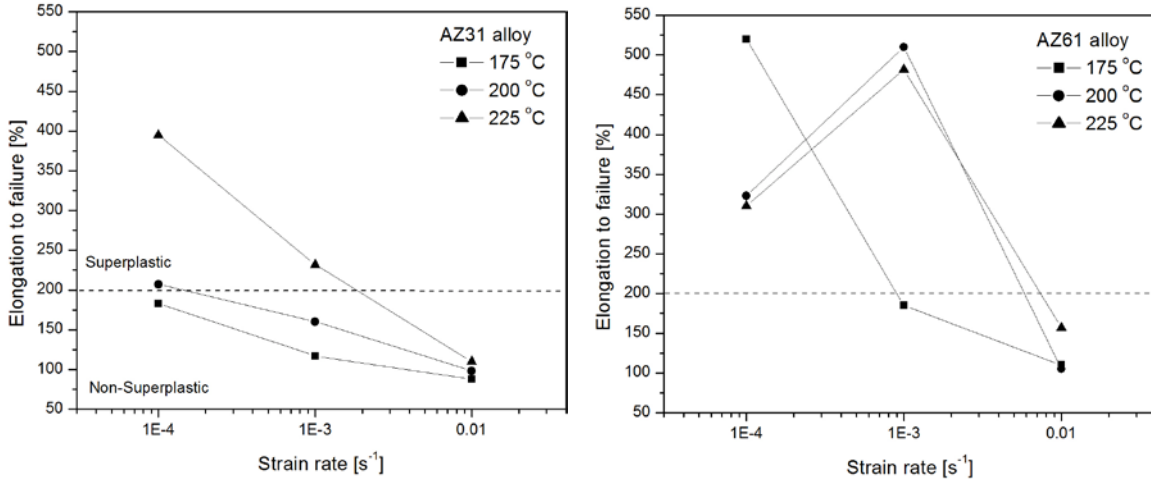


Fig. 16: Tensile and compressive yield strength at different temperatures and strain rates for: a) AZ31, b) AZ61 and c) AZ80 (Filled symbols refer to tension tests whereas filled symbols refer to compression tests).

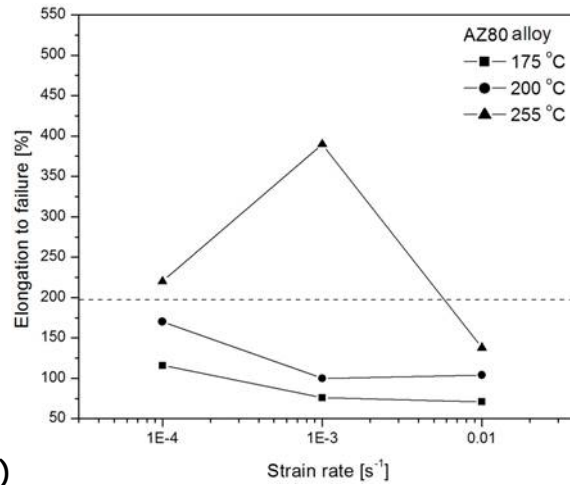
#### 4.5 Elongation to failure of tested alloys

The results of elongation to failure vs. strain rate for all the tested alloys are presented in Fig. 17. It can be seen that the maximum elongation of 400% for AZ31 alloy was achieved at 225 °C and  $10^{-4}\text{s}^{-1}$ . In general for AZ31 alloy, when the strain rate was increased further, the total elongation decreased monotonically at all temperatures (see Fig 17a). In the case of AZ61 depicted in Fig. 17b, high elongation to failure of 160% was recorded at a high strain rate of  $10^{-2}\text{s}^{-1}$ . Interestingly, the maximum elongation was observed at 200 °C and  $10^{-3}\text{s}^{-1}$  instead of 225 °C with the same strain rate. On the other hand, if the strain rate is decreased to  $10^{-4}\text{s}^{-1}$  the alloy showed lower elongation at 200 and 225°C. Conversely, at 175°C the elongation to failure increased monotonically when the strain rate was reduced. At this temperature and strain rate of  $10^{-4}\text{s}^{-1}$ , the alloy showed excellent superplastic behavior, reaching a total elongation to failure of 520%. The AZ80 alloy showed a similar behavior compared to AZ31 when the material was tested at 175 and 200 °C, when the strain rate was decreased the elongation to fracture increased monotonically but the material was able only to reach an strain about 160% at 200 °C and  $10^{-4} \text{ s}^{-1}$  (see Fig. 17c). However, at 225 °C a similar trend as the AZ61 was found; at intermediate strain rate the material showed excellent plasticity reaching elongations of 400%. This capability of reaching these elongations was decreased in the lowest strain rate where the material only reached 220%.



a)

b)



c)

Fig. 17: Elongation to failure vs. strain rate for a) AZ31, b) AZ61 and c) AZ80 alloys tested at 175 °C, 200 °C, and 225 °C.

#### 4.5.1 Flow stress analysis of the tension tests

The logarithm of flow stress vs. logarithm of strain rate is plotted in Fig. 18. The flow stress for each condition was taken from the peak stress of the true stress- true strain curves. The flow stress for the studied alloys increased as the temperature was reduced and the strain rate was increased. In all alloys tested a continuous decrease of the peak stress was observed as the strain rate is reduced.

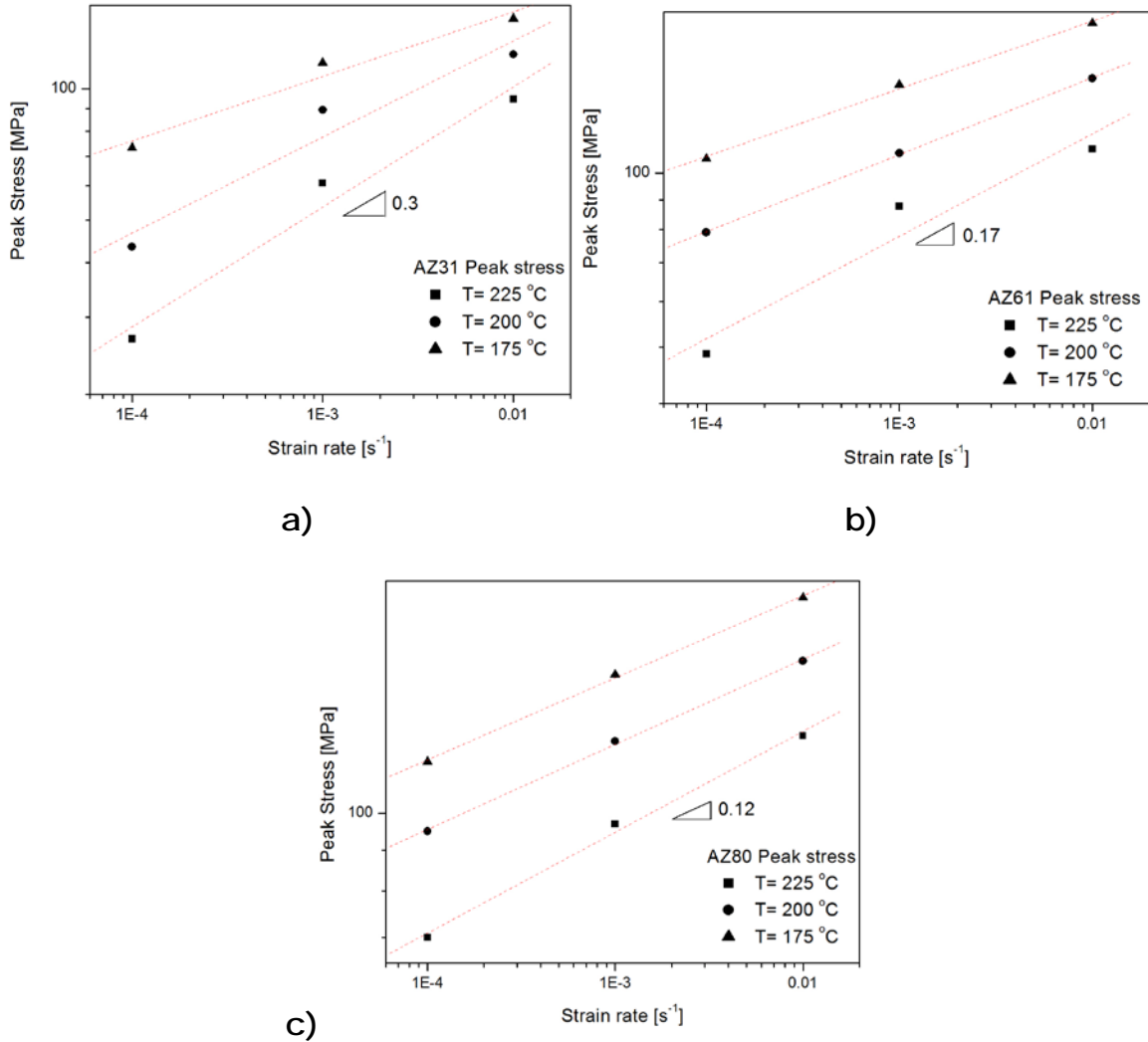


Fig. 18: Peak stress vs. Strain rate for: a) AZ31, b) AZ61 and c) AZ80 alloys tested at 175 °C, 200 °C, and 225 °C .

#### 4.6 Deformed samples

Fig. 19 shows the deformed samples from tension and compression test at room temperature. Due to all alloys showed similar elongation to failure and comparable reduction in height when they were tested in compression,

samples of AZ31 alloy are only presented. In this condition all the alloys behaved brittle.

In Fig. 20a-c the deformed samples from mechanical test at elevated temperatures are presented. In the case of tension test, samples that were able to reach superplastic behavior are presented for each alloy. For these samples, two important characteristics were revealed; first for AZ31, localized neck developed and led to catastrophic failure of the material. However, this neck was less pronounced in the lowest strain rate. Second for AZ61, a diffuse neck rather than localized was observed in almost all samples, just in the lowest strain rate, a localized neck appeared. This behavior was also shown by AZ80.

In compression test (see Fig. 20d) due to all alloys behaved very similar and no cracks were observed, some samples at different degrees of deformation made of AZ31 alloy are presented.

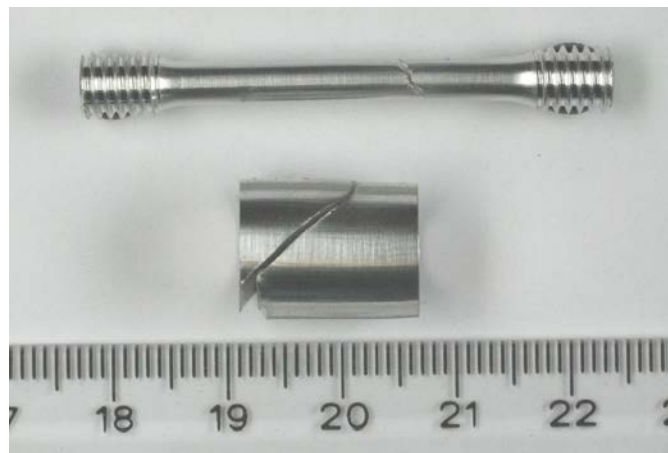


Fig. 19. Deformed samples in tension and compression test at room temperature.

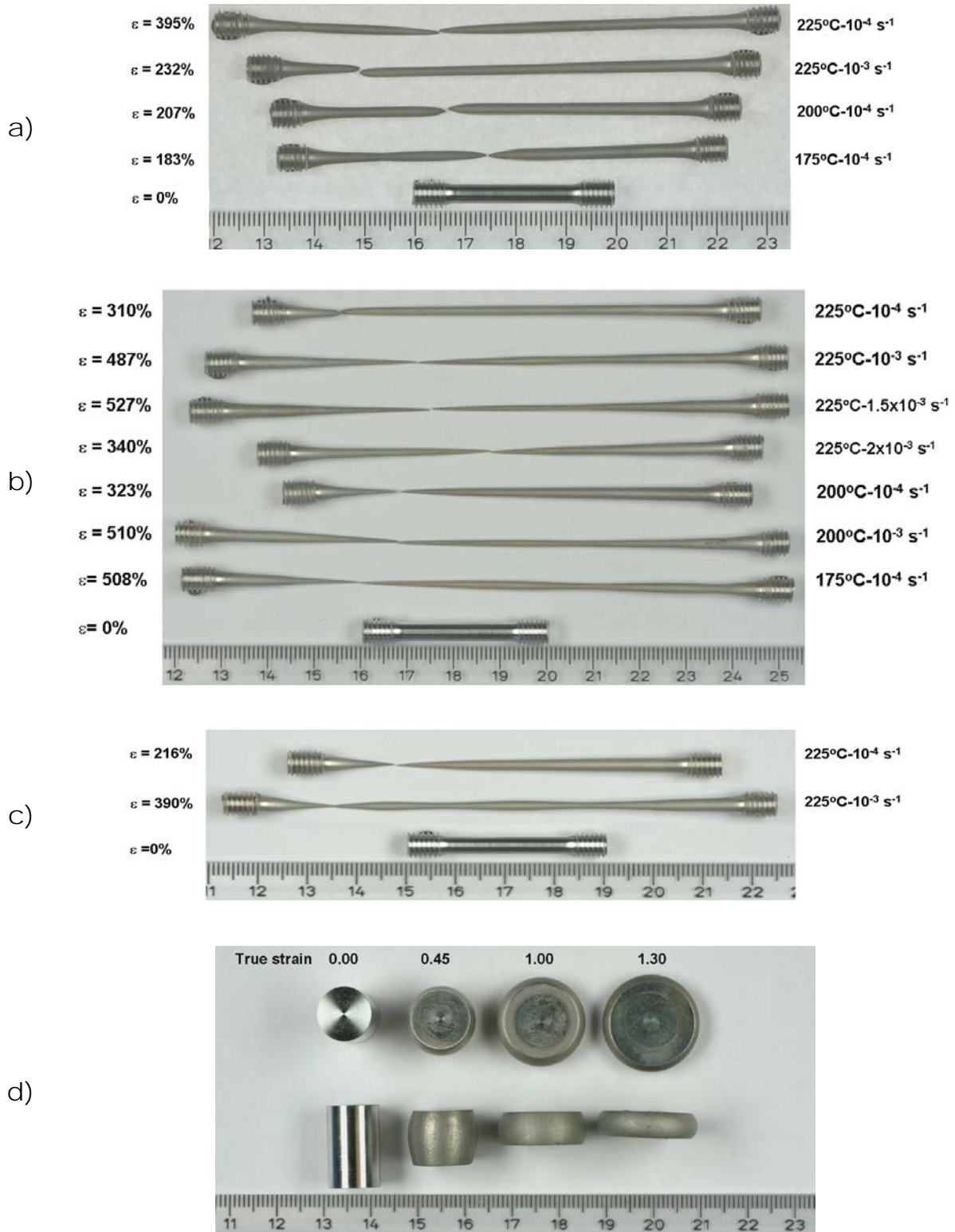


Fig. 20: Deformed samples in tension tested at different strain rates and temperatures for a) AZ31, b) AZ61 and c) AZ80. d) Samples deformed in compression test.

#### 4.7 Micrographs after fracture

The micrographs after fracture in the case of tension tests, and the micrographs of compression tests at 1.0 true strain for AZ31 tested at 175, 200 and 225 °C and strain rate of  $10^{-3} \text{ s}^{-1}$  are shown in Fig. 21. There can be seen that all the large elongated grains from the as-extruded microstructure were recrystallised during the deformation in the tension test at only 175 °C (See Fig. 21 a)) whereas in compression the recrystallisation was not as effective as in tension at the same temperature. A bimodal microstructure composed by newly recrystallised grains and deformed grains was found. (see Fig. 21b)). As the temperature was increased to 200 and 225 °C comparable microstructures were revealed (see Fig. 21 c, d, e and f).

AZ61 shows a comparable recrystallisation behavior in tension than AZ31 tested in the same conditions (depicted in Fig 22a, c and e). However, in compression the duplex microstructure was observed at the three temperatures (Fig. 22b, d and f). Although, the recrystallised grains in the compressed samples were finer than the grains produced in tension there were some coarse and deformed grains that were flattened perpendicularly to the compression direction.

In the AZ80 alloy, the recrystallisation behavior in tension at 175 °C was less effective than in compression (Fig. 23a and b respectively). In compression the bimodal microstructure was observed. This bimodal microstructure was still visible at 200 °C in both tension and compression tests (Fig. 23c and d). Conversely, at 225 °C the recrystallisation was completed in tension and a homogeneous microstructure was found (Fig. 23 e). This tendency of the recrystallisation was observed also in the compression tests at the same temperature where only few deformed grains remained after deformation. The deformed grains were surrounded by new fine recrystallised grains (Fig. 23f).

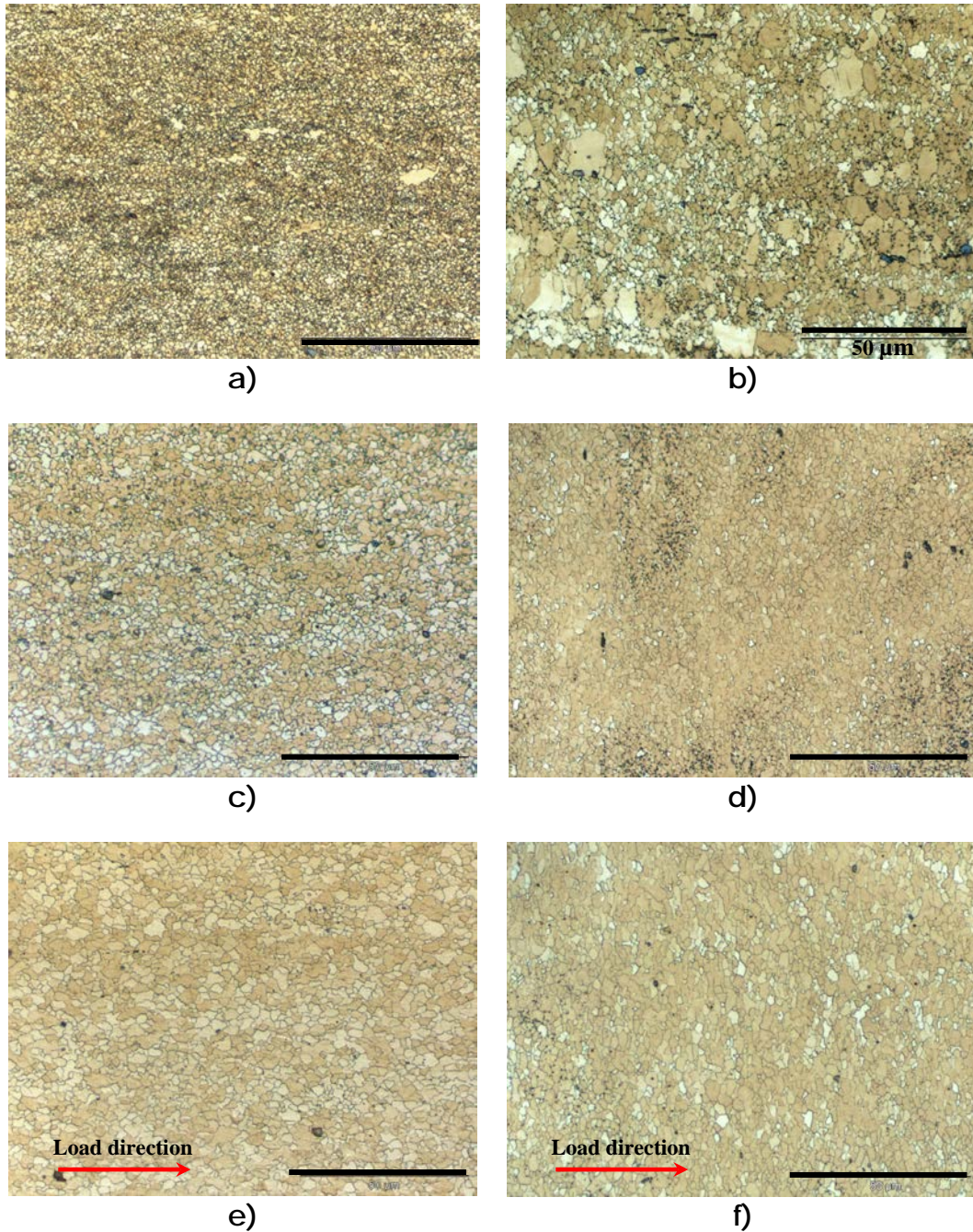


Fig. 21: Optical microstructures of samples deformed in tension and compression (left and right respectively) at strain rate of  $10^{-3} \text{ s}^{-1}$  for AZ31 alloy tested at; 175 °C a) and b); 200 °C c) and d), and 225 °C e) and f).

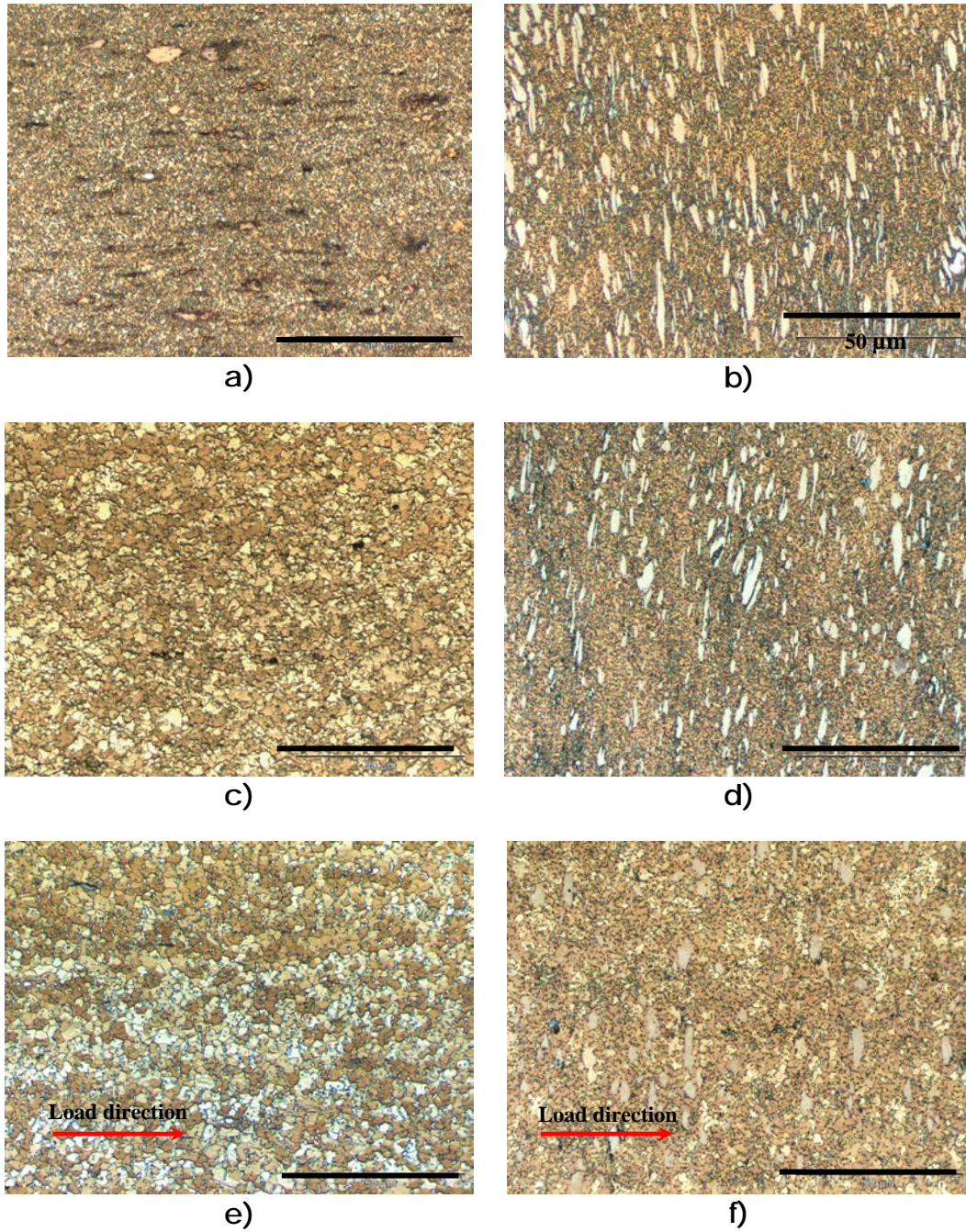


Fig. 22: Optical microstructures of samples deformed in tension and compression (left and right respectively) at strain rate of  $10^{-3} \text{ s}^{-1}$  for AZ61 alloy tested at; 175 °C a) and b); 200 °C c) and d), and 225 °C e) and f).

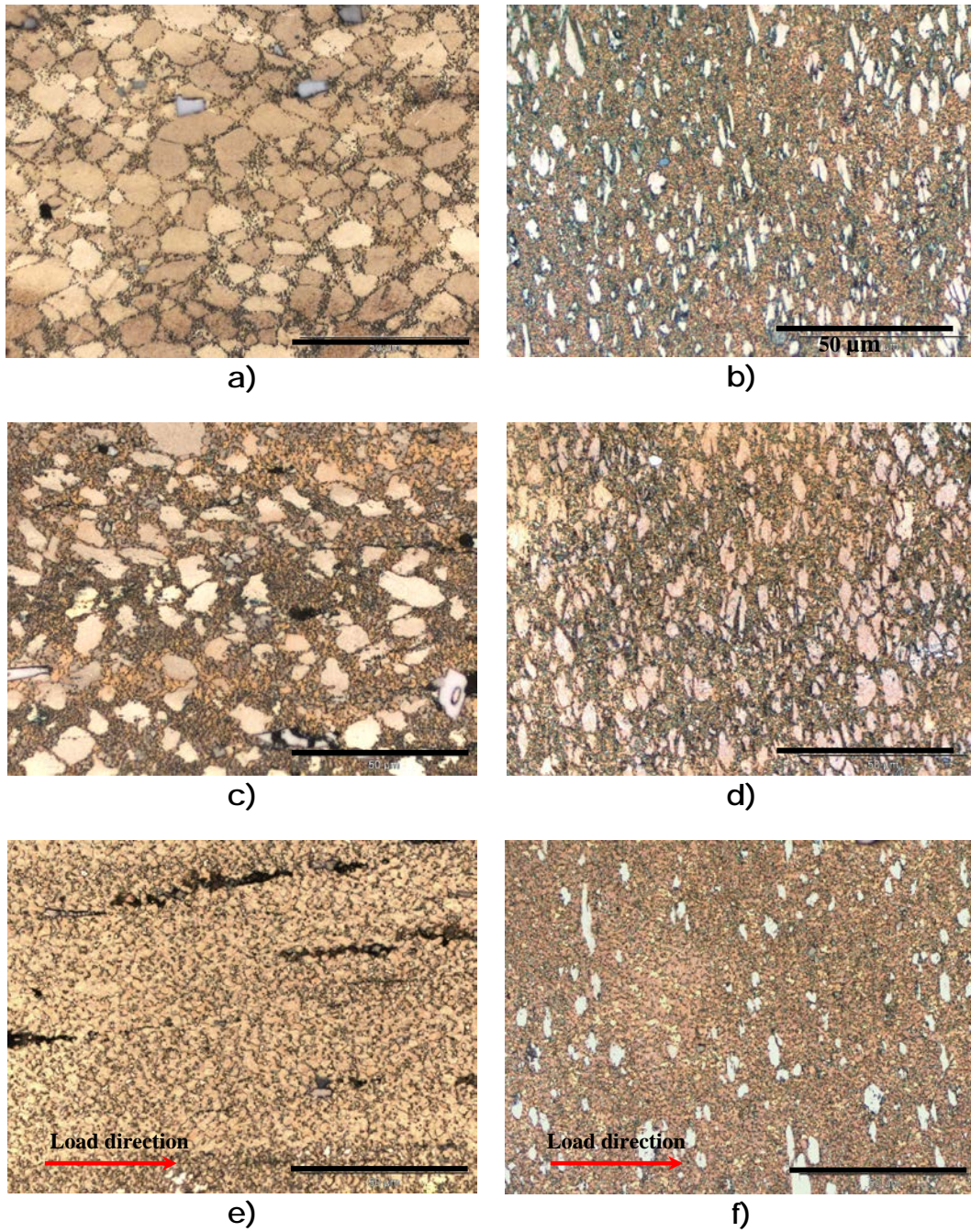


Fig. 23: Optical microstructures of samples deformed in tension and compression (left and right respectively) at strain rate of  $10^{-3} \text{ s}^{-1}$  for AZ80 alloy tested at; 175 °C a) and b); 200 °C c) and d), and 225 °C e) and f).

## 4.8 EBSD analysis

Due to the high aluminum content and the resulting high amount of secondary phase  $Mg_{17}Al_{12}$  found in the AZ80 alloy, the electron backscatter diffraction analysis (EBSD) was not possible (For a good indexing of the Kikuchi patterns of the EBSD analysis is necessary a very flat surface; in the AZ80 alloy the precipitates made a very rough surface, then, the indexing was not good). Therefore, only results of AZ31 and AZ61 will be presented in this section.

The orientation image maps (OIM) for AZ31 tested in tension at 175 and 225 °C and strain rates of  $10^{-2}$ ,  $10^{-3}$  and  $10^{-4}$  s<sup>-1</sup> are presented in Fig. 24.

At 175 °C it can be seen that as the strain rate was decreased the grain size was coarse but more homogeneous and more random distributed. This occurred because in the high strain rate most of the grains were favored oriented to the  $\langle 10.0 \rangle$  component. As the temperature was increased to 225 °C, even in the high strain rate, a random microstructure was revealed. Additionally, a clear tendency can be observed. As the strain rate was reduced grain growth occurred (see Fig. 24 c-f)

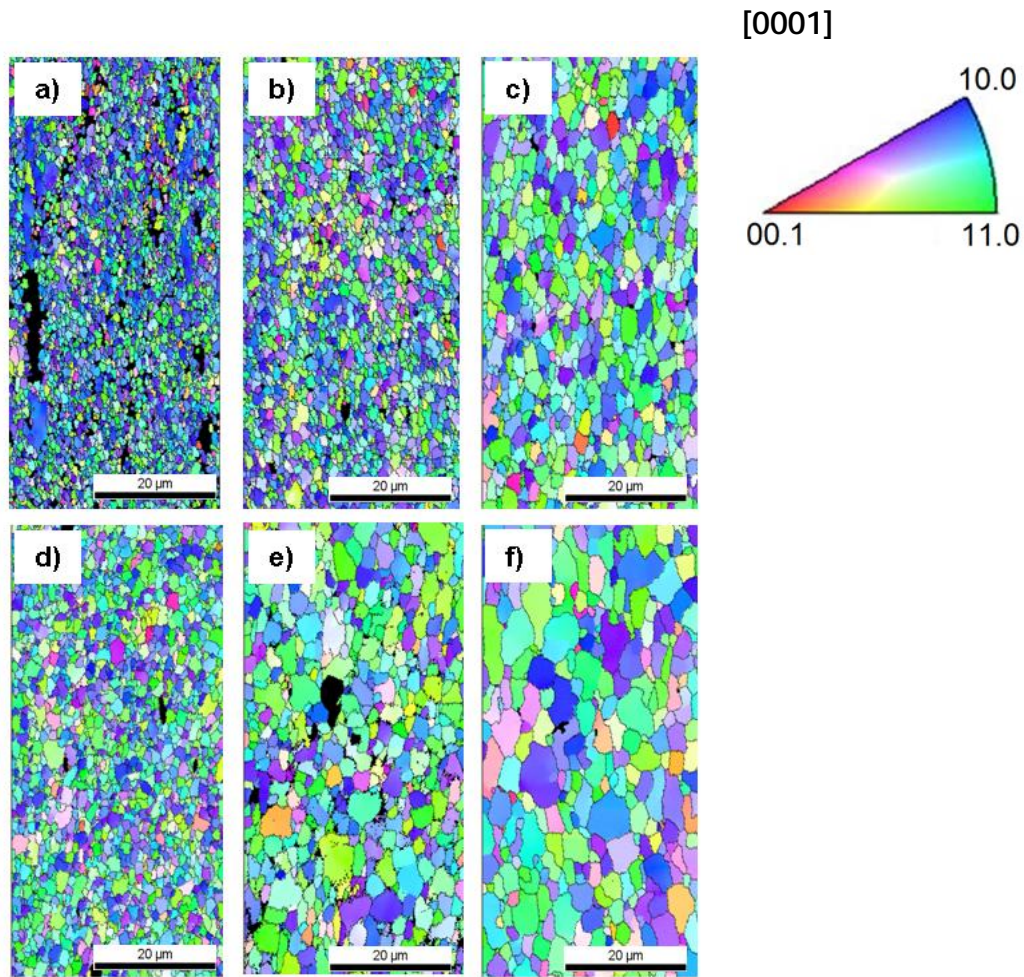


Fig. 24: OIM for AZ31 tested at 175 °C (a-c) and 225 °C (d-f); each temperature three strain rates  $10^{-2}$ ,  $10^{-3}$  and  $10^{-4}$  s $^{-1}$ .

In Fig 25a the orientation maps showed a mixture of deformed grains surrounded by new recrystallised grains for AZ61 when tested at 175 °C and  $10^{-2}$  s $^{-1}$ . In this condition most of the grains were oriented to the  $\langle 10.0 \rangle$  pole. At the same temperature, well recrystallised grains were observed. When the strain rate was decreased, a random distribution of the grains was found (see Fig. 25c). On the other hand, the microstructure shown in Fig. 25d from a sample deformed at 225 °C and  $10^{-2}$  s $^{-1}$  presents a homogeneous microstructure with well recrystallised grains and random

orientation. This tendency was followed by samples deformed at lower strain rates; however, grain coarsening took place as shown in Fig. 25f.

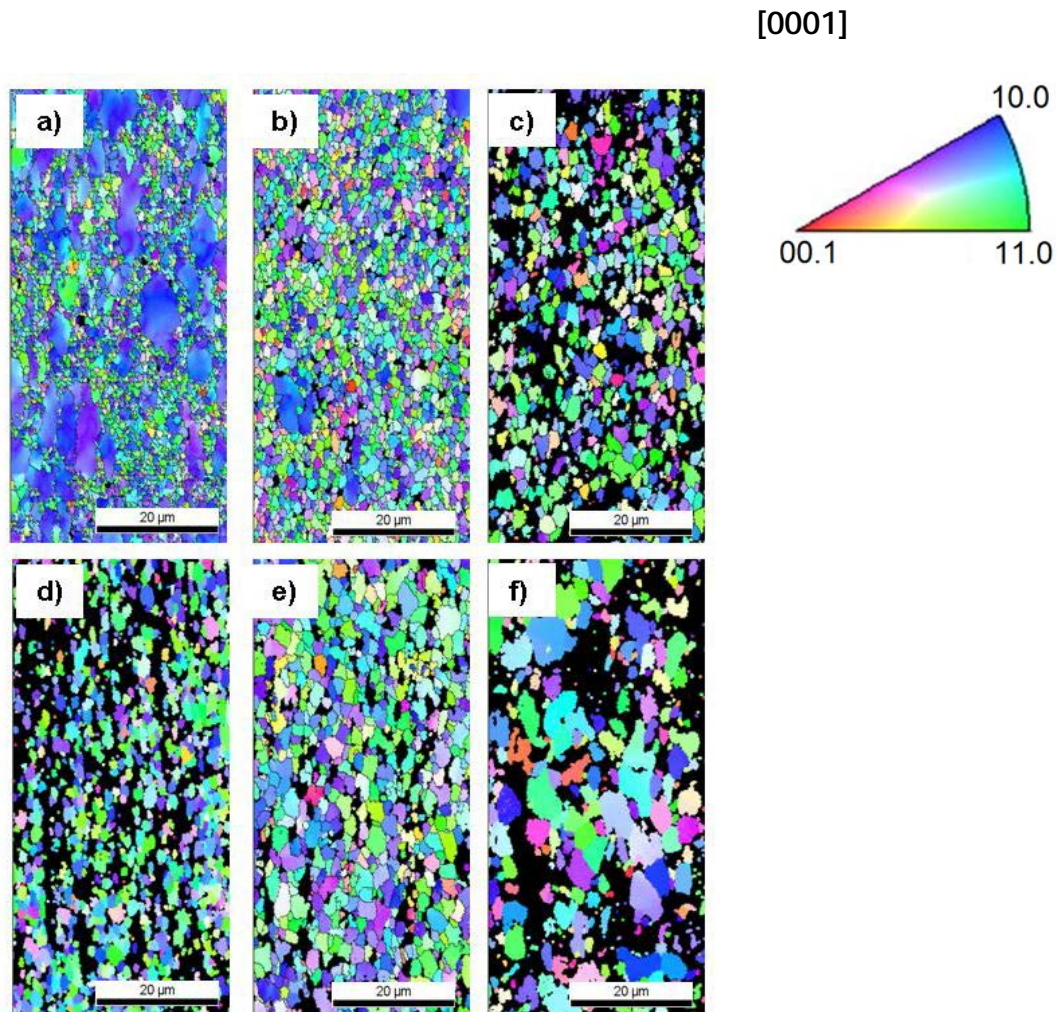


Fig. 25: OIM for AZ61 tested at 175 (a-c) and 225 °C (d-f); each temperature three strain rates  $10^{-2}$ ,  $10^{-3}$  and  $10^{-4} \text{ s}^{-1}$ .

In Fig. 26, the results of the final average grain size after pulling to fracture at all testing conditions are presented. In Fig. 26a, it can be seen for AZ31 alloy that when the temperature was increased or the strain rate was decreased the average grain size increased monotonically. In the case of AZ61 alloy tested at 175 and 200 °C at  $10^{-2} \text{ s}^{-1}$  (Fig. 26b) only a partly recrystallised

microstructure is revealed. It is interesting to note that for AZ31 alloy tested at the same conditions, a fully recrystallised microstructure was revealed. If only the recrystallised grains were considered (which were revealed by restricting the grain size measurement to grains which had orientation spread lower than  $1^\circ$ ) the influence of temperature and strain rate was the same as for AZ31.

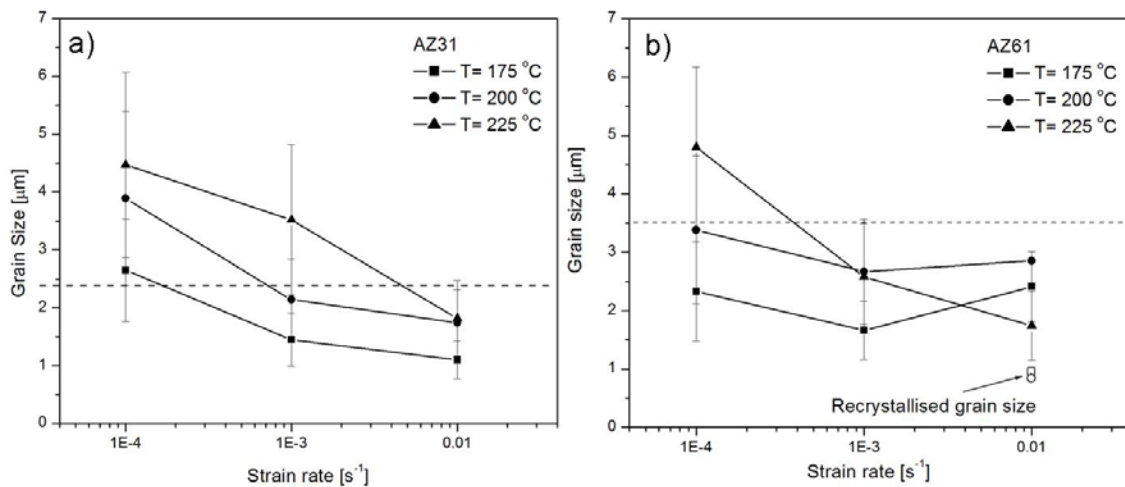


Fig. 26: Average grain size after deformation at different temperatures as a function of the strain rate: a) for AZ31 and b) for AZ61 alloy. (Full symbols give respect to the whole microstructure whereas open symbols refer to recrystallised microstructure only)

#### 4.8.1 Texture of deformed samples in tension

The IPF for samples tested at 175 and 225 °C and  $10^{-3} \text{ s}^{-1}$  are presented in Fig. 27 for both alloys.

The IPF for AZ31 presented in Fig. 27a shows randomization of the texture in which the  $\langle 11.0 \rangle$  component became visible compared to the as-extruded condition. As the temperature was increased and the material underwent

superplastic deformation, the material developed a weak texture and the intensity of the  $\langle 11.0 \rangle$  pole increased (Fig. 27b).

Fig. 27c exhibits the IPF of AZ61 alloy tested in the non-superplastic region. A weak texture with the double fibre components remained after 180 % of elongation. It is worth to note that a very similar distribution was observed in as extruded condition, whereas, in the superplastic region almost a random distribution was found (see Fig. 27d). It is note worthy that in this extremely weak texture, the highest intensities are not found along the arc between the  $\langle 11.0 \rangle$  pole and  $\langle 10.0 \rangle$  poles. The highest intensities were found between the  $\langle 10.0 \rangle$  and the  $\langle 11.1 \rangle$  pole.

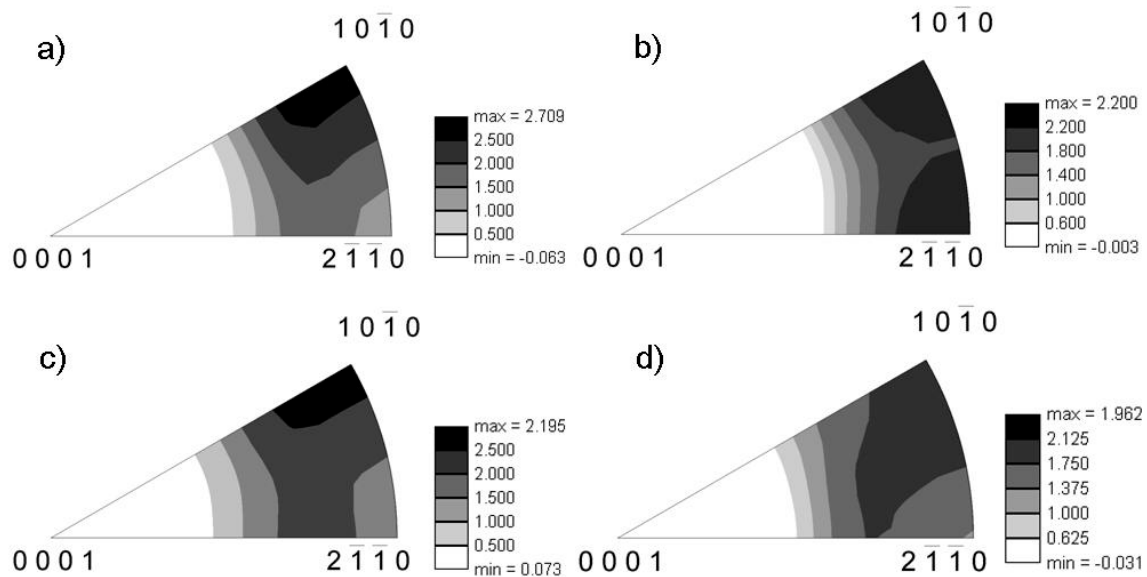


Fig. 27: IPF for samples tested at 175 and 225 °C and constant strain rate of  $10^{-3} \text{ s}^{-1}$ . a) and b) for AZ31, and c) and d) for AZ61 alloy.

## 5. Discussion

### 5.1 Microstructure and texture of as-extruded alloys

Due to the low extrusion temperature and the fact that the extruded bars were quenched in water; static recrystallisation and grain growth were stopped immediately after processing. Therefore, the microstructure was inhomogeneous in the case of AZ31 after extrusion as shown in Fig. 10a.

The strong texture recorded in which the  $\langle 10.0 \rangle$  fibre component was dominant, resulted from a distinct alignment of  $(00.1)$  basal planes parallel to the extrusion direction. This kind of distribution is often found in symmetric extrusion from magnesium alloys. This phenomenon was observed in AZ31 processed by HE at 225, 250, and 300 °C [56]. The results were explained by the incomplete recrystallisation process and the results for the AZ31 HE at 150 °C observed in the present investigation compare well.

In contrast with the observations in AZ31 alloy, AZ61 alloy behaved different. The addition of 3 wt. % more aluminum in this alloy allowed the formation of well recrystallised grains as seen in Fig. 10b, however, in the microstructure there were some deformed grains from the as-cast microstructure. The resulting texture was also slightly different to the found for AZ31. In this case, the intensity of the  $\langle 10.0 \rangle$  pole was weaker than in AZ31 alloy, and a further  $\langle 11.0 \rangle$  pole became visible. This reduction of the intensities can be attributed to a better recrystallisation process in the AZ61 compared to AZ31 alloy. It has been reported that unrecrystallised grains are mainly oriented to the  $\langle 10.0 \rangle$  pole, whereas most of the recrystallised grains tend to orient preferentially towards the  $\langle 11.0 \rangle$  pole [61]. This can explain the double fibre and weaker texture intensity found in AZ61 alloy.

In the AZ80 alloy, the higher aluminum content the better recrystallisation process was obtained. Well recrystallised grains and a homogeneous microstructure were revealed for this alloy. Also the IPF showed a dominant  $\langle 11.0 \rangle$  pole, this followed the trend of AZ61 with increasing the aluminum content. Nonetheless, the recorded texture intensity was slightly stronger than the recorded in AZ61 alloy. That means that most of the prismatic planes (11.0) in AZ80 alloy were oriented parallel to the extrusion direction. Besides, a new texture component  $\langle 10.1 \rangle$  developed in which the (10.0) planes were tilted about 30 °C towards the  $\langle 00.1 \rangle$  pole.

## **5.2 Mechanical test**

### **5.2.1 Room temperature.**

The anisotropy of mechanical properties is always a concern when working with magnesium, it is expected that based on the hexagonal lattice structure of magnesium alloys a strongly orientation dependent deformation behavior is caused. This phenomenon would lead to a distinct difference between tensile and compression yield strength that limits the application of magnesium alloys at industrial scale [62].

In table 5, the summarized results from the mechanical tests were presented. In all alloys tested, the tensile yield strength was slightly higher compared to the corresponding compressive one. This behavior can be attributed to twinning. This deformation mechanism is a dominant orientation dependent deformation mechanism in magnesium alloys and it is promoted since the c-axis laid perpendicular to the tension/compression direction [10].

AZ31 alloy showed higher asymmetry in the yield strength. This could be attributed to the inhomogeneous microstructure where large elongated grains were revealed. Due to these grains were oriented parallel to the extrusion direction, all of them were more prone to present tensile twins  $\{10\bar{1}2\}$ , therefore, reducing the yield strength in compression [18]. The tensile twins inside large elongated grains are presented in Fig. 28.

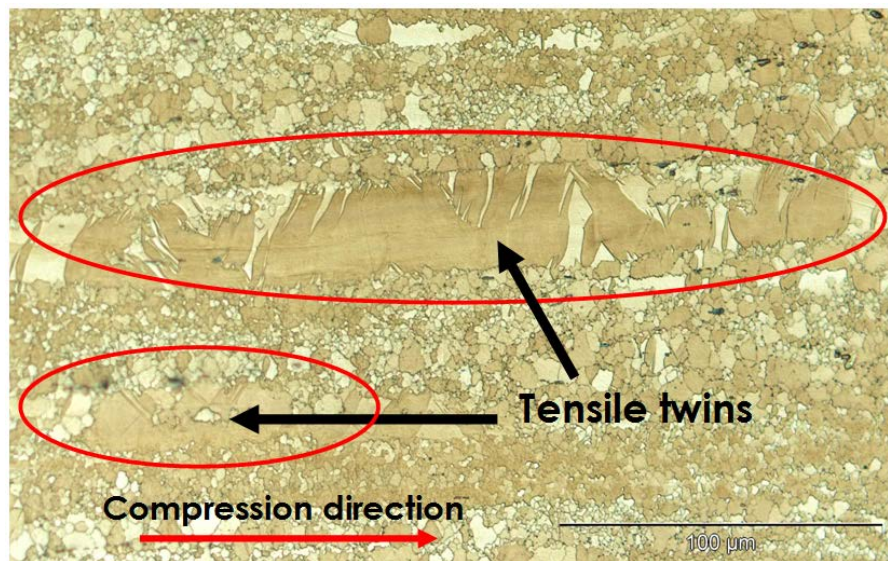


Fig. 28. Tensile twins  $\{10\bar{1}2\}$  observed in large elongated grains in AZ31 alloy during compression test at room temperature.

Conversely, in AZ61 and AZ80 alloys which showed more homogeneous microstructure the yield asymmetry was less pronounced than in AZ31 alloy. It is well known that for small grains twinning is less important [63] which results in the reduction of the yield asymmetry.

There is another observation, although, AZ61 and AZ80 alloys have more aluminum content than AZ31 alloy, the AZ31 alloy had higher value of tensile yield strength. One possible reason is the finer average grain size of this alloy i.e. 5 μm than 8 μm of the AZ80. It is known that the yield strength

of alloys with small grain sizes tends to result in higher values. This observation is in agreement with the Hall–Petch relationship [64]. However, there is another possible explanation. The lower texture intensity of AZ61 and AZ80 compared to the intensity of AZ31 could reduce the yield strength of both alloys.

Materials with strong textures are responsible for an intrinsic plastic anisotropy, low elongation and limited formability. Materials with weaker and more random textures, however, promise improved formability and reduced mechanical anisotropy [65]. This is in agreement with the result obtained from the tension and compression tests.

These findings from hydrostatically extruded Mg-Al-Zn alloys compared well to the reported by Swiosteck et al. [10] for the same series of alloys at processed by hydrostatic extrusion at 100 °C for AZ31 and AZ61, and for AZ80 at 110 °C and tested at room temperature.

### **5.2.2 Intermediate temperatures**

In general from the true stress-strain curves of AZ31 in tension and compression, it can be seen that the flow stress was reduced when the temperature was increased and when the flow stress reached the peak stress, it was followed by work softening.

This reduction in the flow stress suggests that dynamic recrystallisation (DRX) took place. For a metal which presents DRX, initially the flow stress increases with strain due to being dominated by strain hardening, and as DRX takes place upon a critical strain, the flow stress begins to decrease after it

reaches certain peak value. When equilibrium is reached between softening due to DRX and strain hardening, the curves drop to a steady-state region [66].

This phenomenon fits with the behavior observed in AZ31 alloy tested in tension and compression tests at 175, 200 and 225 °C. Taking into account the melting temperature of pure magnesium ~650 °C, the recrystallisation observed in this investigation can be referred to low temperature dynamic recrystallisation (LTDRX).

It is interesting to note that even at 175 °C the alloy was able to reduce the fracture stress at very low values without abrupt fracture when the samples were tested in tension. Also, no evidence of cracks was observed in compression tests at all temperatures and strain rates even at large strains of 1.3.

There is another interesting phenomenon occurring during the deformation of this alloy. Especially at lowest strain rate, the DRX rate was less pronounced than at moderate and high strain rates for the AZ31 alloy. There was a clear competition between work softening and strain hardening from 200 °C at  $10^{-4} \text{ s}^{-1}$ . This behavior was much more evident at 225 °C. It is well known that precipitation of the secondary phase  $\text{Mg}_{17}\text{Al}_{12}$  starts at 180 °C [12]. Therefore, it can be assumed that precipitation hardening took place during this specific test. This kind of behavior has been observed by Cottam et al. [67] for magnesium alloys. For comparison of the amount of precipitates two pictures were taken, one from the as-extruded AZ31 alloy and the second one from a sample deformed at 0.2 true strain at 225 °C and  $10^{-4} \text{ s}^{-1}$ . A slight higher amount of precipitates was found in the deformed sample compared to the as-extruded one (see Fig. 29). Due to the grinding process many precipitates were removed. However it can be assumed that most of the voids observed in both

pictures correspond to places where precipitates of  $Mg_{17}Al_{12}$  were removed.

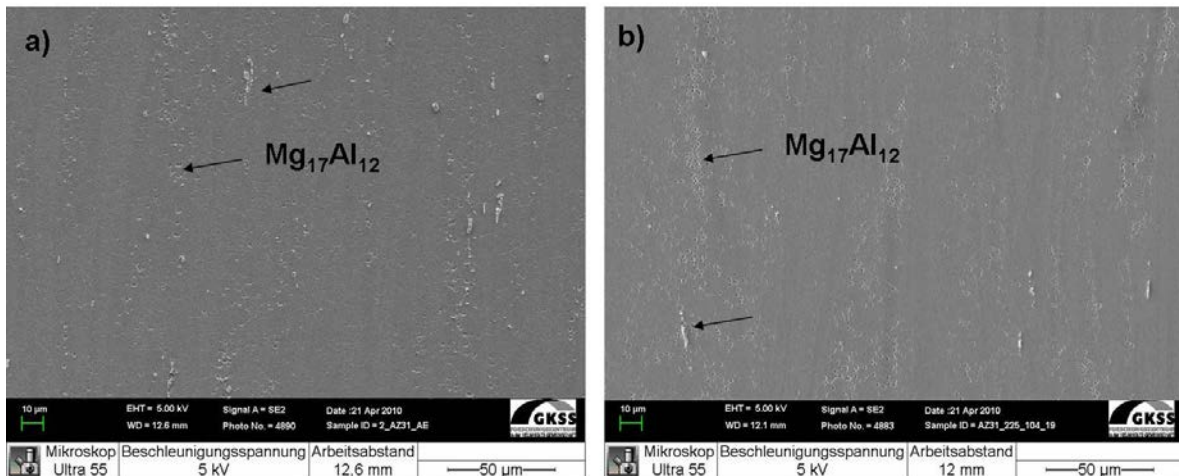


Fig. 29: Secondary phase present in AZ31 alloy; a) as-extruded condition and b) sample deformed 0.2 true strain tested at 225 °C and  $10^{-4} s^{-1}$ .

As the aluminum content was increased in the case of AZ61 alloy, the slope of the true strain-stress curves was more pronounced. This suggests that the recrystallisation suffered by this alloy was more important than in the AZ31 alloy. However, it is important to note that this tendency was also seen in the extrusion process, since better recrystallised grains were obtained in this alloy.

Besides, in contrast to the observation of precipitation hardening exhibited in a sample of AZ31 tested at 225 °C and  $10^{-4} s^{-1}$ , AZ61 alloy tested at the same conditions did not follow the same tendency. Although, AZ61 had more aluminum content to form secondary phase, there was no clear evidence of a strong hardening due to precipitation during tension and compression tests. Thus, it seems that the work softening due to DRX exceed the precipitation hardening in this alloy.

AZ80 alloy behaved quite similar to AZ61 alloy, the work softening strongly influenced the slope of the true strain-stress curves in tension and compression.

Even more interesting to note from all curves is that the slope of the stress-strain curves of the tension tests changes in a range from 0.2 to 0.6 of true strain (see Figs. 13, 14 and 15). Tan and Tan [68] pointed out that DRX takes place during the first 60% (approximately 0.5 of true strain) of strain in AZ31 alloy. They proposed a two-stage deformation method. In the first stage a tensile sample of AZ31 rolled sheet was pulled at relatively low temperature of 250 °C at a strain rate of  $10^{-4} \text{ s}^{-1}$ . This deformation refined the microstructure by means of DRX from 12  $\mu\text{m}$  as rolled to 6  $\mu\text{m}$  after 60% of strain. The stage II was at 400°C –  $2 \times 10^{-4} \text{ s}^{-1}$  where superplastic like behavior was found.

This phenomenon fits with the behavior of AZ61 and AZ80 alloy at similar strains. This leded it to a different microstructure compared to the as-extruded condition, thus, LTDRX generates equiaxed grains.

Exemplarily two micrographs were taken from a couple of samples made of AZ61 alloy deformed under tension at 200 °C and  $10^{-3} \text{ s}^{-1}$ . The first one reached a strain about 0.2 (see Fig. 30a) and the second one was deformed up to 0.5 true strain (see Fig. 30b).

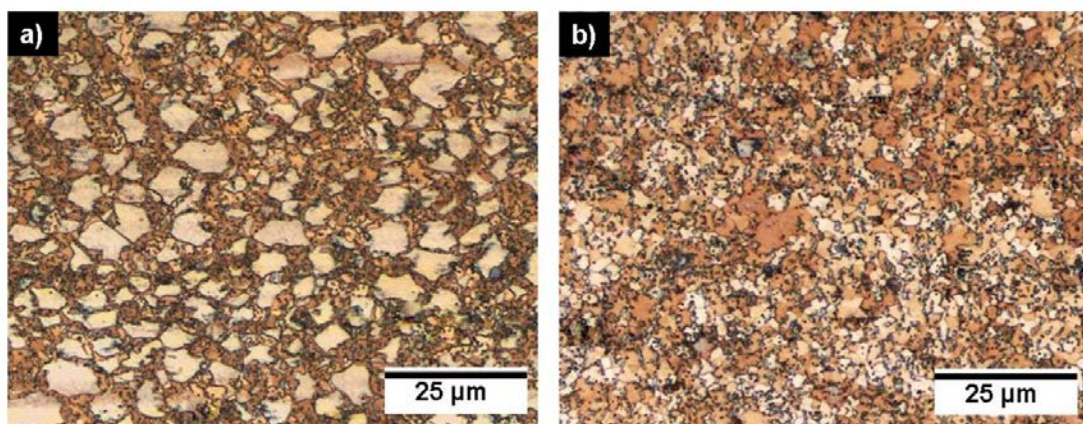


Fig. 30: Optical micrographs of samples of the AZ61 alloy deformed in tension at 200 °C and  $10^{-3} \text{ s}^{-1}$ ; a) 0.2 true strain and b) 0.5 true strain.

Obviously, the recrystallisation process started before a true strain of 0.2. A bimodal microstructure was found, where grains resulting from the extrusion process were surrounded by new and fine recrystallised grains forming a “necklace” structure (Fig. 30a). As the deformation went on to 0.5 true strain, a fully recrystallised and homogeneous microstructure was observed (Fig. 30b). This effect was accentuated in the alloys with higher aluminum content such as AZ61 and AZ80 alloys.

It is known that most industrial alloys that contain more than one phase, the microstructure comprising a matrix phase and a dispersed second-phase particles. If these particles are present during deformation, they will affect the microstructure, and this in turn may or not affect the subsequent annealing behavior [69].

The presence of a high amount of particles of a secondary phase  $Mg_{17}Al_{12}$  in AZ61 and AZ80 alloys could increase the driving pressure for recrystallisation leading it to a new microstructure after deformation.

### **5.3 Yield asymmetry at intermediate temperatures**

In contrast with the observations at room temperature AZ31 tested at 175, 200 and 225 °C, the AZ31 alloy did not show asymmetry when the material was tested in tension. Surprisingly, at high strain rates there was not asymmetry of the yield strength, although the applied stress at high strain rate could promote the appearance of twins that could lead to different values of yield strength if tested in tension or compression [70]. However, when the strain rate decreases the asymmetry was observed, yet, it was not as high as room temperature. Again the inhomogeneous microstructure played an important role increasing the scatter of the results. In AZ61 alloy,

no asymmetry was found at 175 °C at all strain rates, but, increasing the temperature there was a shift in which the CYS had higher values compared with TYS. Still, the difference was not so pronounced as room temperature. Conversely in AZ80 a marked tendency is observed. When the strain rate is decreased, in all temperatures the difference of TYS and CYS increases monotonically. This can be related with the different rate in which dynamic recrystallisation took place. It is known by some authors [71], that dynamic recrystallisation occurs after a critical strain ( $\varepsilon_c$ ), which is dependent of the strain path, the initial grain size ( $D_o$ ), temperature (T) and strain rate ( $\dot{\varepsilon}$ ). The onset has been noticed by a stress peak on the true strain-stress curves. However, the corresponding strain peak ( $\varepsilon_p$ ) does not necessarily coincide with the microstructural critical strain ( $\varepsilon_c$ ). It is probable that the recrystallisation process in the case of AZ80 in compression tests started at lower strain compared with tension tests. In the sample tested in tension DRX is operative; however, the nucleation of new grains was mainly located on the grain boundaries of the grains from the as-extruded microstructure (see Fig. 31a). On the other hand, extensive shear banding and probably twins inside the grains were observed in samples tested in compression (see the arrows and the grain within the red circle in Fig. 31b). Within these regions, very fine grains develop and the old grains from the extrusion were consumed. Al-Samman et al. [59] noted that besides necklace formation as a DRX mechanism, dynamic recrystallisation also took place inside of twins formed during uniaxial compression tests performed on an extruded commercial magnesium alloy AZ31. The mechanism of DRX in twins was found to be of continuous nature, involving the formation of low angle boundaries and their conversion to high angle boundaries forming new fine grains.

Furthermore, it is worth to note that increasing the Al content a higher grain size in as-extruded condition was obtained. For the formation of shear bands, the grain size plays an important role in this regard. Several authors including Ridha and Hutchinson [72] and Korbel et al. [73] have shown that the tendency for shear banding is increased by increasing the grain size. Besides, the deformation temperature has a strong effect as well as the grain size. It has been demonstrated that shear banding becomes less common at high temperatures [74].

Nucleation of recrystallisation at shear bands has been in many metals and alloys including copper, aluminum among others [72, 75].

This mechanism of recrystallisation seems to be active in the compression tests. The average grain sizes of samples tested in tension and compression are plotted in Fig. 32. It can be seen clearly that recrystallisation was much more effective in compression tests resulting in finer grains compared to the grains from the tensile tests. Thus, nucleation of recrystallisation inside shear bands could increase the rate of the recrystallisation leading to a low yield strength compare with tension yield strength at the same temperature.

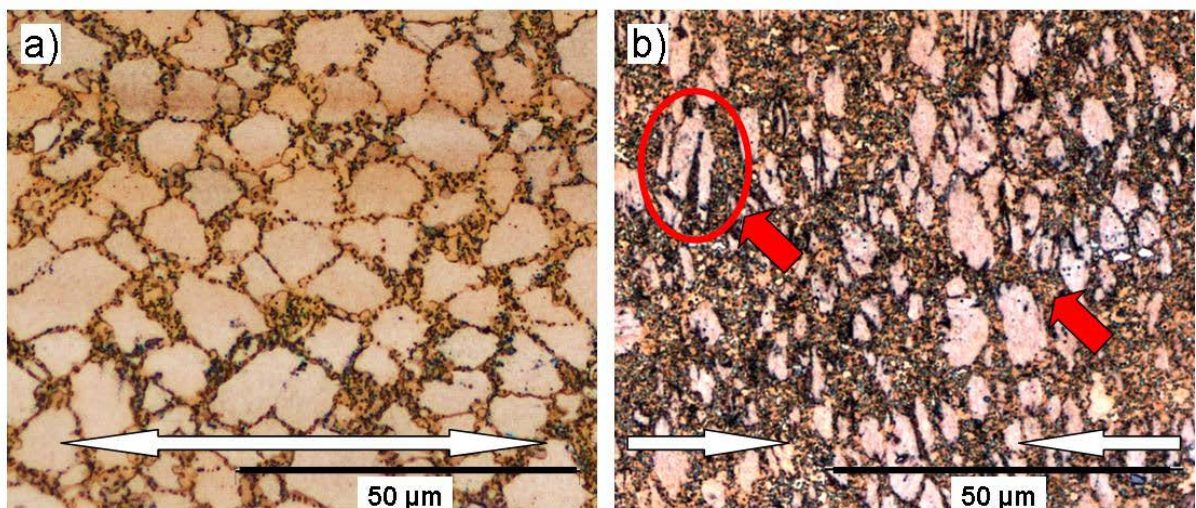


Fig. 31: Microstructure of deformed samples at 200 °C and  $10^{-3} \text{ s}^{-1}$ ; a) tension and b) compression tests (the double arrow indicates the load direction).

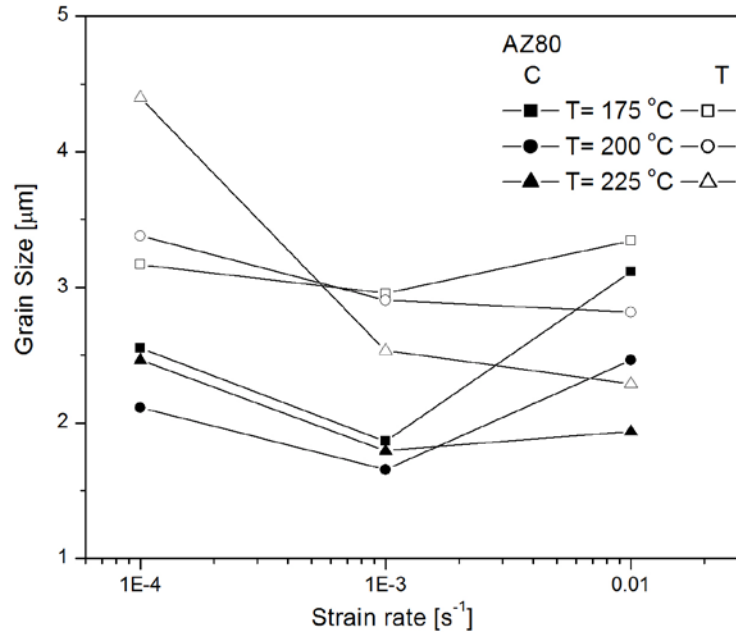


Fig. 32: Average grain sizes after deformation of the AZ80 alloy tested in tension and compression (Open symbols refer to tension whereas filled symbols refer to compression tests)

#### 5.4 Elongation to failure of tested samples

From Fig. 17a can be seen that the maximum elongation of 400% for AZ31 alloy was achieved at 225 °C and 10<sup>-4</sup> s<sup>-1</sup>. This behavior fits well with the behavior reported by Lee et al. [76] for extruded sheets of an AZ31 alloy tested in the low strain rates of 6x10<sup>-4</sup>s<sup>-1</sup> and temperatures around 225 °C. In that work the microstructure obtained by means of that method was homogeneous with an average grain size of 3 µm. Such grain size is quite comparable to the obtained by means of HE in this investigation of 5 µm. It is worth to mention, that the extrusion rate to get such fine and homogeneous microstructure was rather low of 0.001 ms<sup>-1</sup>, meanwhile, the AZ31 alloy processed by hydrostatic extrusion in this work allowed much

higher extrusion rates of  $0.130 \text{ ms}^{-1}$  and showed similar superplastic behavior.

AZ61 alloy showed a different behavior compared to AZ31 alloy. In this alloy very high elongations to failure were recorded at a high strain rate of  $10^{-2}\text{s}^{-1}$  when the material was tested at  $225 \text{ }^{\circ}\text{C}$ . Interestingly, the maximum elongation was observed at  $200 \text{ }^{\circ}\text{C}$  and  $10^{-3}\text{s}^{-1}$  instead of  $225 \text{ }^{\circ}\text{C}$  with the same strain rate. It would be expected that a higher temperature give better conditions for the superplastic phenomenon [33]. In order to determine the strain rate in which the maximum elongation was exhibited, two more strain rates,  $1.5 \times 10^{-3}$  and  $2 \times 10^{-3} \text{ s}^{-1}$ , were used at  $225 \text{ }^{\circ}\text{C}$ . It was found that the maximum elongation for AZ61 tested at  $225 \text{ }^{\circ}\text{C}$  was shifted to  $1.5 \times 10^{-3} \text{ s}^{-1}$  reaching an elongation to failure of  $540 \%$ . These results are plotted in Fig. 33 (see the dashed line).

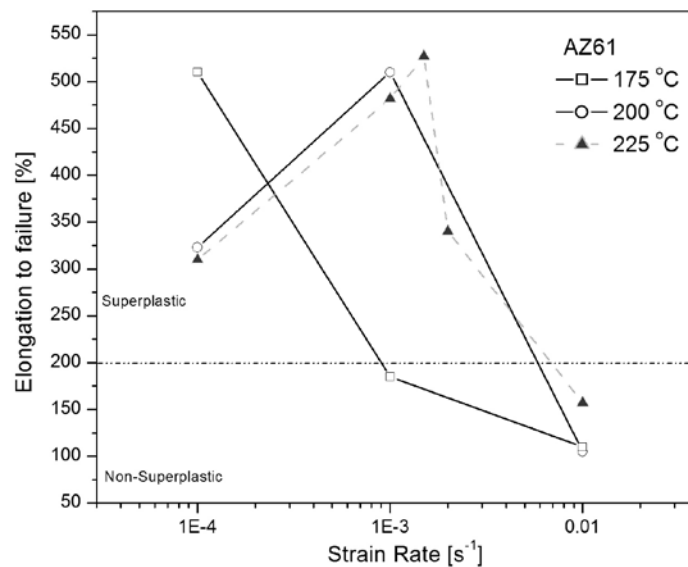


Fig. 33. Elongation to failure vs. strain rate for AZ61.

Kim et al.[77] worked with AZ61 sheets processed by hot rolling. In that work the results obtained are comparable with the elongations to failure recorded in this work. However, the thermomechanical treatment was

performed at substantially higher temperature of 375 °C. That temperature is more than twice the temperature used in HE. The resulting microstructure from that rolling was homogeneous with an average grain size of 8.7 μm. Nevertheless, the necessary temperature to achieve such elongations was considerable high. The tension tests were performed at 400 °C where the maximum elongations to failure of about 550 % laid in the range of  $10^{-4}$  to  $10^{-3}$  s<sup>-1</sup>. Conversely, an elongation to failure of 520% that is close to the maximum elongation achieved in this work was only at 175 °C in the low strain rate.

Interestingly at this low temperature the maximum elongation was almost reached. In order to understand what happened at higher temperatures than 175 °C an extra analysis in the microstructure was carried out. It is well known that for maintaining a fine grain size in the superplastic forming range, the presence of a second phase or particles at the grain boundaries are required [78]. An inspection of the distribution of precipitates in deformed samples from AZ61 in the low strain rate condition revealed that fine and well distributed precipitates were retained when tested at 175 °C (Fig 34a). However, as temperature increased to 225 °C, nucleation of coarse precipitates took place (Fig. 34b). The growth of particles in this condition corresponded to the appearance of cavities as seen in Fig. 34c for the sample tested at 175 °C and Fig. 34d for 225 °C. In sample tested at 175 °C can be seen that small cavities are distributed along the surface, meanwhile, in the sample deformed at 225 °C coarse cavities were found. Both effects can explain why the elongation to failure was reduced in this range.

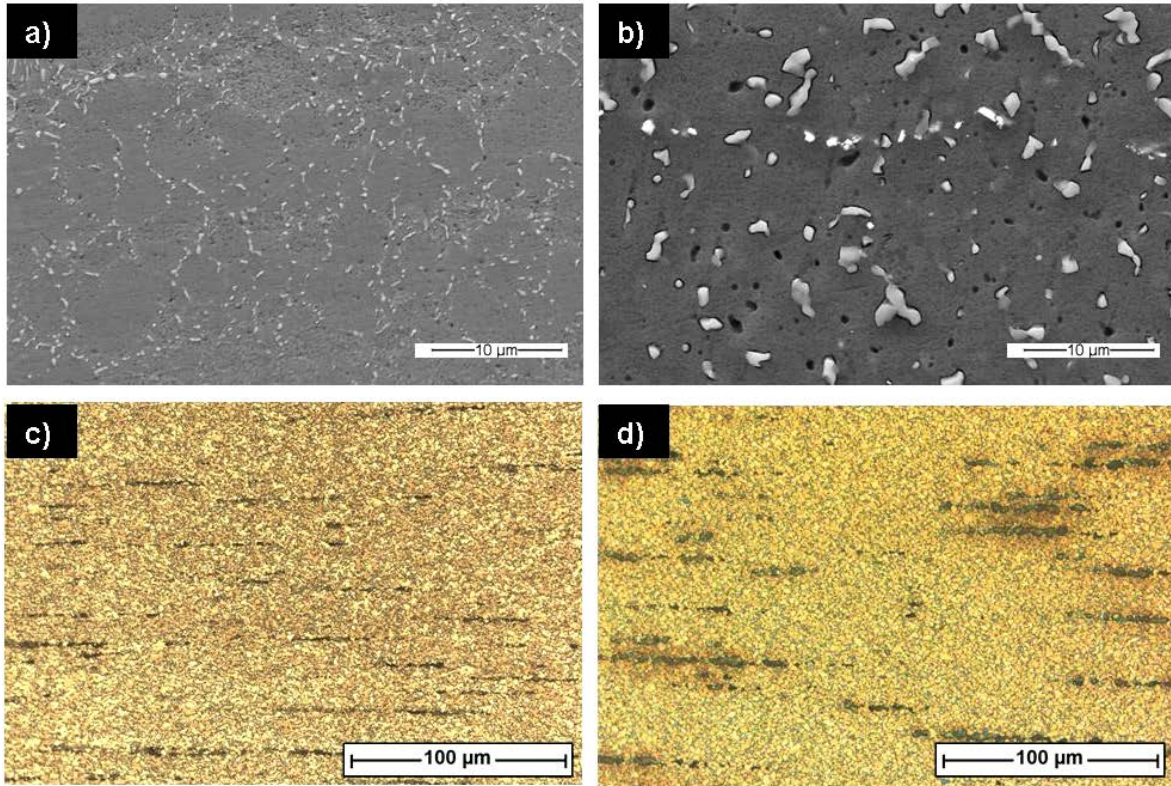


Fig. 34: SEM micrographs of precipitates distribution in AZ61 deformed superplastically at a) 175 °C and b) 225 °C and  $10^{-4} \text{ s}^{-1}$ ; optical micrographs of cavities taken near the fracture c) and d), respectively.

AZ80 alloy showed excellent plasticity at 225 °C in the moderate strain rate of  $10^{-3} \text{ s}^{-1}$ . In this alloy a similar behavior with AZ61 was observed. However, the different grain size measured in this alloy could be the reason that a higher temperature was necessary to achieve such elongation. The appearance of very coarse cavities in a sample deformed at 225 °C and  $10^{-4} \text{ s}^{-1}$  shown in Fig. 35 also confirms the observation made in AZ61, where cavitation was responsible of the reduction of the elongation to failure achieved by these two alloys. Also, the precipitates found in this alloy pointed by red arrows were coarser than the precipitates encountered in AZ61 alloy. These precipitates in contrast to the precipitates in as-extruded condition were only located on the grain boundaries.

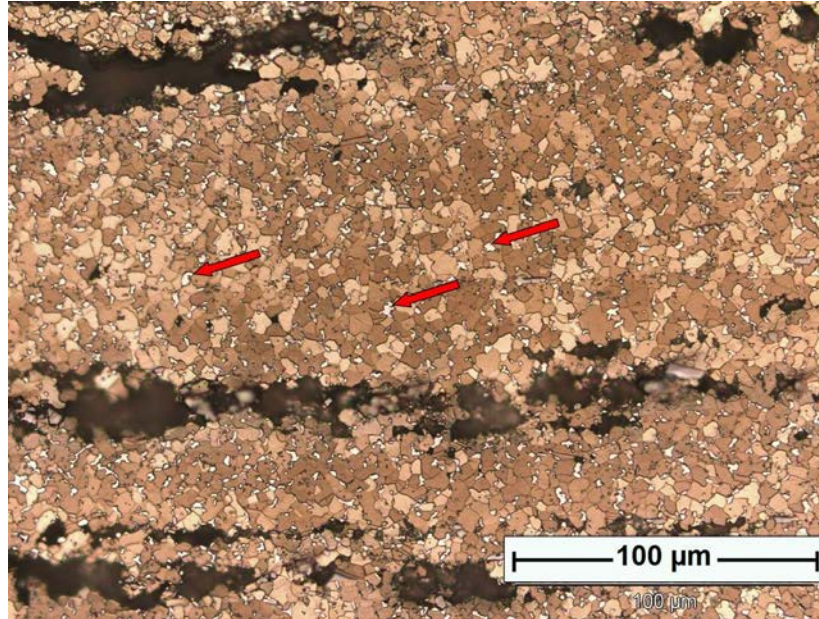


Fig. 35: Optical micrograph showing cavities near the broken tip on a sample made of AZ80 deformed at 225 °C and  $10^{-4} \text{ s}^{-1}$ .

#### 5.4.1 Strain rate sensitivity.

The strain rate sensitivity is intrinsically related with temperature and strain rate. It is agreed that to avoid neck formation, a strain induced hardening is required to offset the geometrical weakening caused by a reduction of the cross section of superplastically deformed samples [30].

From a very first preview, from the Fig. 18, the slopes of the curves  $\text{Log}(\text{strain rate})\text{-Log}(\text{Stress})$  for AZ61 alloy ( $m \sim 0.17$ ) did not correspond to the grain boundary sliding mechanism as explained in section 2.3. The low values of the apparent  $m$  correspond to the mechanisms of dislocation creep processes. This kind of deformation mechanism cannot be responsible for the high elongations achieved at least for the AZ61 alloy [32, 34].

Therefore, the strain rate sensitivity of AZ61 alloy was analyzed by the widely accepted strain-rate-changes tests, since this alloy reached the maximum elongations among the others.

Strain rate change tests were used to determine the strain rate sensitivity  $m$  of the alloy. The strain rates used were from  $5 \times 10^{-4}$  to  $5 \times 10^{-2} \text{ s}^{-1}$  at the three different temperatures. The initial strain rate used to stabilize the microstructure in the tests was  $10^{-3} \text{ s}^{-1}$ . A first strain rate jump down to  $5 \times 10^{-4} \text{ s}^{-1}$  was performed at a small strain of about 0.1 at all temperatures. Subsequently, the strain rate was increased in successive jumps until a high strain rate of  $10^{-1} \text{ s}^{-1}$ .

The results of the strain-rate-change tests are shown in Fig. 36a. Since in this investigation DRX occurred in all conditions tested the strain-rate changes tests were performed at intermediate and high strain rates in order to avoid important changes in the microstructure. The variation of the flow stress took from the peak stresses obtained from the strain-rate-change tests as a function of strain rate is presented in Fig. 36b. The flow stress increased with strain rate, and the relationship between the logarithmic flow stress and the logarithmic strain rate showed that the slope increased as the strain rate decreased. The slope around the intermediate strain rate  $10^{-3} \text{ s}^{-1}$  was 0.4. The summarized results of the tests are presented in Fig. 37. It is well accepted that the  $m$  values higher than 0.3 represent the deformation mechanism of GBS. Consequently, the material showed a typical superplastic behavior in which GBS is the main mechanism that controls the deformation [79]. This result is consistent with the high elongations to failure recorded at strain rates near  $10^{-3} \text{ s}^{-1}$  at 200 and 225 °C.

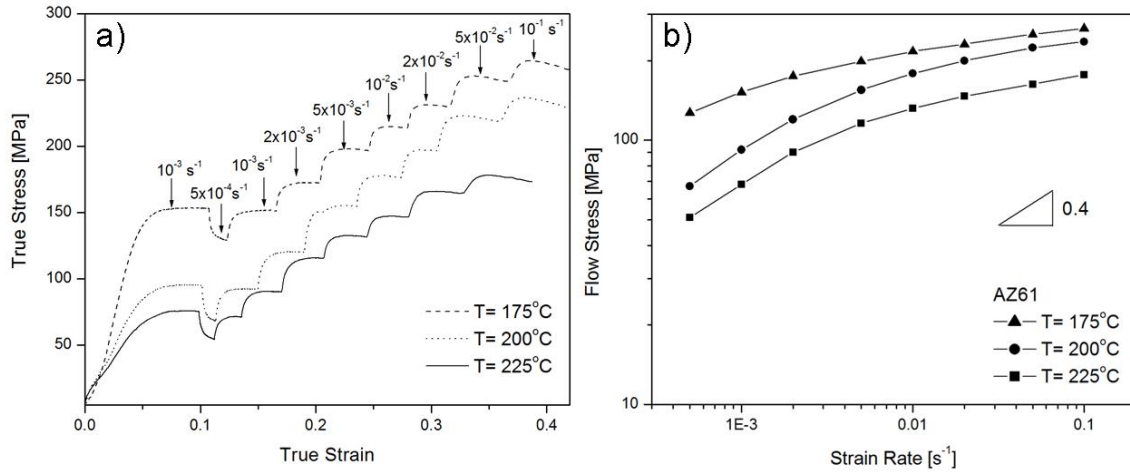


Fig. 36: (a) Strain-rate-change tests and (b) variation of flow stress as a function of strain rate at different temperatures.

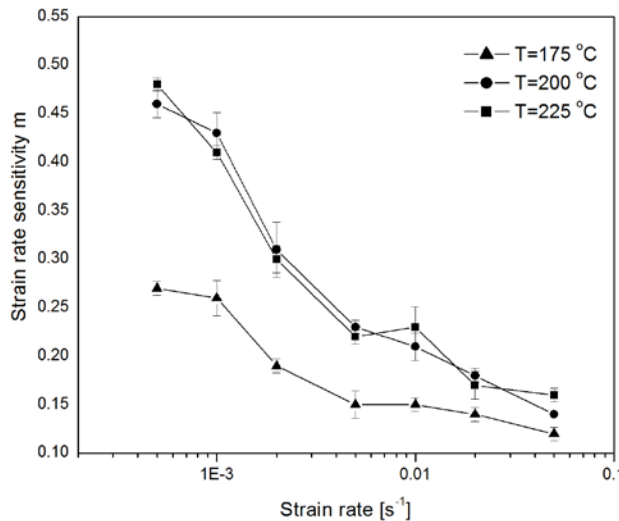


Fig. 37: Strain rate sensitivity ( $m$ ) as a function of strain rate at temperatures from 175 to 225 °C.

Fig. 38 depicts a microstructural observation of a sample tested at 200 °C and  $10^{-3} \text{ s}^{-1}$ , and deformed up to 0.5 true strain. The picture shows an observation of an offset in some marker lines at grain boundaries (see the arrows), indicating GBS as reported by Panicker et al. [32] and Tan et al. [68]. An interesting aspect to be considered is that equiaxed grains were

retained at fracture (as seen in Fig. 25). The retention of equiaxed grains even at very high tensile elongations is an important criterion for superplastic materials deforming by GBS [80].

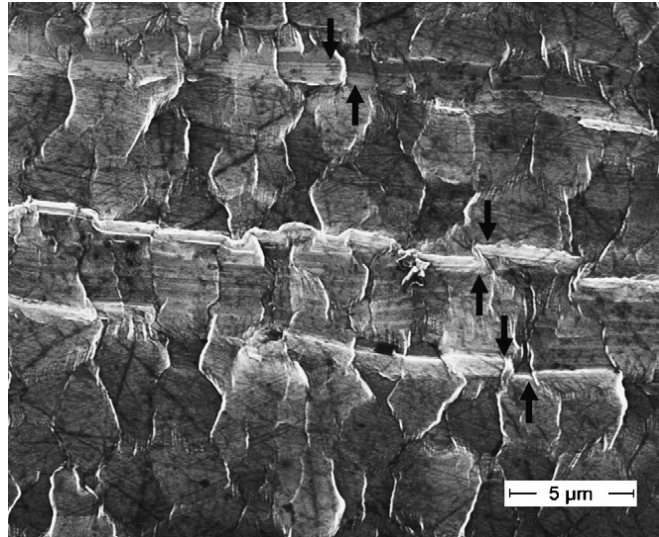


Fig. 38: SEM micrograph of a sample made of AZ61 alloy tested at 200 °C and  $10^{-3} \text{ s}^{-1}$  up to a true strain of 0.5 indicating GBS.

An inspection of the morphology characteristics on the gauge surface of the samples which showed the maximum elongation for AZ31 and AZ61 alloys is presented in Fig. 39. In both samples the grains seem to rotate during the deformation process. This morphology is often observed when grain boundary sliding is the rate-controlling mechanism [8, 34, 68]. Bieler et al. [81] demonstrated that this kind of morphology correspond to grain boundary sliding as the main mechanism during superplastic deformation of mechanically alloyed aluminum in which the strain rate sensitivity was 0.5.

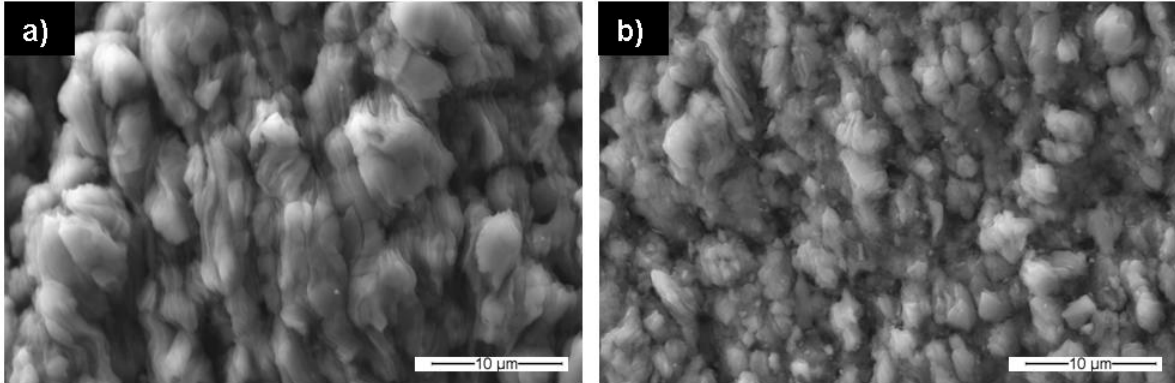


Fig. 39: Surface morphology of superplastically deformed samples. a) AZ31 at 225 °C and  $10^{-4} \text{ s}^{-1}$  and b) AZ61 at 225 °C and  $10^{-3} \text{ s}^{-1}$

#### 5.4.2 Samples morphology after deformation.

For AZ31 alloy, even though the samples reached elongations higher than 200%, localized necking can be observed in Fig. 20a. This effect provoked failure of the samples, although, the samples presented in such figure show the majority of the gauge length with uniform deformation.

In the case of the AZ61 alloy in most of the cases diffuse necking was present. Inspection shows that specimens tested at intermediate strain rates pull out uniformly to a point and there was no evidence for macroscopic necking within the gauge lengths. This was a sign that true superplastic condition was present [82].

The AZ80 alloy followed a similar behavior compared to AZ61 alloy. In the samples with elongations higher than 200 %, diffuse necking was present, and therefore, high elongations to failure were reached.

## 5.5 Microstructural and texture analysis after tensile deformation by means of EBSD.

As explained in section 4.8, due to the high Al content in the AZ80 alloy, the indexing of the Kikuchi patterns in the EBSD measurements was not good. Thus, the analysis in this section will only cover aspects from the AZ31 and AZ61 alloy. Just the activation energy will be calculated for the AZ80 alloy in order to have a reference of the effect of the Al content.

### 5.5.1 Zener-Hollomon parameter

In order to analyze the different microstructures and textures obtained from the tensile tests, the Zener-Hollomon parameter was calculated for the AZ31 and AZ61 alloy. The analysis of the results will be referred to this number to see a relation between applied parameters and deformation mechanisms observed. The following procedure was followed.

The samples tested up to fracture at different temperatures and strain rates were used for studying the microstructure development as a result of the applied testing parameters. It is recognized that the dependency of the flow stress on temperature  $T$  and strain rate  $\dot{\epsilon}$  can be reduced to one single factor, a temperature compensated strain rate  $Z$  which is a parameter named after Zener and Hollomon [83]

$$Z = \dot{\epsilon} \cdot \exp\left(\frac{Q}{RT}\right) \quad (4)$$

Where  $R$  is the gas constant and  $Q$  is the effective activation energy for deformation. The dependency of the flow stress of an experiment can then be reduced to this parameter. A general description which is commonly used [84] is a hyperbolic law

$$Z = \dot{\epsilon} \cdot \exp\left(\frac{Q}{RT}\right) = A \cdot (\sinh(\alpha\sigma))^n \quad (5)$$

where  $A$ ,  $\alpha$  and  $n$  are material constants that are considered to be independent of  $T$ , strain rate and stress. A number of works use procedures to derive the material constants, e.g. [66, 84, 85]. For this work the maximum stress was taken from the flow curves as the only significant parameter for evaluation. The resulting parameters according to Eq. 2 were collected in Table 1. The activation energy  $Q$  was higher for AZ80 than for AZ61 which was consistent with a higher amount of precipitates as well as higher solute content of aluminum in AZ80. In the case of the AZ61 compared to the AZ31 alloy, it was noted that the difference in activation energy affects the calculation of  $Z$ .

Table 6: Material constants of hydrostatically extruded AZ31 and AZ61 bars according to Equation 2.

Alloy	$Q$ [kJ/mol]	$\alpha$ [Mpa <sup>-1</sup> ]	$n$	$\ln(A)$
AZ31	119 (13)	0.013 (0.003)	3.3 (0.1)	22.44 (0.08)
AZ61	141 (3)	0.009 (0.002)	4.7 (0.1)	28.05 (0.06)
AZ80	148 (2)	0.003 (0.001)	6.5 (0.1)	31.03 (0.05)

### 5.5.2 Microstructural analysis.

An analysis of the microstructure after fracture was carried out using the EBSD orientation maps which also revealed grain size information. Typical examples of these series of measurements were shown in Figs. 24 and 25.

The microstructure which was generated during tensile testing was mainly a result of dynamic recrystallisation. Although it is hard to distinguish different fractions of the microstructure, i.e. deformed grains of the extrusion

microstructure and newly formed grains as a result of dynamic recrystallisation, the assumption of a low internal grain misorientation spread of recrystallised grains appeared appropriate; the results are presented in Fig. 40. From the graph the grain size reduction was consistent with a generally expected decrease of the recrystallised grain size with increasing Z. As far as it is seen in this figure no change in the development of the recrystallised grain size did reveal a change in the underlying recrystallisation mechanism, i.e. a change of the slope did not appear.

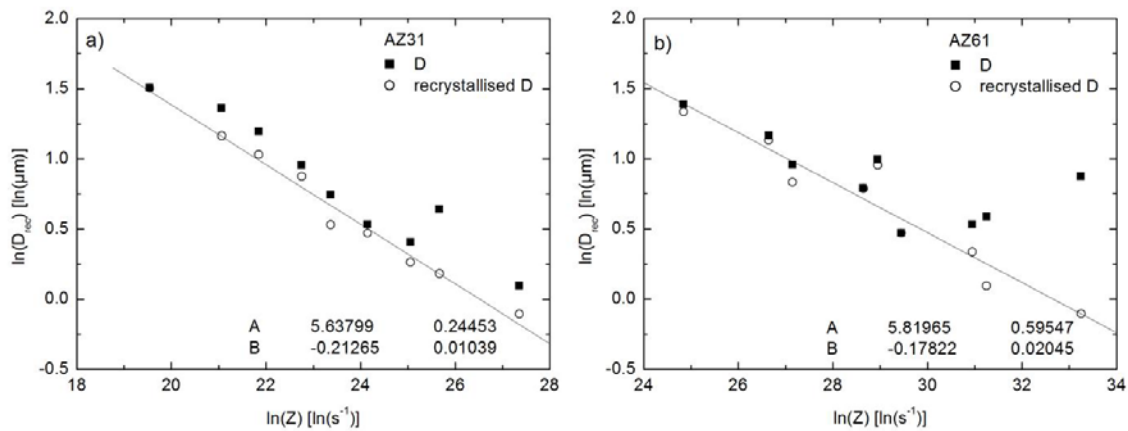


Fig. 40: Average grain size (filled symbols) and average recrystallised grain size (open symbols) as measured in quenched samples after tensile testing as a function of Z for a) AZ31 and b) AZ61 alloy.

Only at high Z (and therefore high strain rate, i.e.  $10^{-2} \text{ s}^{-1}$ ) some larger grains with higher misorientation spread were found which dominate the microstructure and led to an increase of the average grain size whereas the recrystallised grain size was still low (see Fig. 24a and 25a). It is worthwhile to repeat that the appearance of such unrecrystallised grains was limited to those samples with the lowest fracture strain and therefore a lower degree of dynamically recrystallised microstructure was expected. On the other hand, samples with high fracture strain had a large fraction of

grains with low misorientation spread and can therefore be considered as almost fully recrystallised. The lower Z the higher was the respective grain size.

### 5.5.3 Texture development

The EBSD measurements of samples after fracture were used to recalculate inverse pole figures in extrusion direction as shown in Fig. 41 for both alloys, AZ31 and AZ61. The pole figures were ordered according to a decreasing Z. Fig. 41a shows the results for AZ31. The maximum intensity of the pole figures first slightly decreased with decreasing Z but then increased again. This was understood as a result of changing significance of a number of texture components. At high Z the pole figures exhibited preferential orientations along the arc between the  $\langle 10.0 \rangle$  and  $\langle 11.0 \rangle$  poles with a higher intensity at the  $\langle 10.0 \rangle$  pole. With decreasing Z the  $\langle 11.0 \rangle$  pole component became more significant and results in the final increase of the maximum pole figure intensity. This is often experienced in magnesium extrusions if the material has the possibility to completely recrystallise [86]. Furthermore, after some tests, i.e. especially after testing at 200°C and  $10^{-2} \text{ s}^{-1}$  as well as 175 °C and  $10^{-4} \text{ s}^{-1}$  the  $\langle 11.0 \rangle$  component was not significant and a texture resulted which exhibits orientations around the  $\langle 11.1 \rangle$  pole. A texture component like this was hitherto found in very weak textures of magnesium extrusions that contain rare earth elements [19, 87]. Fig. 41b shows a very similar result for AZ61 which was even more distinct. With decreasing Z tendentially the  $\langle 10.0 \rangle$  pole intensity decreases. In some cases a more or less equal intensity distribution developed along the arc between the  $\langle 10.0 \rangle$  and the  $\langle 11.0 \rangle$  poles, especially at the lowest Z. In other cases the intensity distribution was generally low and only distinct along an arc between the  $\langle 10.0 \rangle$  and  $\langle 11.1 \rangle$  poles.

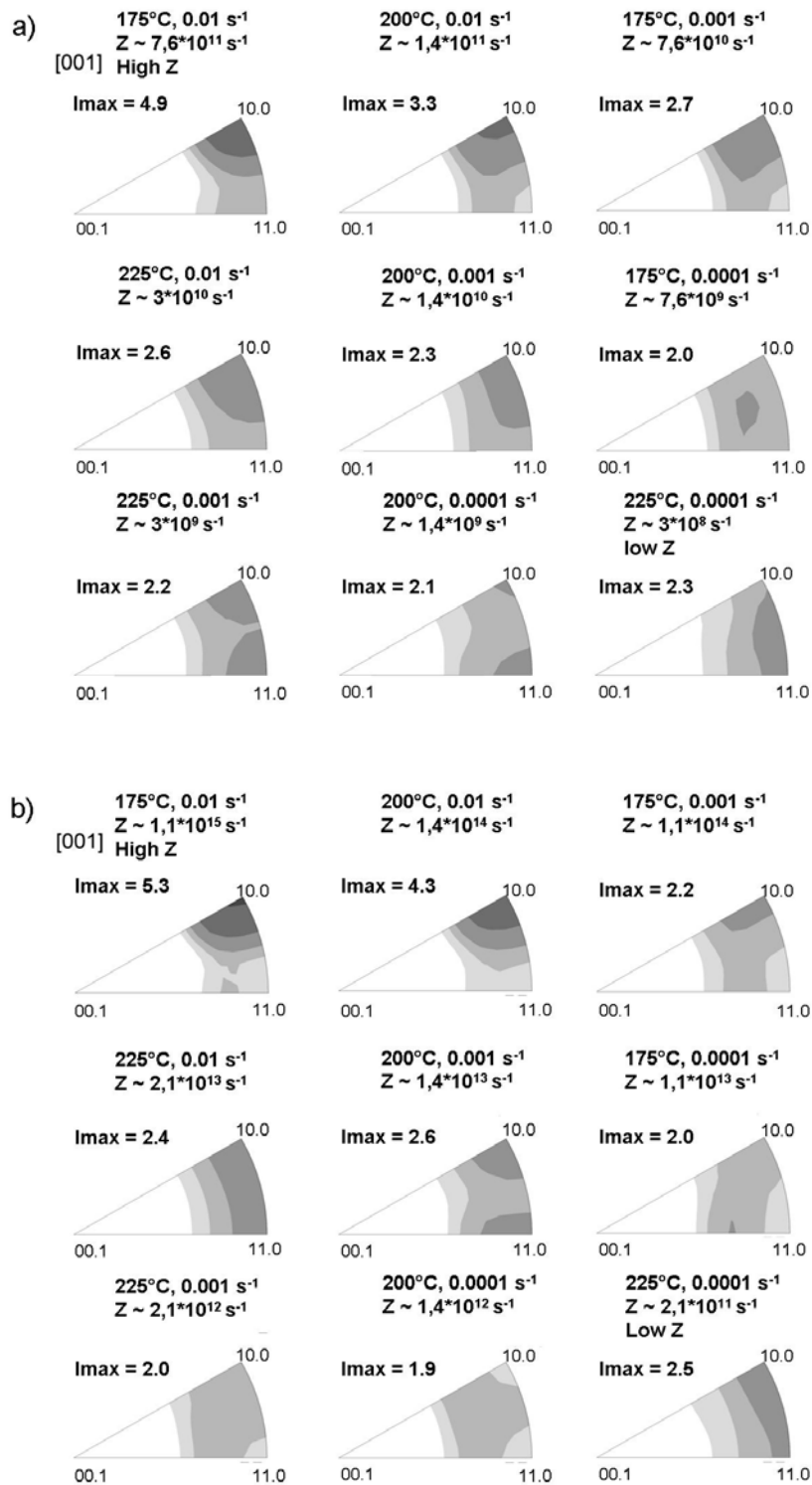


Fig. 41: Inverse pole figures of AZ31 and AZ61 alloy tested at temperatures from 175 to 225 °C and strain rates from 10<sup>-2</sup> to 10<sup>-4</sup> s<sup>-1</sup> as a function of Z (a and b, respectively).

It is seen in Figs. 41a and 41b that the intensities around the  $\langle 11.1 \rangle$  pole were not the result of a distinct texture component because intensities at this pole were quite comparable for all presented tests. It especially was visible due to the relatively lower number of grains with  $\langle 11.0 \rangle$  orientation. In order to reveal the significance of this and other texture components intensities of the inverse pole figures as measured at the  $\langle 10.0 \rangle$ ,  $\langle 11.0 \rangle$ , and  $\langle 11.1 \rangle$  poles as a function of  $Z$  were plotted in Fig. 42. A continuous decrease of the  $\langle 10.0 \rangle$  pole intensity with decreasing  $Z$  was observed for both alloys, AZ31 in Fig. 7a and AZ61 in Fig. 42b. Only in case of AZ61 at the lowest  $Z$  a relatively higher  $\langle 10.0 \rangle$  and  $\langle 11.0 \rangle$  pole intensity was found again.

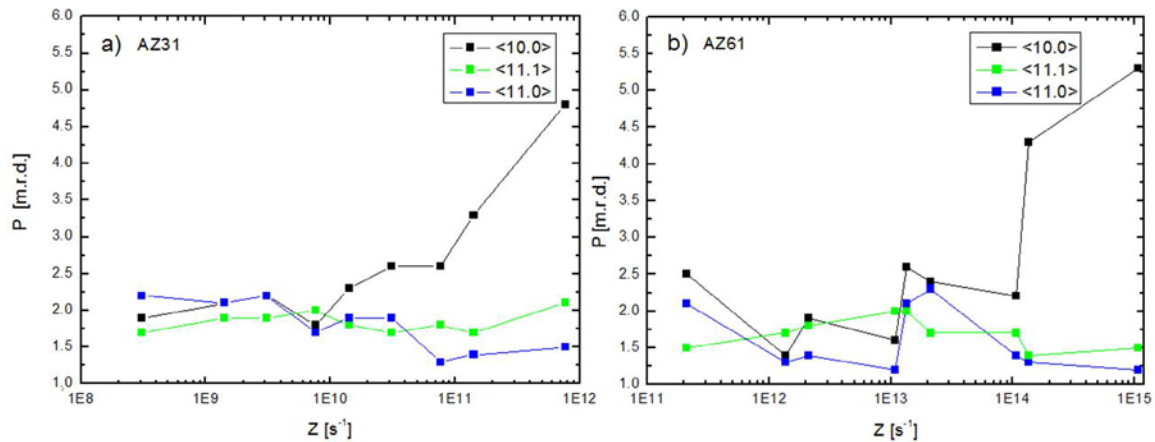


Fig. 42: Variation of the  $\langle 10.0 \rangle$ ,  $\langle 11.0 \rangle$ , and  $\langle 11.1 \rangle$  poles as a function of  $Z$  for a) AZ31 and b) AZ61 alloy.

Differences in the texture after testing were understood as a result of the degree of recrystallisation of the material. Samples with low fracture strain and therefore only partly recrystallised microstructures, i.e. the experiments at larger  $Z$ , also exhibited a strong  $\langle 10.0 \rangle$  fibre component which was related to the unrecrystallised remains of the initial extrusion microstructure. Such structures had also been observed as a result of extrusion itself [56]

and were therefore not likely changed during tensile testing or even strengthened again.

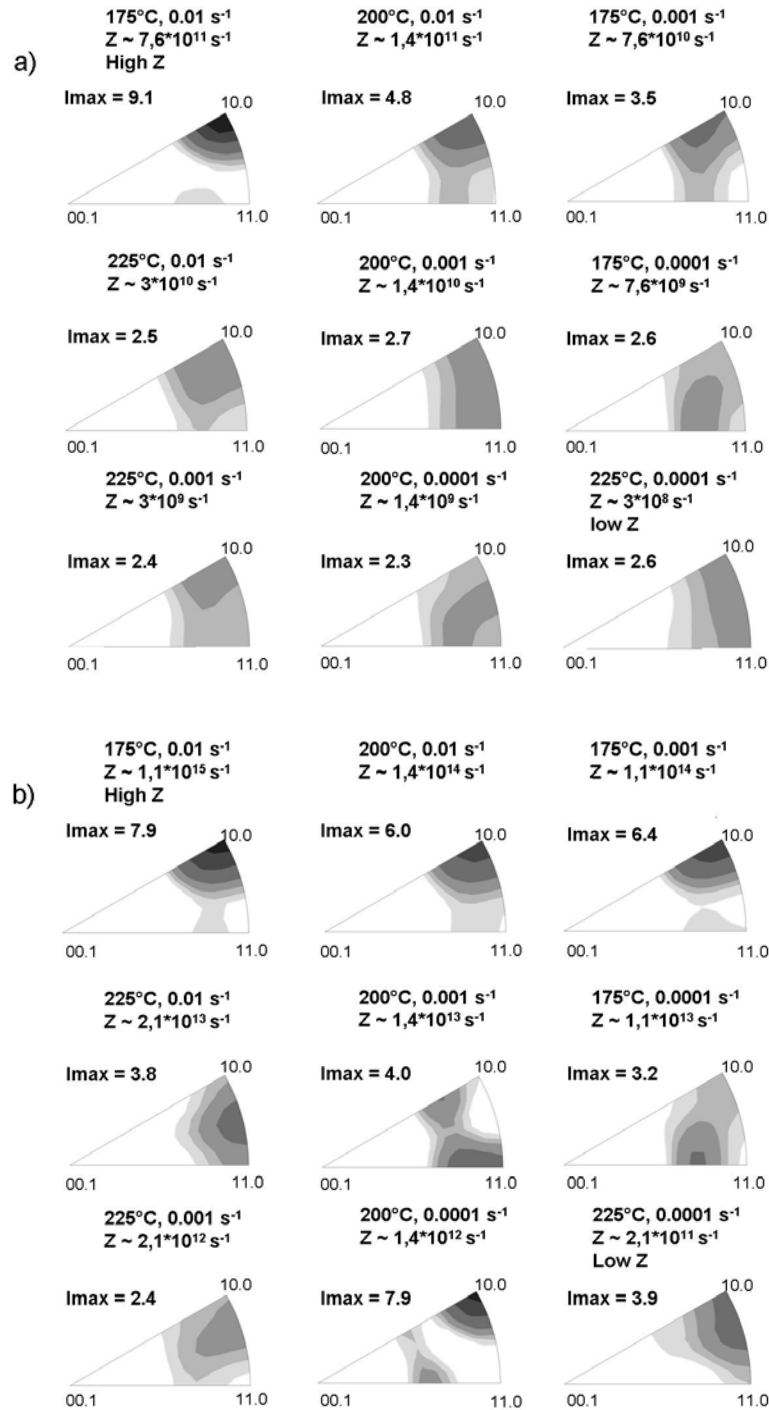


Fig. 43: Inverse pole figures of the fraction of the microstructure with a grain misorientation spread of more than 2° for a) AZ31 and b) AZ61 alloy.

Similar to the considerations about the recrystallised fraction of the microstructure, a larger grain misorientation spread can serve as a separating constraint for the unrecrystallised fraction of the microstructure. Fig. 43 summarised the resulting inverse pole figures of the fraction of the microstructure with a grain misorientation spread of more than  $2^\circ$ .

Two important aspects have to be considered in analysing this part of the microstructure. First, the given constraint of  $2^\circ$  again is mainly arbitrarily chosen. In the understanding that deformed grains will exhibit higher misorientations still this separation will significantly strengthen the fraction of unrecrystallised grains over any other fraction of the microstructure which encourages the following interpretations. Second, it has to be carefully noted that Fig. 43 displays the texture of that fraction of the microstructure which was an unrecrystallised remain of the original microstructure which underwent deformation. It therefore did not represent the overall deformation texture of the material because parts of the microstructure underwent recrystallisation during and after deformation. Still, the presentation allows important aspects of the deformation texture to be revealed.

Fig. 43a shows the results of AZ31 with decreasing  $Z$ . In case of one pole figure, i.e. the one after testing at  $175^\circ\text{C}$  and a strain rate of  $10^{-2}\text{ s}^{-1}$  a strong  $\langle 10.0 \rangle$  fibre was found which corresponded to the elongated grains also shown in Fig. 24a. Furthermore, a low intensity was also found around the  $\langle 11.1 \rangle$  pole in this condition. Although no distinct relation between the appearance of the texture components and the applied testing parameters, i.e. the variation of  $Z$ , was seen, a varying significance of  $\langle 10.0 \rangle$ ,  $\langle 11.0 \rangle$ ,  $\langle 20.1 \rangle$  and  $\langle 11.1 \rangle$  pole intensities was found. In summary, it can be considered that such texture components also appeared in the deformed state of grains despite the fact that the significance of the

components were a complex function of achieved strain and the underlying recrystallisation kinetics which determined the significance of this left fraction of the microstructure. The same was found for AZ61 in Fig. 43b where even more testing conditions led to strong  $\langle 10.0 \rangle$  components.

As shown in Fig. 17, very high tensile elongations were attained under certain testing conditions, in which some samples were able to reach elongations as high as 500 %. It was demonstrated that GBS was an operative mechanism responsible for the large tensile elongation reached [79]. However, this type of mechanism where grains slide past one another keeping their shape but changing their neighbors can not accommodate all the imposed strain and, in order to maintain material continuity, additional mechanisms (slip, creep or diffusion) have to be invoked. In fact, creep accompanied by DRX occurred during tensile testing changing the microstructure as discussed above.

When DRX takes place, non-basal slip systems should be activated during deformation, since the formation of high angle grain boundaries is promoted by non-basal slip rather than basal slip  $\langle a \rangle$ . This is because; basal slip  $\langle a \rangle$  causes a lattice distortion around the basal planes, which is not enough for the formation of new grain boundaries [65].

A correlation between the deformation mechanisms and DRX was made by Galiyev et al. [88]. They reported that during plastic deformation of a ZK60 Mg alloy at temperatures lower than 200 °C, twinning and basal slip are the dominant mechanisms that accommodate the plastic strain, however, it was pointed out that this combination of deformation mechanisms can only insufficiently comply with the compatibility constraints at grain boundaries. Due to large elastic distortion at grain boundaries, the

internal stresses could exceed the critical resolved shear stress (CRSS) for the activation of non-basal slip type  $\langle c+a \rangle$ , which is much larger than basal slip at low temperatures [89]. Therefore, increasing the zones required for the formation of recrystallisation nuclei. They also reported that at intermediate temperatures (200-250 °C) the controlling mechanism of plastic deformation was cross-slip of  $\langle a \rangle$  dislocations on non-basal planes. Such cross-slip was predominantly activated near original grain boundaries where the stresses were highly concentrated and continuous absorption of dislocations in the low-angle boundaries results in CDRX; i.e., in formation of new grains.

This could happen during the deformation of both AZ31 and AZ61 alloys in this work, however, some aspects have to be highlighted. On one hand, although the deformation was carried out at low temperatures around 200 °C, no evidence of twinning was found. This can be attributed to the very fine grain size of both alloys. It is known that twinning in magnesium alloys can be reduced or even suppress if the material has a very fine grain size [90]. On the other hand, the starting texture showed that the c-axis of the HCP structure lay perpendicular to the tensile axis used. Thus, this configuration does not promote the activation of tensile twinning of the type  $\{11\bar{2}1\}$ , that is the most common twinning mode [91].

Thus, the activation of non-basal slip  $\langle c+a \rangle$  and cross slip  $\langle a \rangle$  during tensile testing in this range of temperatures could influence the deformation texture and promote the formation of new recrystallised grains with a different orientation.

Al-Samman [92] shows in similar tests that a lower Z yields a thermal activation of non-basal slip such as  $\langle c+a \rangle$  pyramidal slip as well as enhanced DRX. During tensile testing in ED the distinct  $\langle 10.0 \rangle$  texture component persists which is understood as a favourable deformation by

prismatic  $\langle a \rangle$  slip. This texture component is accompanied by a second component,  $\langle 11.0 \rangle$  which is related to the  $\langle 10.0 \rangle$  pole by an angle of  $30^\circ$  and associated with the recrystallised fraction of the microstructure or the result of double prismatic slip. It is furthermore noted that work that multiple slip systems will prevent a distinct development of one single strong texture component and lead to the formation of a multi-component texture which can be very weak. It is especially discussed that the thermal activation of non-basal slip systems, e.g. prismatic  $\langle a \rangle$  slip leads to the formation of a texture component which is tilted away from the  $\langle 10.0 \rangle$  prismatic pole towards  $\langle 00.1 \rangle$ , i.e.  $\langle 10.1 \rangle$ . Although such components are not explicitly found in the experiments presented in the present work a broader intensity distribution along the arc between the  $\langle 10.0 \rangle$  and  $\langle 00.1 \rangle$  poles or a shift of the highest intensity along this arc away from the  $\langle 10.0 \rangle$  pole might hint to a similar activation of non-basal slip. Furthermore, the ongoing deformation of fractions of the microstructure which underwent recrystallisation might also be part of the pole figures presented in Fig. 43.

In order to separate details of the development of the recrystallised fraction of the microstructure Fig. 44 shows inverse pole figures of the fraction of the microstructure which had a grain misorientation spread of less than  $1^\circ$ . Two inverse pole figures separate this fraction of the microstructure into smaller and larger grains where the average recrystallised grain size was used as a constraint. A similar analysis was applied in [87] in order to separate effects of the growth kinetics of grains with different orientations in Mg-Mn alloys with added rare earth elements. For AZ31 in Fig. 44a at high  $Z$  the main texture component was the  $\langle 10.0 \rangle$  component which was distinct in both, the small and the large fraction of recrystallised grains. This component lost significance with decreasing  $Z$ . The same was found for AZ61 in Fig. 44b. At low  $Z$  a  $\langle 11.0 \rangle$  texture component was distinct for AZ31 which was tendentially more pronounced in large grains than in small grains. However,

this effect was not pronounced in case of AZ61. Instead of this, the textures were very weak and sometimes the highest intensities were not along the arc between the  $\langle 10.0 \rangle$  and  $\langle 11.0 \rangle$  poles any more. It is not possible to say if there is any preferential growth of grains with the resulting orientations along an arc between the  $\langle 20.1 \rangle$  and  $\langle 11.1 \rangle$  poles. It is again suggested that the significance of these intensities was due to lower intensities along the arc between the  $\langle 10.0 \rangle$  and  $\langle 11.0 \rangle$  poles rather than the development of a distinct texture component. In case of AZ31 there was also no significant growth effect of texture components other than the  $\langle 11.0 \rangle$  component at low Z. A preferential growth of a so-called "rare earth texture component" around the  $\langle 11.1 \rangle$  pole was found as a result of recrystallisation during an extrusion experiments, there was no preferential growth of such a component in the case of the AZ31 and AZ61 samples of this study.

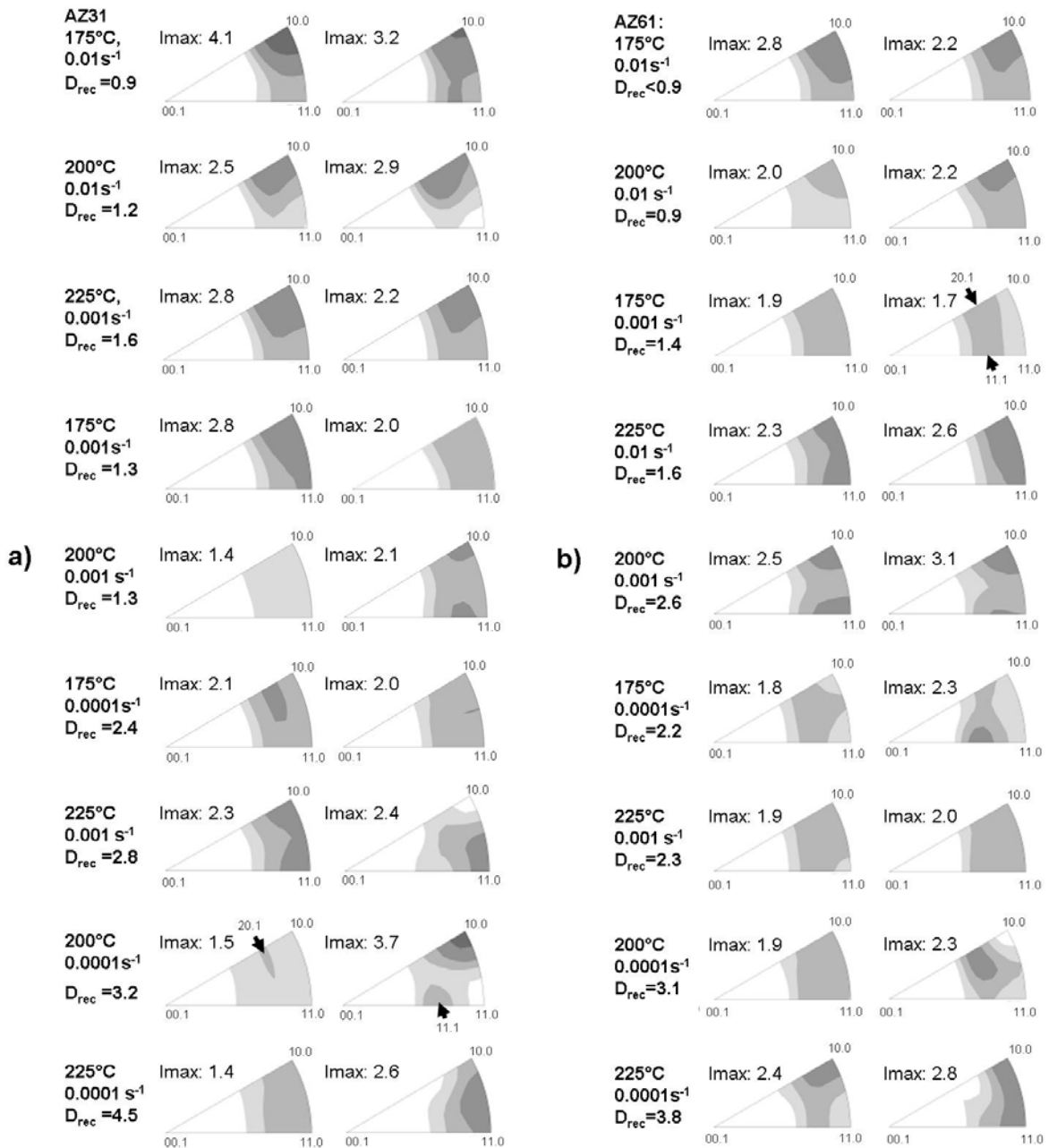


Fig. 44: Inverse pole figures of the fraction of the microstructure with a grain smaller (left) and coarser (right) grain sizes compared to the average recrystallised grain size for a) AZ31 and b) AZ61 alloy.

The development of a texture with a distinct <11.0> component has been observed by various authors as a result of the growth of recrystallised grains

in conventional Mg-Al-Zn alloys [61, 86] It can be a result of DRX if fully recrystallised microstructures are achieved [56] or the result of static recrystallisation (SRX) [86]. The latter one can be excluded as a possible mechanism in this study because samples were water-quenched immediately after testing. In case of DRX, discontinuous dynamic recrystallisation (DDRX) and rotational dynamic recrystallisation (RDRX) are reported to have a different impact on the texture development. Both mechanisms form a necklace type microstructure with fine recrystallised grains surrounding the unrecrystallised deformed grain. This mechanism of recrystallisation was present only during the first stages of deformation (0.2-0.5 true strain). For this reason it was also not possible to distinguish between different shapes of DRXed grains while there still can be a difference in the controlling mechanism for the texture development. DDRX is a mechanism based on conventional grain nucleation by grain boundary bulging based on high angle grain boundary migration. A mechanism like this will basically not change the underlying orientation which are present during grain nucleation and is therefore likely to not change the qualitative texture significantly. It was considered that boundary migration is favourable with a  $30^\circ$  misorientation to the deformed grain along the  $\langle c \rangle$ -axis which gives support to the assumption that  $\langle 11.0 \rangle$  orientations are a result of such a mechanism. DDRX is a mechanism that is reported to occur at higher temperature in several studies [88, 89].

RDRX is a continuous mechanism which is not based on boundary migration where subgrain boundaries form in the vicinity of grain boundaries which gradually transform into high angle grain boundaries. Such a mechanism will lead to an alternation of the texture based on grain rotation as e.g. described by Ion et al. [89].

It is hypothesised that as a function of Z the two different DRX mechanisms contribute differently to the texture development of the recrystallised

fraction of the microstructure. At low Z, where a <11.0> texture component was preferentially represented in larger grains with low misorientation spread, i.e. larger recrystallised grains, it was anticipated that DDRX determines the microstructure development whereas at higher Z this is not the determining recrystallisation mechanism. At high Z the microstructure development appeared to be limited with respect to recrystallisation, i.e. partly recrystallised microstructures result.

This randomisation of the texture at intermediate Z was also understood as a result of DRX. Furthermore, grain boundary sliding has to be considered as a texture contributing mechanism. It has been pointed out [39, 77] that textures can be strongly affected when GBS took place during deformation. It is hypothesised, that it is unlikely that DDRXed grains with fast migrating grain boundaries interact significantly with grain boundary sliding because this mechanism would restrict the ability to grain boundary sliding. Vice versa, such an interaction can be assumed at low Z where DDRX is an important mechanism but fracture strains were lower than at higher Z, especially in case of AZ61. Because of the resulting restrictions in texture strengthening it was possible to directly observe other texture components than those at the <10.0> or <11.0> poles.

Stress conditions which were applied during tensile testing as shown in this work were similar to those in round bar extrusions. This consideration is interesting because different texture components like those shown as a result of the tensile tests in this work are quite known as a result of extrusion of magnesium alloys. Although the differences in the original microstructure (cast microstructure of an extrusion billet versus an extraordinary fine-grained microstructure of the profile used for tensile tests) as well as the differences in the applied deformation parameters, temperature and strain

rate, are significant, it is noted that the change in such processing parameters can have the same impact on the texture development by extrusion.

It is known that alloying additions of rare earth (RE) elements result in significant texture weakening during extrusion which is reflected in an improved ductility at low temperatures [93, 94, 95]. In addition to this, similar textures are formed by adding these elements such as the development of a <11.1> texture component [19, 87, 96, 97]. Different hypothesis have been made in order to explain the origin of this characteristic texture distribution.

Stanford et al. [19] attributed the formation of the distinct texture component <11.1> to new recrystallised grains contained inside shear bands. It can be seen in that work, that the new component was only present at certain extrusion conditions, i.e. a low extrusion temperature. Binary magnesium alloy Mg-1.55 wt.% Gd exhibited the new texture component if extruded at 450 °C, however, when the extrusion temperature was raised to 510 °C it disappeared and the common <11.0> component was observed.

Thus, the recrystallisation kinetics itself can be considered as a reason for the development of this texture component. It was also shown that RE affect the recrystallisation by restricting grain growth [87]. As described in [87] the RE component is strongly influenced by different stages of recrystallisation depending on the RE used. In that work, the alloys which contained RE elements exhibited weak textures compared to alloys that did not contain RE elements. Besides, it was pointed out that the texture component depends on the size of recrystallised grains. Larger recrystallised grains exhibit a distinct <11.1> component whereas smaller recrystallised grains showed the original <10.0> component.

For common magnesium alloy AZ31 Yi et al. [86] demonstrated that recrystallised grains generated during extrusion were mainly produced by rDRX and that the high degree of internal misorientation of those grains was the driving force for the grains to grow during the annealing treatments. Furthermore, grain growth plays an important role in changing the texture of the respective profile. Such grain growth changed the texture distribution from the  $\langle 10.0 \rangle$  pole to the  $\langle 11.0 \rangle$  pole. It is noteworthy that the study of Yi et al. is also based on a hydrostatically extruded profile which was water-quenched after extrusion.

## 6. Conclusions

Hydrostatic extrusion carried out at 150 °C and high extrusion rate of 8 m/min was an effective thermomechanical treatment for refining the microstructure of the magnesium alloys AZ31, AZ61 and AZ80 all under 10 µm.

The average grain size measured for the AZ31 was approximately 5 µm, for the AZ61 was 5 µm, and for the AZ80 was 8 µm.

During extrusion, the effect of Al content is directly related to the recrystallisation process. The higher Al content the better recrystallisation. This can be seen for the well recrystallised microstructure with equiaxed grains in the case of the AZ80 alloy.

All alloys showed superplastic behavior at low temperature: 200 °C for AZ31, 175 °C for AZ61 and 225 °C for AZ80. Interestingly, the AZ61 alloy exhibited low temperature superplasticity at only 175 °C (0.33  $T_m$ ). At this temperature the elongation to failure recorded was about 520 % tested at a strain rate of  $10^{-4} \text{ s}^{-1}$ . The AZ61 alloy reached the maximum elongation of all alloys. This was 540% at 225 °C and a moderate strain rate of  $1.5 \times 10^{-3} \text{ s}^{-1}$ .

As a result of low temperature dynamic recrystallisation, significant work softening was observed during the tests. The microstructure produced by LTDRX was equiaxed and homogeneous that was retained up to the end of the tests. This could enhance GBS as the predominant mechanism to reach the high elongations recorded.

There is a processing window where complete recrystallisation took place and where the maximum elongations were reached:

For AZ31 alloy:  $T = 200 - 225 \text{ }^\circ\text{C}$ ,  $\dot{\epsilon} = 1 \times 10^{-4}$  to  $1 \times 10^{-3} \text{ s}^{-1}$ ,  $\epsilon \sim 1.1-1.6$

For the AZ61 alloy:  $T = 200 - 225 \text{ }^\circ\text{C}$ ,  $\dot{\epsilon} = 1 \times 10^{-4}$  to  $1 \times 10^{-3} \text{ s}^{-1}$ ,  $\epsilon \sim 1.4-1.8$

For the AZ80 alloy:  $T = 225 \text{ }^\circ\text{C}$ ,  $\dot{\epsilon} = 1 \times 10^{-4}$  to  $1 \times 10^{-3} \text{ s}^{-1}$ ,  $\epsilon \sim 1.2-1.6$

Extensive conglomeration of precipitates took place at  $225 \text{ }^\circ\text{C}$  and  $10^{-4} \text{ s}^{-1}$  in the AZ61 and AZ80 alloys during tensile testing. Since these coarse precipitates were not homogeneously dispersed on the grain boundaries, grain growth and the appearance of cavities were found. This fact reduced the fracture strain of both alloys at low strain rates.

Based on the results of the tension tests, the optimum Al content is the one of the AZ61 alloy. This produces the necessary quantity of secondary phase  $\text{Mg}_{17}\text{Al}_{12}$  which nucleates on grain boundaries keeping the equiaxed grain structure and limiting grain growth during tensile deformation at intermediate temperatures and strain rates where the maximum elongations were recorded.

In the compression tests, DRX played also an important role refining the microstructure during deformation. In this case all the alloys showed excellent plasticity and all of them were able to reach true strains as high as  $-1.3$  without fracture even when tested at the lowest temperature and the highest strain rate ( $175 \text{ }^\circ\text{C}$  and  $10^{-2} \text{ s}^{-1}$ ).

The higher grain size obtained for the AZ80 compared to the grain sizes of the AZ31 and AZ61 alloys promote the appearance of extensive shear banding during compression tests. The activation of this mechanism could

lead to the increase of the yield asymmetry in tension/compression at moderate and low strain rate ( $10^{-3} - 10^{-4} \text{ s}^{-1}$ ) at all temperatures. This could be attributed to the enhance recrystallisation process inside shear bands.

During tensile deformation, texture randomization was observed. This can be related to the high elongations to failure achieved in the AZ31 and AZ61 alloys. The underlying mechanisms that are active to reveal this condition include DRX and GBS. Furthermore, texture development includes the formation of grain orientations that so far have mainly been observed in rare earth containing magnesium alloys.

DRX and GBS were considered as the main mechanism to alter the texture during testing of AZ31 and AZ61 alloys. DDRX is connected with the formation of a typical  $\langle 11.0 \rangle$  texture component at low Z whereas with increasing Z this mechanism does not appear to be significant for the texture development. Thus, changes in the developing texture such as the appearance of new texture components are connected with the absence of this recrystallisation mechanism or at least with its non-significant contribution.

A comparison of the resulting textures of AZ31 and AZ61 samples after tensile testing reveals similarities to the texture development during conventional extrusion of rare earth containing magnesium alloys. It is suggested that in both cases a restriction of DDRX, i.e. a restriction of grain boundary migration, contributes to the texture development.

## References:

- [1] S.B. Yi, H.G. Brokmeier, R. E. Bolmaro, K.U. Kainer and T. Lippmann, *Scripta Mater.* 51 (2004) 455-460
- [2] K. Hantzsche, J. Bohlen, J. Wendt, K.U. Kainer, S.B. Yi and D. Letzig, *Scripta Mater.* (2010), doi:10.1016/j.scriptamat.2009.12.033
- [3] J. Bohlen, P. Dobron, E. Meza-Garcia, F. Chmelik, P. Lukac, D. Letzig and K.U. Kainer. *Adv. Eng. Mat.*, doi:10.1002/adem.200600023
- [4] W.J. Kim, M.J. Kim and J.Y. Wang, *Mater. Sci. Eng. A* 516 (2009) 17-22
- [5] H.J. Frost, M. F. Ashby, *Deformation Mechanism Maps*, Pergamon Press, Oxford, 1982
- [6] S. Spigarelli, *Mater. Sci. Eng. A* 492 (2008) 153-160
- [7] S. Q. Zhu, H.G. Yan, W. J. Xia, J.Z. Liu and J.F. Jiang, *J. Mater. Sci.* 44 (2009):3800-3806
- [8] S.W. Lee, Y.L. Chen, H.Y. Wang, C.F. Yang and J.W. Yeh, *Mater. Sci. Eng. A* 464 (2007) 76-84
- [9] H. Watanabe, M. Fukusumi, H. Somekawa and T. Mukai, *Mater. Sci. Eng. A*(2010), doi: 10.1016/j.msea.201006.053
- [10] J. Swiosteck, J. Goken, D. Letzig and K.U. Kainer, *Mater. Sci. Eng. A* 424 (2006) 223-229
- [11] J. Goken, J. Swiosteck, D. Letzig and K.U. Kainer, *Mater. Sci. Forum.* 482 (2005) 387-390
- [12] *Magnesium and Magnesium Alloys*, ASM International, 1999
- [13] E. Meza Garcia, *Extrusion of Magnesium-Zn based alloys*, Edit. Suedwestdeutscher Verlag fuer Hochschulschriften (2011).
- [14] K.U.Kainer, *Magnesium alloys and technology*, Wiley-VCH, 2003
- [15] K.U. Kainer, *6 Technology of Magnesium and Magnesium Alloys*, Wiley-VCH, 2003
- [16] Hanawit J.D, Nelson CE, Holdeman GE, US Patent 2,267,862,1940
- [17] P. Cao, M Qian, D. H. StJohn, *Scripta Mater.* 54 (2006) 1853-1858
- [18] L. Nascimento, S. Yi, J. Bohlen, L. Fuskova, D. Letzig, K.U. Kainer, *Procedia Engineering* 2 (2010) 743–750
- [19] N. Stanford, M.R. Barnett, Effect of microalloying with rare-earth elements on the texture of extruded magnesium-based alloys, *Mater. Sci. Eng. A* 496 (2008), pp. 399-408
- [20] Siebel G., *Technology of magnesium and its alloys* (Ed. Beck), Hughes, London, 1940

- [21] Roberts C.S., Magnesium and its alloys, Wiley, New York, 1960
- [22] Raynor G.V., The physical metallurgy of magnesium and its alloys, Pergamon Press, London, 1959
- [23] Chapman J.A., PhD thesis, University of Birminham, 1963
- [24] B.D. Cullity, S.R. Stock, Elements of X-Ray Diffraction, Third ed., Prentice Hall, 2001
- [25] G.E. Dieter, Mechanical Metallurgy, SI Metric ed., McGraw-Hill Co., London, UK, 1988
- [26] W.F. Hosford, The mechanics of crystals and textured polycrystals, Oxford University Press, 1993
- [27] B.C. Wonsiewicz, W.A. Backofen, Plasticity of magnesium crystals, Transactions of the metallurgical society of AIME 239 (1967) 1422-1431.
- [28] M. Yoo, Slip, twinning and fracture in hexagonal close-packet metals, Metallurgical Transactions A 12A (1981) 409-418.
- [29] R.C. Gifkins and T.G. Langdon, Comments on theories of structural superplasticity, Mater. Sci. Eng. 36 (1978) 27-33
- [30] W. A. Backofen, I.R. Turner and H. Avery, Superplasticity in Al-Zn alloy, Transactions of the ASM, Vol. 57, 1964
- [31] K. Sirinivasa Raghavan, Superplasticity, Bull. Mater. Sci. Vol. 6, No. 4, pp. 689-698, 1984
- [32] P. Panicker, A.H. Chokshi, R. K. Mishra, R. Verma and P.E. Krajewski, Acta Mater. 57(2009) 3683-3693
- [33] K.A. Padmannabhan, R.A. Vasin and F.U. Enikeev, Superplastic Flow Phenomenology and Mechanics, Springer-Verlag berlin Heidelberg 2001.
- [34] H. Watanabe, T. Mukai, K. Ishikawa, M. Mabuchi and K. Higashi, Mater. Sci. Eng. A 307(2001) 119-128
- [35] Ball A. and Hutchinson M.M., Met. Sci. Journal 3 I, 1968
- [36] M.F. Ashby and R.A. Verral, Acta Metal. 21, 149, 1973
- [37] R.C. Gifkins, Met. Trans. A7, 1225, 1976
- [38] W.J. Kim, J.D. Park, U.S. Yoon, J. Alloys and Compounds, 464 (2008) 197-204
- [39] H. Watanabe, M. Fukusumi, Mater. Sci. Eng. A 477 (2008) 153-161
- [40] W.J. Kim and S.W. Chung, Metals and Materials, Vol. 6, No. 3 (2000)
- [41] H. Watanabe, T. Mukai, M. Kohzu, S. Tanabe and K. Higashi, Acta Mater. 47, (1999) 3753-3758

- [42] Y. Miyahara, Z. Horita and T.G. Langdon, *Mater. Sci. Eng. A* 420 (2006) 240-244
- [43] M. Mabuchi, K. Ameyama, H. Iwasaky and K. Higashi, *Acta Mater.* 47 (1999) 2047-2057
- [44] W.J. Kim, M.J. Kim and J.Y. Wang, *Mater. Sci. Eng. A* 527 (2009) 322-327
- [45] A. Galiev, R. Kaibyshev, *Scripta Mater.* 51 (2004) 89-93
- [46] H.J. Bunge, *theoretical methods of texture analysis*, Edit. Informationsgesellschaft fur metallkunde, 1987
- [47] U.F. Kocks, C.N. Tomé, H.-R. Wenk, *Texture and Anisotropy: Preferred Orientations in Polycrystals and their Effect on Materials Properties*, Cambridge University Press, Cambridge, UK, 1998.
- [48] Wikipedia
- [49] Manual EDAX-TSL, 2010
- [50] A. W. Bowen, *theoretical methods of texture analysis*, Edit. Informationsgesellschaft fur metallkunde, 1987
- [51] J.A. del Valle, M.T. Pérez-Prado, and O.A. Ruano, *Metallurgical and Materials Transactions A*, Vol. 36a, June 2005—1427
- [52] Hiroyuki Watanabe, Akira Takara, Hidetoshi Somekawa, Toshiji Mukai, Kenji Higashi, *Scripta Mater.* 52 (2005) 449-454
- [53] S.B. Yi, S. Zaefferer, H.-G. Brokmeier, *Mater. Sci. Eng. A* 424 (2006) 275-281
- [54] R. Gehrman, M. M. Frommert, G. Gottstein, *Mater. Sci, Eng, A* 395 (2005) 338-349
- [55] J. Enss, T. Evertz, T. Reier, P. Juchmann, *Properties and Perspectives of Magnesium Rolled Products*, in: see [4] pp 590-595
- [56] J. Bohlen, S.B. Yi, J. Swiosteck, D. Letzig, H.G. Brokmeier and K.U. Kainer, *Scripta Mater.* 53 (2005) 259-264
- [57] J.J. Jonas, H.J. McQueen, *Recovery and Recrystallisation during High Temperature Deformation*, CNRS. "Mise en forme des metaux et alliages", Villars-sur-Ollon, (1975)
- [58] A.M. Wemba, H.J. McQueen, E. Herba, M. Sauerborn, *Hot Workability of Five Commercial Magnesium Alloys*, DGM, *Magnesium Alloys and their Applications*". Editors Morkdike BL, Kainer KU, Wolfsburg, pp 215-222, (1998)
- [59] T. Al-Samman, G. Gottstein, *Mater. Sci. Eng. A* 490 (2008) 411-420
- [60] V. Kree, J. Bohlen, D. Letzig and K.U. Kainer, *Pract. Metall.* 41 (2004) 233
- [61] L.W.F. V. Mackenzie, G.W. Lorimer, F.J. Humphreys, T. Wilks, *Mater. Sci. Forum* 477-82 (2004)

- [62] C.H.J. Davies, F. Xiong, M. Battaini, in: K.U. Kainer (Ed.), *Magnesium Alloys and Their Applications*, Wiley-VCH, Weinheim, Germany, 2003, pp. 433–438, P.G. Partridge, *Met. Mater.* 1 (1967) 169–194.
- [63] M.R. Barnett, Z. Keshavarz, A.G. Beer, D. Atwell, *Acta Mater.* 52 (2004) 5093–5103
- [64] C. Sanchez, G. Nussbaum, P. Azavant, H. Octor, *Mater. Sci. Eng. A* 221 (1996) 48–57
- [65] S.B. Yi, J. Bohlen, F. Heinemann, D. Letzig, *Acta Mater.* 58 (2) (2010) 592–605.
- [66] J. Liu, Z. Cui and C. Li, *Comput. Mater. Sci.* (2007), doi:10.1016/j.commatsci.2007.04.024
- [67] R. Cottam, J. Robson, G. Lorimer, B. Davis, *Mater. Sci. Eng. A* 485 (2008) 375–382
- [68] J.C. Tan, M.J. Tan, *Mater. Sci. Eng. A* 339 (2003) 81–89
- [69] F.J. Humphreys, M. Hatherly, *Recrystallization and related annealing phenomena*, second edition, Elsevier, 2004, pp. 48, 49
- [70] Christian JW, Mahajan S. *Prog Mater Sci* 1995;39:1
- [71] F. Montheillet, *Recrystallisation, Dynamic*, Encyclopedia of applied physics, vol. 16, VCH Publishers, Inc., 3-527-28138-x, (1996), pp. 205–225
- [72] A.A. Ridha, W.B. Hutchinson, *Acta Metall.* vol. 30, (1982), 1929
- [73] A. Korbel, J.D. Embury, M. Hatherly, P.L. Martin, H.W. Erbsloh, *Acta Metall.* vol. 34, (1986), 1999
- [74] A. Duckham, R.D. Knutsen, O. Engler, *Acta Mater.* 49 (2001) 2739
- [75] J. Hjelen, R. Orsund, E. Nes, *Acta Metall.* 39, (1991), 1377
- [76] C.J. Lee, J.C. Huang, *Acta Mater.* 52 (2004) 3111–3122
- [77] W. -J. Kim, S. W. Chung, C. S. Chung and D. Kum, *Acta Mater.* 49 (2001) 3337–3345
- [78] T.G. Nieh, J. Wadsworth and O.D. Sherby, *Superplasticity in metals and ceramics*, Cambridge University Press, 1997, p. 23
- [79] J. Victoria-Hernandez, D. Hernandez-Silva, S.B. Yi, D. Letzig and J. Bohlen, *Mater. Sci. Eng. A* 10.1016/j.msea.2011.09.104
- [80] T.G. Langdon, *Mater. Sci. Eng. A* 166 (1993) 67
- [81] T.R. Bieler, T.G. Nieh, J. Wadsworth and A.K. Mukherjee, *Scripta Metall.* 22 (1988) 851–8
- [82] T.G. Langdon, *Met. Sci.* 16 (1982) 175–183
- [83] C. Zener and J. H. Hollomon, *J. Appl. Phys.* 15 (1994) 22.

- [84] C. M. Sellars, *Mater. Sci. Tech.* 6 (1990) 1072-1081
- [85] H.J. McQueen, N.D. Ryan, *Mater. Sci. Eng. A* (2002) 43-63
- [86] S.Yi, H. G. Brokmeier, D. Letzig, *J. Alloys and Comp.* 506 (2010) 364–371
- [87] J. Bohlen, S. Yi, D. Letzig, K. U. Kainer, *Mater. Sci. Eng. A* 527 (2010) 7092-7098
- [88] A. Galiyev, R. Kaibyshev and G. Gottstein, *Acta mater.* 49 (2001) 1199–1207
- [89] Ion, S. E., Humphreys, F. J. and White, S. H., *Acta metall.*, 1982, 30, 1909.
- [90] P. Dobron, F. Chmelik, S.B. Yi, K. Parfenenko, D. Letzig and J. Bohlen, *Scripta Mater.* 65 (2011) 424-427
- [91] Z. Zhang, M. Wang, Z. Li, N. Jiang, S. Hao, J. Gong, H. Hu, *J. Alloys and Comp.* 509 (2011) 5571-5580
- [92] T. Al-Samman, X. Li, S. Ghosh Chowdhury, *Mater. Sci. and Eng. A* 527 (2010) 3450-3463
- [93] N. Stanford, D. Atwell, A. Beer, C. Davies, M.R. Barnett, *Scripta Mater.* 59 (2008) 772.
- [94] R.K. Mishra, A.K. Gupta, P.R. Rao, A.K. Sachdev, A.M. Kumar, A.A. Luo, *Scripta Mater.* 59 (2008) 562
- [95] J. Bohlen, M. R. Nürnberg, J. W. Senn, D. Letzig, S. R. Agnew, *Acta Mater.* 55 (2007) 2101-2112
- [96] N. Stanford, M. Barnett, *Scripta Mater.* 58 (2008) 179-182
- [97] N. Stanford D. Atwell, M. R. Barnett, *Acta Mater.* 58 (2010) 6773-6783